

MODEL, DESIGN & DEVELOPMENT OF
PIEZOELECTRIC ULTRASONIC MOTOR

DUAN WENHUI

NATIONAL UNIVERSITY OF SINGAPORE

2005

**MODEL, DESIGN & DEVELOPMENT OF
PIEZOELECTRIC ULTRASONIC MOTOR**

Duan WenHui

(B.Eng.,M.Eng.,TJU)

**A THESIS SUBMITTED
FOR THE DEGREE OF DOCTOR OF PHILOSOPHY
DEPARTMENT OF CIVIL ENGINEERING
NATIONAL UNIVERSITY OF SINGAPORE
2005**

Acknowledgements

I am lucky to study in two universities, both of which have more than 100 years history. I graduated from Tianjin University (China) founded at 1895 with a Bachelor degree in July 1997 and with an M.Eng. degree in July 2002. From July 2002, I began my PhD study at the National University of Singapore (NUS) founded in 1905. In 1995, I had seen the centennial celebration of Tianjin University as an undergraduate student. This year, NUS will celebrate her Centennial, while Tianjin University will celebrate her 110 years. Besides warmest congratulation to NUS and Tianjin University, I would like to give my deepest appreciation to the financial support for my Ph.D study from NUS.

I acknowledge my family for their unquestioning love and moral support that only one's family can provide. Thanks for everything that they have done to support me throughout my Ph.D time, my wife-Yali, my parents and other relatives.

I would like to thank a number of people who have been instrumental in guiding this research and providing useful advice throughout its course. Great thanks go to my supervisors, Prof. Quek Ser Tong and Prof. Wang Quan, for allowing me the freedom to pursue my own individual interests in this work; for teaching me how to find research problems, which is more crucial for a Ph.D student than just solving them; for their inspired ideas, which always make me go ahead on my way; for their patience and unfaltering commitment to their students - my first paper is revised up to eight times by them; for our discussion on life, society and philosophy, which may be more important than guidance on my research in some cases. Great thanks go to my thesis committee members, Prof. Wang Chien Ming of Department of Civil Engineering, Prof. Lim Leong Chew of Department of Mechanical Engineering, for reviewing my Ph.D proposal and

supervising my research progress. Great thanks go to Prof. Lim Siak Piang of the Department of Mechanical Engineering, for the discussion on my research topics. Great thanks go to English teachers, Madam Pang Hee Hung and Dr. Ng En Tzu for their help on my English study and thesis preparation.

Additional thanks go to my friends for their valuable help in both discussions of academic issues and in other issues everyday. I would especially like to thank Mr. An De Nian of Tianjin Municipal (Highway) Engineering Research Institute, China, for his exhaustive effort in providing detailed feedback on the design and fabrication of ultrasonic motor and drive circuit; Dr. Lu Feng, Dr. Jin Jing, Dr. Tua Puat Siong, Dr. Thamaraiikkannan Vinayagam, Dr. Chen Xi, Mr. Xu Qian Li, Mr. Zhou En Hua, Mr. Ma Yong Qian, Mr. Li Zhi Jun, and Mr. Wang Chang Long for their unbelievably helps over the years by offering their academic prowess, their time, their entertainment source, day or night, whenever a new hurdle was encountered.

I have many thanks to give to all the Laboratory Technologists, but I will specifically mention a few: Mr Sit Beng Chiat had an answer to every question and Mdm. Tan Annie had a solution for every problem. Mr Ang Beng Oon, Mr. Ow Weng Moon, Mr. Kamsan Bin Rasman, Mr. Wong Kah Wai and Mr. Yong Tat Fah were always around to help me keep going too. Special thanks go to Mr Ong Teng Chew and Mr Yip Kwok Keong for all of their helps in the laboratory and with computer issues.

I am also grateful to give to the Management Support Officers in the Department, namely, Ms Kathy Yeo, Mdm Tracey Yeoh Geok Kooi, Mdm R Kala Devi C Retnam and Ms Lim Sau Koon for all of their help in administrative issues.

War talk by men who have been in a war is always interesting; whereas moon talk by a poet who has not been in the moon is likely to be dull.

Mark Twain

Summary

The objectives of the present work are twofold: to develop advanced models for the accurate prediction of performance of piezoelectric traveling-wave ultrasonic motor (USM, a type of actuator that uses mechanical vibrations in the ultrasonic range), and to improve upon the typical piezoelectric traveling-wave motor configuration by investigating novel designs of the stator. The modeling objective addresses the need for an efficient design tool to complement or even overcome the costly process of prototype iteration. Similarly, to expand the viable commercial application of the traveling-wave motor as a direct-drive actuator, novel configurations of USM are suggested. The main scope of this study is: (a) modeling of piezoelectric coupled stator; (b) modeling of USM by finite element analysis; (c) design of annular stator with varying thickness; and (d) design of novel configuration of USM with multiple wave numbers.

Free vibration characteristics are a prelude to the dynamic analysis of piezoelectric coupled stator. As a basis for modeling of the piezoelectric coupled stator, analytical solutions of the free vibration of a three-layer piezoelectric laminated annular plate based on Kirchhoff and Mindlin plate theories are presented for the case where the electrodes on the piezoelectric layers are shortly connected. The electric potential distribution across the thickness of piezoelectric layer is modeled by a sinusoidal function and the Maxwell equation is enforced. The governing equations are solved using transformation of variables, by which, a sixth order PDE can be decoupled into three second order PDEs. To validate the proposed solutions, resonant frequencies and mode shapes of the piezoelectric coupled annular plates from the proposed solutions are compared with those obtained by FE analysis.

In addition to the development of an analytical model, methodologies for analyzing the overall behavior of USM are proposed and demonstrated by FE analysis due to its advantage of modeling complicated geometries and boundary conditions. The proposed model yields one of the more complete data sets on simulation of piezoelectric ultrasonic motors in the open literature. Numerical results, such as resonant frequencies and elliptic motion on the surface of stator, steady and transient relationship between axial force, rotor speed and torque, agree with published numerical and experimental results. The good correlation between FEM model and experiment verifies the proposed procedures for analyzing overall behavior of USM and also provided great potential for an accurate design tool.

Preliminary investigation of the concept of USM with varying thickness stator is performed. As a basis for the design of stator with varying thickness, free vibration analysis of thin annular plate with thickness varying monotonically in arbitrary power form are performed. Transformation of variable is introduced to translate the governing equation for the free vibration of thin annular plate into a fourth-order generalized hypergeometric equation. The closed form solutions are presented and verified by comparing with those from Kirchoff-based and 3D FEM for plates with linear increasing, non-linear increasing and non-linear decreasing thicknesses in the radial direction.

Another effort is the design and fabrication of the piezoelectric traveling-wave motor with multiple wave numbers. This multiple wave numbers operation is realized by a new electrode configuration of the piezoelectric element. Besides designing the configuration of the electrodes, drive electronics with four channels compatible with multiple wave numbers operation are also designed, tested and fabricated. The experimental results of the multiple wave numbers motor show that the multiple wave numbers motor significantly outperformed the single wave number motor with regard to the range of speed and torque output. This novel implementation of the traveling-wave motor also offers the extra control for stable operation of USM.

Contents

Acknowledgements	i
Summary	iv
Table of Contents	vi
List of Tables	x
List of Figures	xi
List of Symbols	xiii
1 Introduction	1
1.1 Historical background	2
1.2 Review on design effort of USM	4
1.2.1 Standing and traveling wave USM	4
1.2.2 Geometry of stator	10
1.2.3 Piezoelectric materials	11
1.2.4 Driving electronics	12
1.2.5 Summary of design considerations	13
1.3 Review on modeling effort of USM	13
1.3.1 Equivalent electric circuit method	14
1.3.2 Modeling based on Kirchhoff or Mindlin plate theory	15
1.3.3 Finite element analysis	16
1.4 Objective and scope of study	17
1.5 Outline	18

2	Exact Closed Form Solutions for Transverse Vibration of a Class of Non-Uniform Annular Plates	20
2.1	Vibration of circular plate with varying thickness	21
2.2	Transformation of governing equation	22
2.3	Closed form solutions	24
2.4	Some special cases	27
2.4.1	Solution for plates with uniform thickness	27
2.4.2	Solution for plates with linearly varying thickness	28
2.5	Numerical examples	29
2.5.1	Application of logarithmic solution	29
2.5.2	Effect of plate with varying thickness	31
2.6	Conclusions	35
3	Free Vibration Analysis of Piezoelectric Coupled Thin and Thick Annular Plate	36
3.1	Vibration of piezoelectric coupled plates	37
3.2	Strain and stress components in piezoelectric sandwich plate	38
3.3	Piezoelectric sandwich Kirchhoff plate	41
3.3.1	Basic equations	41
3.3.2	Solutions for w and ϕ	43
3.4	Piezoelectric sandwich Mindlin plate	45
3.4.1	Basic equations	45
3.4.2	Solutions for w , ψ_r , ψ_θ and ϕ	47
3.5	Numerical examples and discussion	50
3.5.1	Comparisons between proposed models and FEM	51
3.5.2	Effect of piezoelectric layer	55
3.6	Conclusions	58

4	Finite Element Solution for Intermittent-Contact Problem in Ring Type USM	59
4.1	Description of USM	60
4.2	Overall behavior analysis of USM by finite element method	61
4.2.1	Governing equations	61
4.2.2	Variational formulation	65
4.2.3	Spatial and temporal discretization for nonlinear dynamics	67
4.3	Proposed procedures for overall behavior analysis of USM	69
4.3.1	Equivalent piezoelectric force (EPF) routine	70
4.3.2	Steady-state contact (SC) procedure	71
4.4	Numerical demonstration and discussion	72
4.4.1	FEM models of Kagawa and Glenn USMs	72
4.4.2	Analysis of Kagawa motor	75
4.4.2.1	Free vibration of stator	75
4.4.2.2	Input parameters for SC and EPF procedures	75
4.4.2.3	Dynamic analysis of stator	76
4.4.2.4	Steady-state analysis by SC procedure	77
4.4.2.5	Transient analysis by EPF procedure	80
4.4.3	Analysis of Glenn motor	81
4.4.3.1	Free vibration of stator	81
4.4.3.2	Input parameters for SC and EPF procedures	82
4.4.3.3	Steady-state analysis by SC procedure	82
4.4.3.4	Dynamic analysis by EPF procedure	84
4.5	Conclusion	86

5	Design, Fabrication and Characterization of a Ring Type USM with Multiple Wave Numbers	87
5.1	Design of USM with multiple wave numbers	87
5.1.1	Piezoelectric configuration	89
5.1.1.1	Conditions for excitation of traveling waves in a ring . . .	89
5.1.1.2	Comparison of excitation conditions	90
5.1.1.3	Realization of multiple wave numbers operation	92
5.1.2	Driving electrical circuit	94
5.1.2.1	Waveform generator	94
5.1.2.2	Power amplifiers	97
5.1.2.3	Differential amplifiers	100
5.1.3	Mechanical parts	101
5.2	Fabrication of USM prototype	102
5.2.1	Piezoelectric ceramics preparation	102
5.2.2	Stator preparation	103
5.2.3	Rotor preparation	104
5.3	Preparation for characterization	105
5.3.1	Experimental instruments	106
5.3.1.1	Speed measurement	106
5.3.1.2	Torque and coefficient of friction measurement	107
5.3.1.3	Axial force measurement	108
5.3.1.4	Electrical variables measurement	108
5.3.1.5	Resonant frequencies and damping coefficients measurement	108
5.3.2	Controlling experimental conditions	109
5.4	Characterization of USM with multiple wave numbers	110
5.4.1	Modal parameters of stator	110
5.4.2	Overall behavior of USM with multiple wave numbers	111
5.4.2.1	Experimental results and numerical verification	112
5.4.2.2	Comparison of speed control variables	113
5.5	Conclusions	117

6	Conclusions and Recommendations	119
6.1	Conclusions	119
6.2	Recommendations for future work	122
	References	125
A	Description of USM	139
Appendix A	Description of USM	139
A.1	Kumada motor	139
A.2	Suzuki motor	139
A.3	Ohnishi motor	140
A.4	Dong motor	142
A.5	Flynn motor	143
A.6	Cagatay motor	143
B	Logarithmic Solutions of Generalized Hypergeometric Equation	145
Appendix B	Logarithmic Solutions of Generalized Hypergeometric Equation	145
B.1	$z_2(x)$	147
B.2	$z_3(x)$	149
B.3	$z_4(x)$	151
B.4	Convergence conditions	153
C	Electrical Drawing	155
Appendix C	Electrical Drawing	155
D	Mechanical Drawing	157
Appendix D	Mechanical Drawing	157
E	Vita	169
Appendix E	Vita	169

List of Tables

2.1	Material and geometrical properties of annular plate	30
2.2	Comparison of frequencies (Hz) of annular UHMWPE plate	31
2.3	Comparison of frequencies (Hz) of annular plate for $m = 1, 1/2, -1/2$. . .	32
3.1	Material properties	50
3.2	Comparison of frequencies (rad/s) of thin annular plate	52
3.3	Comparison of frequencies (rad/s) of moderately thick annular plate . . .	53
3.4	Comparison of first three displacement mode shapes for annular plate . .	54
3.5	Frequencies (rad/s) of annular plate with piezoelectric layers	56
4.1	Material properties	75
4.2	Comparison of frequencies (kHz) of Kagawa stator	76
4.3	Comparison of operational parameters of Kagawa motor	80
4.4	Comparison of frequencies (kHz) of Glenn stator	81
5.1	Material properties	110
5.2	Comparison of resonant frequencies (kHz) of stator	111
5.3	Experimental results of damping	111
5.4	Contact parameters of different cases	116

List of Figures

1.1	The Kumada motor (Kumada, 1985)	5
1.2	The Suzuki motor (Suzuki <i>et al.</i> , 2000)	5
1.3	The Ohnishi motor (Ohnishi <i>et al.</i> , 1993)	6
1.4	The Dong motor (Dong <i>et al.</i> , 2004)	7
1.5	Generic stator structure of traveling wave USM	7
1.6	The Flynn motor (Flynn <i>et al.</i> , 1992)	9
1.7	The Cagatay motor (Cagatay <i>et al.</i> , 2004)	10
2.1	Geometry of annular plate with varying thickness	23
2.2	Geometry of annular plate with $m = 1, 1/2, -1/2, 6/5$	30
2.3	Frequency ratio (varying thickness to uniform plate) for different m	33
2.4	Convergence conditions for different m and p	34
3.1	Annular plate surface-mounted with two piezoelectric layers	38
3.2	Frequency ratio based on FEM simulation under C-C conditions	57
4.1	Geometry of generic USM	61
4.2	FE discretization in SC and EPF routines and electrode arrangement	73
4.3	Displacements and velocity of Kagawa stator	77
4.4	Axial force and corresponding contact area in Kagawa motor	77
4.5	Overall behavior of Kagawa motor by SC routine	78
4.6	Transient response of intermittent-contact in Kagawa motor	81
4.7	Glenn motor overall behavior vs. frequency at 150 V _p by SC routine	82

4.8	Glenn motor overall behavior vs. voltage at 41.57 kHz by SC routine . . .	84
4.9	Transient responses of Glenn motor at 41.57 kHz and 150 V _p	85
4.10	Comparison of speed torque curve of Glenn motor	85
5.1	Excitation of a traveling wave by bonded piezoelectric ceramics	89
5.2	Comparison of electrode configurations with wave number 9	91
5.3	Electrode configurations of USM with wave number 4, 5, 10 and 20	92
5.4	Electrode configurations of USM with wave number 3, 6, 9 and 18	93
5.5	Integrated electronics used in the actuation and sensing	94
5.6	Waveform generator MAX038	95
5.7	TLC555 timer and SN74LS74A flip-flop	96
5.8	LF353 power amplifier	97
5.9	Composite amplifier by LF353 and PB58	98
5.10	Current monitor differential amplifier OPA27	100
5.11	Explode view of USM prototype	101
5.12	Power supply of USM	102
5.13	Fabricated piezoelectric ring in USM prototype	103
5.14	Fabricated stator in USM prototype	104
5.15	Fabricated rotor in USM prototype	105
5.16	Experimental setup for speed measurement	106
5.17	Experimental setup for torque measurement	107
5.18	Strain gage for axial force measurement	108
5.19	Resonant frequency behavior of stator for (a) fifth and (b) tenth modes .	112
5.20	Simulated vs. measured speed and torque	113
5.21	Simulated vs. measured output power	114
5.22	Measured input power	115
5.23	Measured efficiency	117

List of Symbols

A	Amplitude of vibration, real or complex	7
C	Capacitance of the circuit	14
C_d	Damping of mechanical system	14
C^E	Elastic compliance at constant electric field	40
d	Piezoelectric constant, strain/field at constant stress	70
D_r, D_θ, D_z	Electric displacements	40
e	Piezoelectric constant, stress/field at constant strain	40
E	Electrical field	14
E_z, E_r, E_θ	Electrical field in the radial, tangential and transverse direction	40
F	Applied force	14
I, K	Modified Bessel function of the first and second kind	28
J, Y	Bessel function of the first and second kind	28
k	Wave number	7
K	Stiffness of mechanical system	14
L	Inductance of the circuit	14
M	Mass of mechanical system	14
$M_{rr}, M_{\theta\theta}$	Bending moments in plate	38
$M_{r\theta}$	Twisting moment in plate	38
n	Number of nodal circles	31

p	Number of nodal diameters	8
q	Electrical charge	14
Q_r, Q_θ	Transverse shearing forces in plate	39
R	Resistance of the circuit	14
u	Displacement of mechanical system	14
$u_S(x, t)$	Standing wave displacement	7
$u_T(x, t)$	Traveling wave displacement	7
\mathbf{u}	Displacement of a material point on plate	8
u_r, u_θ, u_z	Displacement in radial, tangential and transverse direction of plate	9
\mathbf{v}	Velocity of a material point on plate	8
v_θ	Velocity in the tangential direction of a plate	9
w	Transverse displacement on the middle surface of a plate	8
Y	Youngs modules	23
α, β	Rayleigh damping factor	68
$\epsilon_{rr}, \epsilon_{\theta\theta}$	Normal strain components in plate	39
$\gamma_{r\theta}, \gamma_{rz}, \gamma_{\theta z}$	Shear strain components in plate	39
μ	Poisson ratio	23
ω	Circular frequency	8
ω_{rotor}	Rotary speed of rotor	9
Ω	Traveling wave veolcity	8
ψ_r, ψ_θ	Rotations of the normal to the mid-plane	45
ϕ	Electric potential	40
ρ	Density	30
$\sigma_{rr}, \sigma_{\theta\theta}$	Normal stress components in plate	39
$\tau_{r\theta}, \tau_{rz}, \tau_{\theta z}$	Shear stress components in plate	39

φ	Electric potential on the mid-surface of the piezoelectric layer	41
ε	Dielectric constant:the relative permittivity of a dielectric material	40

CHAPTER 1

Introduction

Electromagnetic motors were invented more than a hundred years ago and still dominated the industry. Industrial requirements have in the past focused mainly on improving the quality and quantity of electromagnetic motors. However, electromagnetic motors have several drawbacks. The foremost concern is the permanent magnet associated with most electromagnetic motors is heavy and takes up valuable space. Gear reduction is always required as well and this leads to a series of other problems like backlash, cogging, and added mass and volume of the actuator. Drastic improvement cannot be expected except through new discoveries in magnetic or superconducting materials. Recent advances in the field of smart materials and structures have led to the evolution of a new kind of motor, namely the piezoelectric ultrasonic motor (USM). Compared to conventional electromagnetic motors, USM has the advantages of high torque at low speed, quick response, quiet operation and simpler structure. The study of USM has received wide attention. Many different types of USM have been developed and gained numerous applications, such as in aerospace, vehicles, ships, cars and cameras. This research concerns the development of more accurate model and novel design of USMs.

1.1 Historical background

A piezoelectric USM is a type of actuator that uses mechanical vibrations in the ultrasonic range (i.e. inaudible to human) (Sashida and Kenjo, 1993). In general, a piezoelectric USM contains two basic components: the stator which generates vibratory motion and the rotor which transmits the motion onto a shaft. The stator comprises piezoelectric elements. Mechanical oscillations of high frequency and small amplitude are excited by piezoelectric elements in such a way that material points on the surface of the stator perform an elliptic motion. Usually the elliptic motion of the stator's surface is obtained by superposition of two orthogonal vibration modes of the stator having the same resonance frequency. The rotor is pressed against the stator and is driven by frictional forces.

Although the driving principle described above has been well known for at least 50 years (Williams and Brown, 1948), only few types of piezoelectric USMs have been developed prior to 1980. This is mainly due to the fact that piezoelectric materials with high conversion efficiency and fast electronic power control of mechanical oscillations were not available. The publication on the first USM (Barth, 1973), although a milestones in the history of piezoelectric USM, unfortunately did not have an immediate impact on the technology.

With increasing chip pattern density in the 1980s, the semiconductor industry began to request for more precise and sophisticated positioning systems which do not generate magnetic field noise. This accelerated the developments in ultrasonic motors (Sashida and Kenjo, 1993; Ueha and Tomikawa, 1993). Research interest in piezoelectric motors has been triggered by Sashida (1983) and many types of USM with size smaller than 100 mm have been machined during this decade. The designs of USM with different types of stator, such as rods, disk, cylinder, membranes and plates and their performance predicted using equivalent electric circuit models are the main research focus in this decade.

Market research conducted in the mid-1990s for 80 international electronic component companies indicated an intriguing demand for compact motors (that is, motors of size under 10 mm) over a 10-year period (Uchino, 1998; Wallaschek, 1995). Electromagnetic motors smaller than 10 mm and having sufficient energy efficiency and torque are difficult to produce. For example, a wrist watch motor with a rotor diameter less than 1 mm still requires a relatively large (10 mm) coil for its activation but with a low efficiency less than 1%. USMs whose efficiency is insensitive to size are considered superior in the field of compact motor. This led to a change in research focus in the development of compact USMs and Uchino *et al.* (2004) presented three key design concepts: (a) simplify the structure and reduce the number of component; (b) use simple (i.e. uniform) poling configuration; and (c) use standing-wave type to reduce the drive circuit components. For numerical simulations, Kirchhoff or Mindlin plate based models have been widely adopted.

Parallel to the development of compact USM, minimization of USM using silicon micro-processing technique have led to the fabrication of millimeter or sub-millimeter sized motors (Morita, 2003; Uchino *et al.*, 2004). Practical demands for miniature USM include those in microsurgery where insect scaled robots or micro positioning stages are employed, requiring actuators less than 1 mm³. For such size, using piezoelectric USM also poses problems. The challenge lies, for example, in the fragility of piezoelectric ceramics, the constraint of small amplitude of stator vibration and the bulkiness of the driving circuits. Special fabrication processes of piezoelectric materials, including a thin and thick film deposition process, various interesting stator structures and integrated driving circuits have been developed to overcome the above challenges. A useful tool to facilitate the design, development and performance evaluation of potential USMs is the finite element (FE) method where numerical simulation can be performed prior to prototype fabrication and testing.

1.2 Review on design effort of USM

There are two energy transfers in piezoelectric USM. First is the transfer from electric power to mechanical vibration power through piezoelectric materials as part of the stator (acting as a vibrator). Second is the transfer of the mechanical wave energy in the stator to the rotor (driven body) by means of frictional force at their point of contact. The efficient transfer of energy constitutes a main design effort.

To date, more than several hundred papers on the design of USM have been published. Excellent reviews can be found in various references (Morita, 2003; Sashida, 1983; Uchino, 1998; Uchino *et al.*, 2004; Ueha and Tomikawa, 1993; Wallaschek, 1995). It would be quite an endeavor to summarize them all; however, it may be meaningful to concisely present the major design efforts through a few characteristic examples, while detailed descriptions of these USM can be found in Appendix A. For the convenience of discussion, two widely adopted categories will be investigated for USMs from a vibration characteristic viewpoint of the stator: a standing wave type and a traveling wave type. Their working principles are presented. The other categories based on the generation of elliptical motion, stator geometry shape, piezoelectric materials, and driving electronics are also introduced.

1.2.1 Standing and traveling wave USM

For stator vibration, two types of waves can be generated to cause mechanical motion, namely, standing wave and traveling wave (Aoyagi *et al.*, 2004, 1996, 1997; Carotenuto *et al.*, 1998; Dong *et al.*, 2002, 2000, 2004; Dubois and Muralt, 1998; Fleischer *et al.*, 1989, 1990; Friend *et al.*, 2004; Iijima *et al.*, 1993; Juang and Hardtke, 2001; Kawai *et al.*, 1995; Koc *et al.*, 2002; Kumada, 1985; Lebrun *et al.*, 1996; Leinvuo *et al.*, 2004; Manceau *et al.*, 1998; Petit *et al.*, 1998; Rayner and Whatmore, 2001; Sato *et al.*, 1995; Satonobu *et al.*, 2003; Suetomo and Tomikawa, 2004; Suzuki *et al.*, 2004; Takano *et al.*, 1992, 1990;

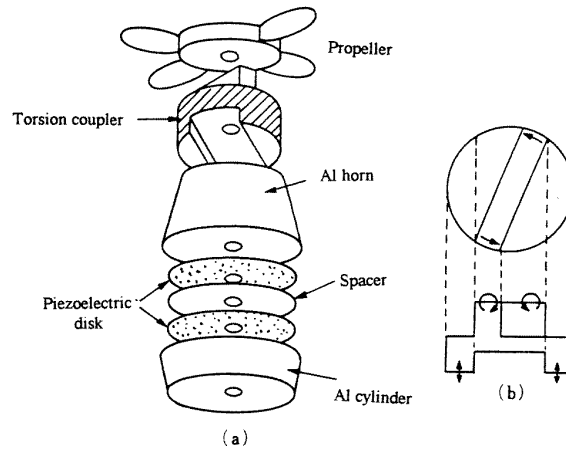
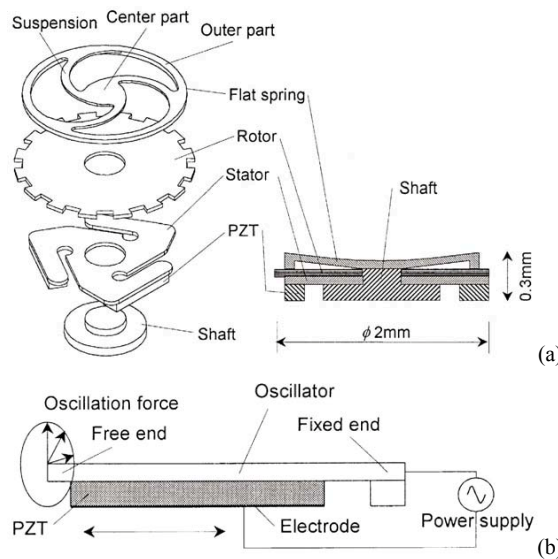


Figure 1.1: The Kumada motor (Kumada, 1985)

Tsujino, 1998; Uchiki *et al.*, 1991; Yao *et al.*, 2001; Yen *et al.*, 2003). To operate an

Figure 1.2: The Suzuki motor (Suzuki *et al.*, 2000)

ultrasonic motor, whether standing or traveling wave type, an elliptical motion at each contact point on the stator is required. Two orthogonal components of the elliptical motion will work in unison: the normal component controls the contact force between the stator and the rotor and the horizontal component drives the rotor. Thus, a large preload is required for the normal component to cause a large frictional force, and the driving component requires large vibration amplitude to achieve high speed in the rotor. In the standing-wave type USM, the elliptical motion is usually formed by mode conversion or superposition of multiple modes, for example, Kumada motor shown in Fig. 1.1. The

torsion coupler converts the longitudinal standing wave motion into an elliptical motion. This method of generating elliptical motion by mode conversion, where the torsion mode is converted from the bending mode. A similar mechanism is used in the composite stator of the Suzuki motor shown in Fig. 1.2.

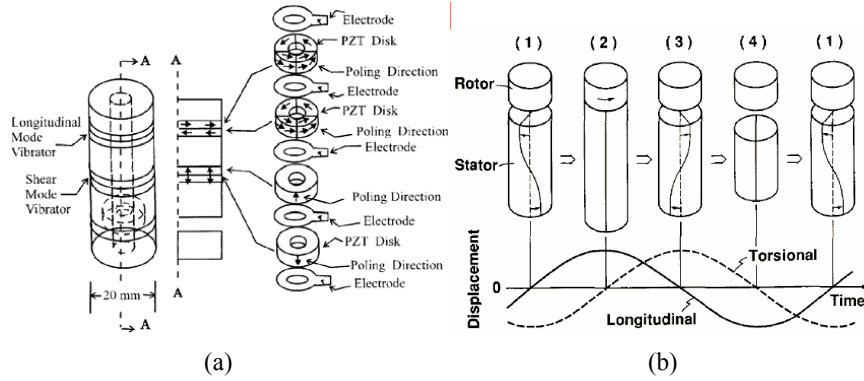


Figure 1.3: The Ohnishi motor (Ohnishi *et al.*, 1993)

Another example is the Ohnishi motor shown in Fig. 1.3. The longitudinal mode vibrator and shear mode vibrator generate longitudinal and torsional standing waves, and these two components are superposed to form an elliptical motion at the end of the rod type stator. The important thing to note is that the whole surface at the end of stator has the same normal vibration direction and amplitude. This method of generating elliptical motion is known as multiple modes superposition.

The Dong motor (Fig. 1.4) relies on the traveling wave, and its working principle is addressed as follows. The construction of Dong's motor can be simplified and plotted in Fig. 1.5. A piezoceramic ring is bonded to the bottom of an elastic ring (or plate) in the stator. On top of the ring near its circumference is a set of teeth separated radially. A layer of contact material is bonded to the bottom surface of rotor. In such traveling-wave type USM, the elliptical motion is also generated by the superposition of two standing wave components, but its mechanism is more complicated. Mathematically, a standing wave can be expressed by

$$u_S(x, t) = A \cos kx \cos \omega t \quad (1.1)$$

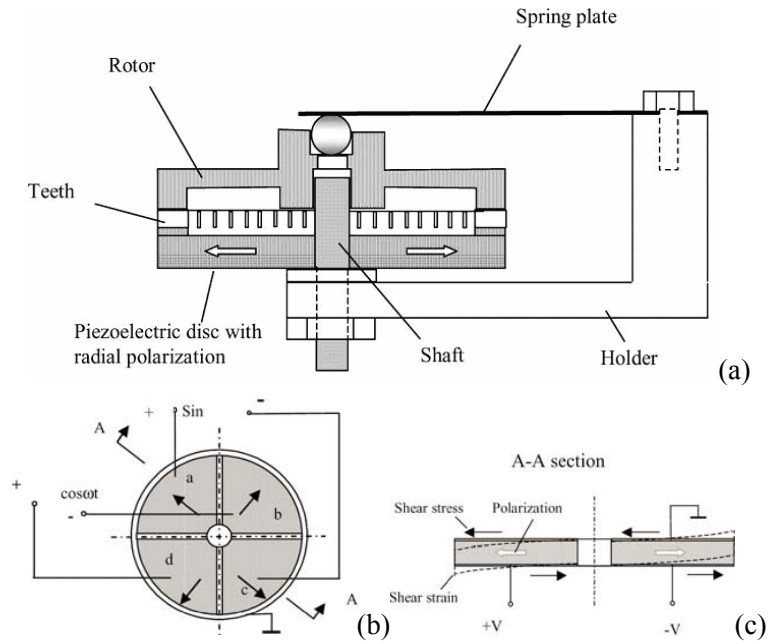


Figure 1.4: The Dong motor (Dong *et al.*, 2004)

where $u_S(x, t)$ is displacement of material point on the middle surface of the ring, A is amplitude of vibration, k is the wave number, and ω is circular frequency of vibration.

While a traveling wave can be represented by

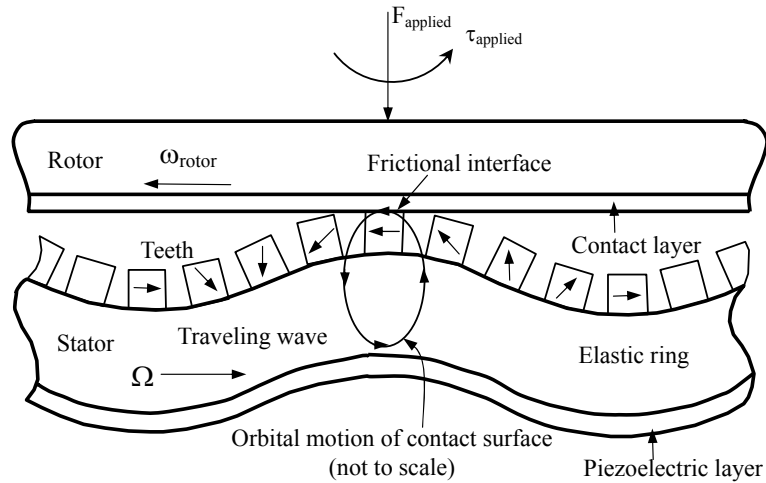


Figure 1.5: Generic stator structure of traveling wave USM

$$u_T(x, t) = A \cos(kx - \omega t) \tag{1.2}$$

where $u_T(x, t)$ is displacement of material point on the middle surface of the ring. Using

a trigonometric relation, Eq. (1.2) can be transformed as

$$u_T(x, t) = A \cos kx \cos \omega t + A \cos(kx - \pi/2) \cos(\omega t - \pi/2) \quad (1.3)$$

This leads to an important result; that is, a traveling wave can be generated by superimposing two standing waves whose phases differ by 90° from each other both in the spatial and temporal domain. Based on this concept, the piezoceramics are arranged into two groups such that they differ by 90° spatially from each other. These two groups are excited by two driving channels with varying voltages following a sine and a cosine wave. A traveling flexural wave will be generated within the stator. The traveling wave, not the stator, moves from left to right at a rotational speed denoted by Ω .

Next, it is shown that such a traveling wave cause an elliptical motion at the material points on the surface of the stator. If Kirchhoff's plate theory is adopted, a cylindrical traveling wave on the stator can be expressed in polar coordinates as

$$w(r, \theta, t) = AR(r) \cos(p\theta + \omega t) \quad (1.4)$$

with w the transverse displacement of the plate, p being the number of nodal diameters, $R(r)$ is a dimensionless function of the stator's deflection in the r -direction, which is usually normalized so that A can be interpreted as the modal amplitude for a particular radius of interest. The displacement of a material point on the stator is given by

$$\mathbf{u}(r, \theta, z, t) = -z \frac{\partial w(r, \theta, t)}{\partial r} \mathbf{e}_r - z \frac{\partial w(r, \theta, t)}{r \partial \theta} \mathbf{e}_\theta + w(r, \theta, t) \mathbf{e}_z \quad (1.5)$$

and its velocity is written as

$$\mathbf{v}(r, \theta, z, t) = \frac{d}{dt} \mathbf{u}(r, \theta, z, t) \quad (1.6)$$

It is well-known that for a traveling wave, all material points perform an elliptical motion whose projection on the e_r, e_θ plane is given by

$$u_\theta(r, \theta, z, t) = \frac{z}{r} p AR(r) \sin(p\theta + \omega t) \quad (1.7)$$

$$u_z(r, \theta, z, t) = AR(r) \cos(p\theta + \omega t) \quad (1.8)$$

Thus

$$v_{\theta}(r, \theta, z, t) = \frac{z}{r} \omega p A R(r) \cos(p\theta + \omega t) \quad (1.9)$$

$$[u_z(r, \theta, z, t)]^2 + \left[\frac{r}{zn} u_{\theta}(r, \theta, z, t)\right]^2 = A^2 R^2(r) \quad (1.10)$$

where $u_{\theta}(r, \theta, z, t)$ and $u_z(r, \theta, z, t)$ are the displacement of a material point on the stator in θ and z direction, $v_{\theta}(r, \theta, z, t)$ is the velocity of a material point on the stator in θ direction. At a given time the material points lying on the wave crest have a circumferential velocity of

$$v_{\theta}^* = \frac{z^*}{r^*} \omega n A R(r) \quad (1.11)$$

where z^* and r^* are the polar coordinates of the material point under consideration.

In generating the elliptic motion, the elastic wave is traveling in an annular plate, so it is also called a mode rotation method. Once the elliptical motion is realized, the rotor and the stator will be in contact at various points resulting in having the effect of an external compressive force and torque applied on the rotor as shown in Fig. 1.5. Specifically, the normal component u_z of the elliptical motion provided the normal force by contacting with rotor; and the horizontal component u_{θ} causes the rotor to spin by frictional force. At this point, it is important to realize that the rotational speed of the rotor is not equal to the frequency of the traveling wave. There is a virtual gear reduction inherent in these motors; Ω is usually of the order of tens of kilohertz whereas ω_{rotor} can be as low as or even lower than one hertz.

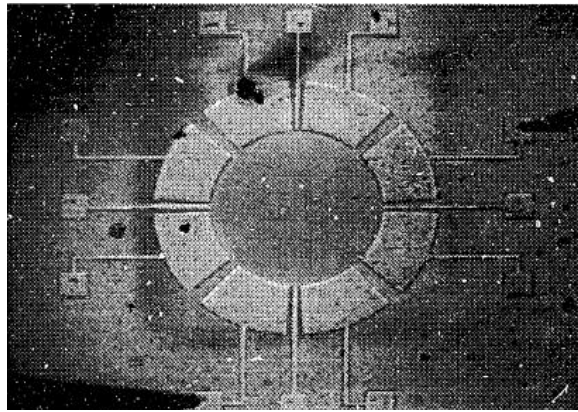


Figure 1.6: The Flynn motor (Flynn *et al.*, 1992)

The traveling wave type motor makes use of the elliptic motion of the vibrator surface caused by wave propagation. The rotor has only mechanical contact with the stator at specific surface points (wave crest). Compared with standing wave type USM shown in Fig. 1.3, the areas of these contact points are small relative to the total surface area of the stator. Hence, for small diameter stator, the standing wave type motor produces larger torque than that of the traveling wave type. Two other similar traveling wave USMs are given in Fig. 1.6(Flynn motor) and Fig. 1.7(Cagatay motor).

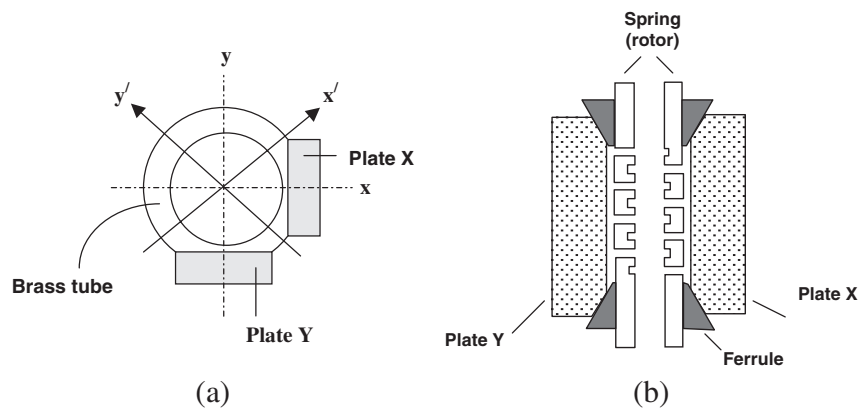


Figure 1.7: The Cagatay motor (Cagatay *et al.*, 2004)

1.2.2 Geometry of stator

Many different shapes for stator, including rods, rings, disks, and cylinders were adopted in the design of stator (Aoyagi and Tomikawa, 1993; Aoyagi *et al.*, 1992; Bexell and Johansson, 1999; Carotenuto *et al.*, 2004; Dong *et al.*, 2003; Koc *et al.*, 2000, 1998; Kurosawa *et al.*, 1996, 1989; Lamberti *et al.*, 1998; Ohnishi *et al.*, 1993; Suzuki *et al.*, 2000; Tomikawa *et al.*, 1992; Tong *et al.*, 2003; Vyshnevskyy *et al.*, 2005). The geometry of stator (vibrator) can be broadly grouped under three categories: bars, plates and complex structures types. For example, the stators of Dong (Fig. 1.4) and Flynn (Fig. 1.6) are plate type while Kumada (Fig. 1.1), Ohnishi (Fig. 1.3) and Cagatay (Fig. 1.7) stators are of the bar type.

For plates, its size in one dimension, say z direction, is much smaller than the other

two dimensions, say x and y directions. Hence, in-plane extensional, shear or out-of-plane bending are the predominant mode of actuation. The in-plane shape can be rectangular, square, circular or annular. For bars, its size in one dimension, say z direction, is much larger than the other two dimensions, say x and y directions. Therefore, the vibration of a bar can be decomposed into three simple modes - longitudinal, torsional, and transverse (Rayleigh and Lindsay, 1945; Timoshenko *et al.*, 1974). The shape of the cross section can be rectangular, square, circular or annular. Besides these two fundamental types of plates and bars, some complex stator structures which are the combination of plates and bars have also been used, such as Suzuki motor shown in Fig. 1.2.

The variable geometric structure of the stator in USM has an advantage over an electric magnetic motor. An example is the Canon USM (Hosoe, 1989) designed exclusively for the EOS 35 mm camera auto-focus lens, where the large hole in the middle of the ring is for light to pass through.

1.2.3 Piezoelectric materials

It is known that a multi-layer layout is effective in reducing the driving voltage for piezoelectric devices. However, the size of multi-layer structure is only suitable to be used in bar-type stator of USM, such as the stator of Kumada (Fig. 1.1) and Ohnishi (Fig. 1.3).

Two main forms of piezoelectric materials have been used in USM, namely piezoelectric film and bulk PZT (Biwersi *et al.*, 1998; Cagatay *et al.*, 2004, 2003; Koc *et al.*, 2000, 1998; Kurosawa and Ueha, 1991; Morita *et al.*, 1995, 1996, 1998, 1999, 2000b; Muralt, 1999; Muralt *et al.*, 1995; Racine *et al.*, 1998; Saigoh *et al.*, 1995). USMs typically use bulk PZT ceramic plates or bars which exhibit a high level of piezoelectric activity and can generate large forces from moderate applied electric fields, such as the stator of Dong (Fig. 1.4) which is a plate. However, bulk ceramic PZT is relatively fragile and has higher manufacturing cost as it must be individually glued in place.

Researchers shifted the stator design to a composite structure of piezoelectric ceramics on a metal tube, such as the stator of Suzuki (Fig. 1.2) and Cagatay (Fig. 1.7). A PZT ceramic/metal composite tube was used as the stator instead of a simple PZT tube, as a PZT/metal composite stator can produce higher power output, and better reliability.

For miniaturization, some special fabrication techniques for piezoelectric materials have been considered, such as the thin or the thick-film technology. Materials deposited using thin-film techniques, such as, the Flynn motor (Fig. 1.6), exhibit high level of piezoelectric activities. However the thickness is limited to a few microns and this implies that the torque and power generated will be very small. In addition, their deposition processes, being typically sputtering, sol-gel, or hydrothermal techniques, were rather expensive.

Thick films are based on standard screen printing technology, which has been widely used within the microelectronics industry for many years. It can produce thicker layers than thin-film deposition methods. Therefore thick-film printed PZT layers are capable of generating larger actuating forces than thin film layers.

1.2.4 Driving electronics

The driving circuit in USMs can be single, double or even four channels types (Aoyagi *et al.*, 1995; Bai *et al.*, 2004; Iijima *et al.*, 1992; Lebrun *et al.*, 1999; Manceau and Bastien, 1995; Satonobu *et al.*, 2000, 1996; Shimanuki *et al.*, 1994; Takano *et al.*, 1999; Wen *et al.*, 2004, 2003). In principle, USM requires multiple phase electrical actuations to realize the elliptic motion, such as the Dong motor (Fig. 1.4) and the Flynn motor (Fig. 1.6). However, for a miniature USM, single phase actuation has been actively investigated such as Kumada motor (Fig. 1.1) and Cagaty motor (Fig. 1.7). However, the controllability that multiple channels provided makes the USM more stable.

1.2.5 Summary of design considerations

As electromagnetic motors produce relatively low torque at high speed, most applications require that the output first be geared down so as to produce higher torque output at more manageable speeds. Unfortunately, gears not only contribute additional mass, but they also introduce considerable loss and sometimes undesirable backlash. Consequently, the efficiency of a geared motor is notably less than that of the motor alone. Thus, the industry is interested to achieve a simple, low cost and high reliability motor with the advantages such as high torque at low speed, flexible configurable shape and quick response time. This has resulted in the emergence of USM with different designs and characteristics as described above. Most design efforts are confined to the vibration characteristic of stator, form of piezoelectric material, geometry of stator, and driving electric circuit.

For the stator, a circular plate or an annular ring with uniform thickness is widely adopted. However, the application of plates with varying thickness in USM is lacking or not well publicized in the open literature. In addition, in a traveling wave USM such as one with a ring stator, its wave number is fixed at one single value, say 9, after the motor has been assembled. The working resonant frequency corresponding to this wave number is a single value although it may be adjusted within a narrow range in practice. Multi-driving wave-number within one USM may potentially perform better.

1.3 Review on modeling effort of USM

Parallel to the design effort, the numerical modeling of this device has attracted strong interest as it facilitates in-depth understanding and further innovation. Many different numerical models, such as those derived from equivalent electric circuit model, Kirchhoff or Mindlin plate model combined with elastic foundation or half-space contact model, and three-dimensional (3-D) finite element (FE) model, have been developed depending

on the purpose, such as for simulating the overall behavior and for optimizing the design parameters and operational characteristics of USM.

1.3.1 Equivalent electric circuit method

The equivalent electric circuit concept based on electrical and mechanical analogies is briefly introduced as details can be found in the literature (Ikeda, 1990; Mason, 1942, 1958). An inductance, capacitance, and resistance in series satisfy the differential equation

$$L \frac{d^2q}{dt^2} + R \frac{dq}{dt} + \frac{q}{C} = E \quad (1.12)$$

where E is the applied electrical potential; L , R and C are the inductance, resistance and capacitance of the circuit, respectively; and q is the charge. It has the same form as that of the governing equation for an inertial-spring-damping mechanical system given by

$$M \frac{d^2u}{dt^2} + C_d \frac{du}{dt} + Ku = F \quad (1.13)$$

where F is the applied force; M , C_d , and K respectively, are the mass, damping and stiffness of the mechanical system; and u the displacement of M from its equilibrium position. Using such an analogy allows Eq. (1.13) to be solved using well-developed electrical network theory and is especially useful in cases involving electromechanical coupling inherent in USM system. In USM, the stator generally operates at some resonant frequency at which a particular mode shape of vibration can be associated with. By assuming a displacement field based on this mode shape, the stator can be simplified as an inertial-spring-damping system, which in turn can be represented by an equivalent electrical circuit system. The effect of contact interface can be accounted for mainly as frictional losses, which can be analogously represented by a diode and a resistor in series, where the breakdown voltage of the diode is equivalent to the change in state from stick to slip between the stator and the rotor, and the resistance is analogous to the frictional losses. The rotor is simplified as a rotary system with rotary inertia and stiffness, and

similarly represented by an equivalent electrical circuit. The USM is thus simplified as an equivalent electrical circuit with computationally efficient solution (Lerch, 1990; Sherrit *et al.*, 1999), at the expense of simplification in the geometry and contact interface details. However, to accurately compute the model parameters, such as mass, damping, stiffness and force, is still a topic of research (Aoyagi *et al.*, 1996; Chu *et al.*, 2002; Hirata and Ueha, 1993, 1995).

1.3.2 Modeling based on Kirchhoff or Mindlin plate theory

Hagood and McFarland (1995) first presented a complete framework for modeling USM as well as a design tool for optimizing prototypes using plate-based analytical model. The traveling wave dynamics of the stator is simulated using the Kirchhoff thin plate model in conjunction with the Rayleigh-Ritz method and assumed modes, including the modes related to voltage to account for the piezoceramics. Nonlinear normal and tangential contact interface forces between the rotor and stator are obtained by approximating the effect of the rotor as a linear spring (Winkler elastic foundation model). A Runge-Kutta second and third-order routine is utilized to perform time integration with Rayleigh damping. Many published methods can be considered as extension of the framework for stator dynamics and contact interface or both, propounded by Hagood and McFarland (1995). For optimization of frequencies and mode shapes of various stator cross-sectional geometries, Hagedorn and Wallaschek (1992); Hagedorn *et al.* (1993) analysed the free vibration of stator ignoring piezoelectric effect using annular plates with radially varying thickness under Mindlin and Reissner assumption and using the finite difference method. Friend and Stutts (1997), and Ming and Que (2001) using the classical thin plate model, and Sun *et al.* (2002) using the Euler beam model, solved the dynamics of stator by mode superposition in which the piezoelectric effect is considered as externally applied moment to avoid solving the original coupled electric and mechanical field equations. Pons *et al.* (2003, 2004a,b) analysed the stator dynamics based on the Mindlin plate model. For

contact interface, detailed review on contact model including visco-elastic foundation model with/without tangential compliance, elastic half-space and layered elastic half-space in the normal direction and generalized Coulomb friction model in the tangential direction can be found in Wallaschek (1998). Other papers involving contact mechanics in USM include Lu *et al.* (2001a,b) and Storck and Wallaschek (2003) adopting a visco-elastic foundation model, Le Moal and Cusin (1999) adopting an elastic half-space model, and Zhu (2004) adopting a layered elastic half-space model.

The models derived from equivalent electric circuit (1-D), Kirchhoff or Mindlin plate model (2-D) combined with elastic foundation or half-space based contact model are simple and computationally efficient; however, there are shortcomings. Firstly, the piezoelectric coupling effect between the piezoelectric layer and the host structure has been ignored. The improvement to existing models accounting for this coupling effect (Liu *et al.*, 2002; Wang *et al.*, 2001) needs to be investigated. Secondly, the stator dynamics including its resonant frequency, corresponding model shape and vibration amplitude due to piezoelectric actuation cannot be estimated accurately because the presence of piezoelectric ceramics layers and teeth structures necessitate a 3-D model of the geometry of the stator. Thirdly, in 1-D or 2-D based models, the stator bending profile is always assumed to be unaffected by the interface forces, which causes the results of contact stress at the interface between the stator and rotor to be inaccurate.

1.3.3 Finite element analysis

The finite element (FE) method can be used to overcome the shortcomings discussed above. Kagawa *et al.* (1996) used the FE method to simulate the transient dynamic response of piezoelectric coupled stator based on the approach by Allik and Hughes (1970) where the displacements and electrical potential were used as nodal unknowns. The 3-D FE formulations including variables related to the piezoelectric structures were given and the discretized equations of motion solved by Newmark integration routine,

from which the amplitude of stator vibration due to piezoelectric actuation was obtained. Maeno *et al.* (1992) presented a FE analysis of the rotor/stator contact interface in USM. First, the free vibration analysis of stator was performed using the commercial software MSC/NASTRAN[®], in which solid elements were adopted to simulate the complex geometry of the teeth. Using the computed vibration frequency, the amplitude of force vibration of stator was estimated experimentally. The steady-state contact response was then computed assuming the stator performs a prescribed motion. Although the FE analysis of piezoelectric coupled stator dynamics (Kagawa *et al.*, 1996) and steady contact mechanics (Maeno *et al.*, 1992) have been published separately, a complete FE model of an USM for steady and transient overall behavior analysis is still unavailable in the open literature.

1.4 Objective and scope of study

Based on the above review, it can be noted that (a) none of the existing USM analytical models account for the coupling effect between the piezoelectric layer and the host structure; and (b) improvements can be made to accurately model the interaction between piezoelectric coupled dynamics and the non-linear contact (i.e. the whole system including the rotor, stator and piezoelectric layer, should be considered as a coupled dynamic structure). With regards to the design of USM, none of the existing USM (a) caters for the possibility of multi-driving wave-number operation on one motor; and (b) takes into account varying thickness in the actual stator when determining the point of application of the frictional force to effect the rotation of the disk. Therefore, the work accomplished in this thesis is guided by the following two main objectives:

(a). To develop a model for the accurate prediction of piezoelectric traveling wave USM performance. The scope specific to this is a piezoelectric coupled plate model for the dynamics of stator and a FEM model for the overall behavior analysis of USM.

(b). To improve the design of the piezoelectric traveling wave USM by investigating novel multiple driving wave number operation and analyzing of free vibration characteristics of non-uniform thickness stator.

This thesis reports on the attempt to solve the highly nonlinear problem in performance prediction and design of USM. The emphasis is on the FEM analysis of an USM overall behavior, free vibration of the piezoelectric coupled stator, free vibration of the annular plates with varying thickness, and the realization of an USM with multiple wave numbers.

1.5 Outline

Chapter One introduces the background and concept of operation of USMs. A summary of the state-of-the-art and accomplishments to date is given, including the limitations of current design and modeling efforts. Based on the review, the objective of this research is formulated.

Chapter Two presents the solution for the free vibration of non-uniform thickness annular plate. To illustrate the use of the closed form solutions presented, free vibration analyses of a thin annular plate with linear and nonlinear thickness variation are performed and the results compared with published exact solutions and those from 3D FEM.

Chapter Three discusses a model for the stator taking into account piezoelectric coupling effect. An analytical model for the free vibration analysis of piezoelectric coupled thin and thick circular plate is presented. Numerical investigations are performed and the results are verified by the results of three-dimensional finite element analyses using ABAQUS®. The formulation and solution presented is simpler and more compact than that previously published.

Chapter Four proposes a complete three-dimensional finite element (FE) framework combining the piezoelectric coupled stator dynamics and intermittent-contact mechanics to simulate the steady state and transient behavior of ultrasonic motor (USM), which produces fairly accurate results at moderate computational cost. The approaches presented here provide an accurate framework at moderate computation cost for modeling and analysis of USM performance and serve as a design tool for optimizing prototypes.

Chapter Five realizes experimentally an USM with multiple wave numbers. Design, fabrication and characterization of such motor are performed. The experimental performances of the multiple wave numbers USM are presented, and the control variables, wave number and amplitude, compared. As expected, the multiple wave numbers motor significantly outperforms the single wave number motor with regard to the range of speed and torque output, and provides extra control flexibility.

Finally, the conclusions are presented in Chapter Six along with recommendations for further work.

CHAPTER 2

Exact Closed Form Solutions for Transverse Vibration of a Class of Non-Uniform Annular Plates

In an USM, the piezoceramics excite a traveling flexural wave within the stator. This will cause the rotor to be in contact with the stator placed beneath it. The horizontal frictional force between the moving stator surface and the rotor causes the rotor to spin. The contact point to effect rotation of the disk is critical in the construction of an USM. The location of this point is affected by the vibration mode and the variation of the thickness of the stator. In this respect, it would be relevant to study as a preliminary step, the transverse vibration of a non-uniform thickness annular plate, prior to studying that of a piezoelectric coupled annular structure of non-uniform thickness. After a brief background of the vibration of circular plate with varying thickness is addressed in Section 2.1, a variable transform is defined in Section 2.2, which re-casts the governing equation for the vibration of circular plate with varying thickness to a generalized hypergeometric equation. This leads to closed form solutions which are presented in Section 2.3. Their application and comparison of solutions with those from FE analysis are addressed in Sections 2.4 and 2.5.

2.1 Vibration of circular plate with varying thickness

The transverse vibration of plates of various shapes has been studied by many researchers over a long period of time owing to its wide applications in engineering design. The simplicity and widespread use of circular plates are borne by the many publications on their behavior under different boundary conditions. For circular plate with uniform thickness, Airey (1911) and Carrington (1925) gave exact solutions in terms of Bessel functions. Other related references may be found in the well-known work of Leissa (1969) and his subsequent articles (Leissa, 1977, 1978, 1981a,b, 1987a,b).

While considerable work has been done on the vibration of circular plates with uniform thickness, there is no lack of publications on the vibration of thin circular and annular plates with variable thickness either. Since the response of a plate with non-uniform thickness can be formulated as a set of differential equations with variable coefficients, many approximate solutions have been proposed. Raleigh-Ritz method has been applied to obtain approximate frequencies and mode shapes of annular plates with various forms of thickness variations (Bambill *et al.*, 1996; Romanelli and Laura, 1997; Singh and Chakraverty, 1992; Singh and Hassan, 1998; Singh and Saxena, 1995; Thurston and Tsui, 1955). Perturbation method (Yang, 1993) has been employed in analyzing the axi-symmetric free vibration of a circular plate with arbitrary but gradual variation in thickness. The generalized differential quadrature rule (GDQR) was utilized by Wu and Liu (2001) for the free vibration of solid circular plates with variable thickness and elastic constants. In their work, the thickness of the circular plates can vary radially in specific continuous form such as exponential and linear variation. However, these methods are mostly numerical and there are relatively few *analytical* solutions available for plates with variable thickness. Analytical solutions in terms of Bessel functions for axi-symmetric vibrations of circular plate with linear varying thickness and Poisson ratio $\mu = 1/3$ were given by Conway *et al.* (1964). Exact closed form solutions, as a function of the power of

the radius, were obtained by Lenox and Conway (1980) for the transverse vibrations of a thin annular plate having a parabolic thickness variation. Wang (1997) gave a power series solution method for the axi-symmetric vibration of a thin annular plate whose thickness is constant in the circumferential direction but varies arbitrary in the radial direction.

In this chapter, the free vibration analysis of thin annular plate with thickness varying monotonically in the radial direction in arbitrary power form is presented. Transformation of variable is introduced such that the governing equation for the free vibration of varying thickness in power form can be transformed into a fourth-order generalized hypergeometric equation. The corresponding analytical solution in terms of generalized hypergeometric function is presented, which encompasses existing published solutions as special cases. As an illustration, the free vibration solutions of thin annular plate with three types of thickness variations based on the presented solutions are discussed, namely, variation with power of (a) 1 (i.e. linearly increasing thickness), (b) $\frac{1}{2}$ (non-linear increasing thickness), and (c) $-\frac{1}{2}$ (non-linear decreasing thickness). The results are compared with those from three-dimensional (3D) finite element method (FEM). In particular, the change in natural frequency is examined as this has relevance to the operational frequency and characteristics of USM.

2.2 Transformation of governing equation

Consider an annular plate shown in Fig. 2.1, which is generated by rotating the line $z = \pm \frac{1}{2} h_0 \left(\frac{r}{a}\right)^m$ about the z -axis, $0 < b \leq r \leq a$, where b and a are the inner and outer radius of the plate respectively, m is a positive real number and h_0 is the maximum thickness which occurs at the outer radius of the annular plate. When $m < 0$, the rotating line is modified as $z = \pm \frac{1}{2} h_0 \left(\frac{r}{b}\right)^m$ where the method of analysis is the same as that when $m > 0$ by replacing ' a ' with ' b '; hence, only the case $m > 0$ is presented herein. The governing equation using the cylindrical coordinate system for the free vibration of

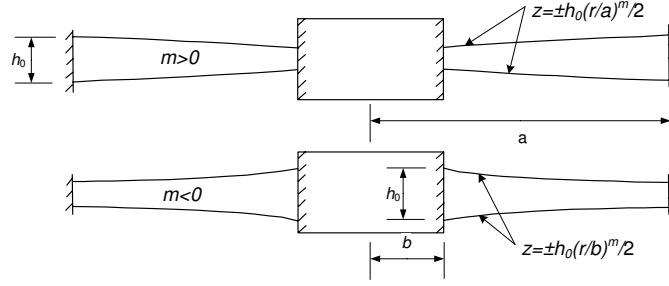


Figure 2.1: Geometry of annular plate with varying thickness

such thin annular plate can be expressed as (Lenox and Conway, 1980)

$$\begin{aligned}
 r^4 \frac{\partial^4 w}{\partial r^4} + (6m + 2)r^3 \frac{\partial^3 w}{\partial r^3} + r^2 [(9m^2 + 3m\mu + 3m - 1) \frac{\partial^2 w}{\partial r^2} + 2 \frac{\partial^4 w}{\partial \theta^2 \partial r^2}] \\
 + r [(9m^2 - 3m\mu - 3m + 1) \frac{\partial w}{\partial r} + (6m - 2) \frac{\partial^3 w}{\partial \theta^2 \partial r}] \\
 + (9m^2 \mu - 9m - 3m\mu + 4) \frac{\partial^2 w}{\partial \theta^2} + \frac{\partial^4 w}{\partial \theta^4} + \frac{12\rho(1 - \mu^2)a^4}{Yh_0^2} \left(\frac{r}{a}\right)^{4-2m} \frac{\partial^2 w}{\partial t^2} = 0
 \end{aligned} \quad (2.1)$$

where Y is the Young's modulus, μ the Poisson ratio. Assume the displacement takes on the separable form:

$$w(r, \theta, t) = z(r)e^{ip\theta}e^{i\omega t} \quad (2.2)$$

Substituting Eq. (2.2) into Eq. (2.1) leads to a homogeneous linear ordinary differential equation with variable coefficients.

$$\begin{aligned}
 r^4 \frac{d^4 z}{dr^4} + (6m + 2)r^3 \frac{d^3 z}{dr^3} + r^2 (9m^2 + 3m\mu + 3m - 1 - 2p^2) \frac{d^2 z}{dr^2} \\
 + r [(9m^2 - 3m\mu - 3m + 1) - (6m - 2)p^2] \frac{dz}{dr} \\
 + [p^4 - (9m^2 \mu - 9m - 3m\mu + 4)p^2 - \frac{12\rho(1 - \mu^2)a^4 \omega^2}{Yh_0^2} \left(\frac{r}{a}\right)^{4-2m}] z(r) = 0
 \end{aligned} \quad (2.3)$$

Solutions for specific simplified forms of Eq. (2.3) have been presented in published literature. When $m = 0$ (i.e. uniform thickness), Eq. (2.3) takes on the usual Bessel function solutions. When $m = 1$ (i.e. linearly varying thickness), $p = 0$ (axi-symmetric vibration), and $\mu = 1/3$, Eq. (2.3) can be simplified to a fourth-order Bessel equation (Conway *et al.*, 1964). When $m = 2$ (i.e. parabolic thickness variation), Eq. (2.3) can be simplified to a fourth-order Euler equation (Lenox and Conway, 1980). There appears to be no other published closed form solutions for annular plate with thickness varying in power form with arbitrary constants.

In this chapter, a variable transformation is defined such that Eq. (2.3) can be transformed into a fourth-order generalized hypergeometric equation, which covers all cases, except for $m = 2$, given by

$$x = \frac{1}{(4-2m)^4} \left(\frac{\omega}{\omega_0}\right)^2 \left(\frac{r}{a}\right)^{4-2m} \quad (2.4)$$

where

$$\omega_0 = \frac{h_0}{a^2} \sqrt{\frac{Y}{12\rho(1-\mu^2)}}$$

Through this transformation, Eq. (2.3) can be written as

$$\left\{ 1 - \frac{1}{x} \prod_{i=1}^4 (\vartheta + \gamma_i - 1) \right\} z(x) = 0 \quad (2.5)$$

where

$$\vartheta = x \frac{\partial}{\partial x}$$

and

$$\begin{aligned} \gamma_i &= 1 - \frac{a_i}{2m-4}, i = 1..4 \\ a_1, a_2 &= -1 + \frac{3}{2}m \mp \frac{1}{2}\sqrt{\Delta_1 + 2\sqrt{\Delta_2}} \\ a_3, a_4 &= -1 + \frac{3}{2}m \mp \frac{1}{2}\sqrt{\Delta_1 - 2\sqrt{\Delta_2}} \\ \Delta_1 &= 9m^2 - 6(1+\mu)m + 4(1+p^2) \\ \Delta_2 &= (9(1-\mu)^2 + 36\mu p^2)m^2 - 24(1+\mu)p^2m + 16p^2 \end{aligned} \quad (2.6)$$

2.3 Closed form solutions

Eq. (2.5) is a generalized hypergeometric equation. According to the Frobenius theory, if no two values of γ_i are equal or differ by an integer value, the solutions of Eq. (2.5) are non-logarithmic and may be written in the form (Pochhammer, 1888; Smith, 1939)

$$\begin{aligned} z_1(x) &= x^{1-\gamma_1} {}_0F_3([], [1+\gamma_2-\gamma_1, 1+\gamma_3-\gamma_1, 1+\gamma_4-\gamma_1], x) \\ z_2(x) &= x^{1-\gamma_2} {}_0F_3([], [1+\gamma_1-\gamma_2, 1+\gamma_3-\gamma_2, 1+\gamma_4-\gamma_2], x) \\ z_3(x) &= x^{1-\gamma_3} {}_0F_3([], [1+\gamma_1-\gamma_3, 1+\gamma_2-\gamma_3, 1+\gamma_4-\gamma_3], x) \\ z_4(x) &= x^{1-\gamma_4} {}_0F_3([], [1+\gamma_1-\gamma_4, 1+\gamma_2-\gamma_4, 1+\gamma_3-\gamma_4], x) \end{aligned} \quad (2.7)$$

where ${}_0F_3([\], [1 + \gamma_2 - \gamma_1, 1 + \gamma_3 - \gamma_1, 1 + \gamma_4 - \gamma_1], x)$ is the generalized hypergeometric function. The series form of the function ${}_pF_q$ is given by

$${}_pF_q([a_1, a_2, \dots, a_p], [b_1, b_2, \dots, b_q], x) = 1 + \sum_{k=1}^{\infty} \frac{\prod_{i=1}^p (a_i)_k x^k}{\prod_{j=1}^q (b_j)_k k!} \quad (2.8)$$

where

$$(a_i)_k = \frac{\Gamma(a_i + k)}{\Gamma(a_i)} = a_i(a_i + 1) \cdots (a_i + k - 1)$$

Since the infinite series of Eq. (2.8) converges for all finite x if $p \leq q$ (Rainville, 1960), the solutions given by Eq. (2.7) are convergent. The complete solution of Eq. (2.5) can be expressed as

$$z(x) = \sum_{i=1}^4 c_i z_i(x) \quad (2.9)$$

where c_i are non-zero constants.

If only λ numbers ($\lambda = 2, 3$ or 4 in the case plate vibration) of γ_i are equal or differ by an integer value, there is no loss of generality in taking λ numbers of γ_i 's as $\gamma_1, \gamma_2, \dots, \gamma_\lambda$, arranged with their real parts in an ascending order. Under these conditions, according to the theory of Frobenius (Smith, 1939), the solutions $z_j(x)$ ($j = 1, \lambda + 1, \dots, 4$) of Eq. (2.5) are given by Eq. (2.7) with the remaining $z_j(x)$ ($j = 2, \dots, \lambda$) in logarithmic form. The detailed derivations of the logarithmic solutions are presented in Appendix B. The results for three cases, which span all possible combinations of γ_i , are given as follows:

(I) When two γ_i 's are equal or differ by an integer value.

Under this case, $\lambda = 2$. $z_1(x)$, $z_3(x)$ and $z_4(x)$ are non-logarithmic solution expressed by Eq. (2.7). The logarithmic solution, $z_2(x)$, is given by

$$z_2(x) = z_1(x) \ln x + x^{1-\gamma_1} \sum_{s=0}^{\infty} \Psi_{0s}^{10} x^s \prod_{i=1}^4 \frac{\Gamma(1 - \gamma_1 + \gamma_i)}{\Gamma(1 - \gamma_1 + \gamma_i + s)} + \prod_{i=2}^4 (\gamma_i - \gamma_1) \frac{1}{x^{\gamma_1}} {}_5F_0([1, 1, 1 + \gamma_1 - \gamma_2, 1 + \gamma_1 - \gamma_3, 1 + \gamma_1 - \gamma_4], [\], \frac{1}{x}) \quad (2.10)$$

where Ψ_{nk}^{ij} is listed in Appendix B.

(II) When three γ 's are equal or differ by an integer value.

Under this case, $\lambda = 3$. Then $z_1(x)$ and $z_4(x)$ are non-logarithmic solutions given by Eq. (2.7). There are two logarithmic solutions, namely $z_2(x)$ given by Eq. (2.10), and $z_3(x)$ which is given by

$$\begin{aligned}
z_3(x) &= 2\bar{z}_2(x) \ln x - z_1(x) \ln^2 x \\
&+ x^{1-\gamma_1} \sum_{s=0}^{\infty} [(\Psi_{0s}^{20})^2 + \Psi_{1s}^{20} + 2\pi^2] x^s \frac{\prod_{i=1}^4 \Gamma(1 - \gamma_1 + \gamma_i)}{\prod_{i=1}^4 \Gamma(1 - \gamma_1 + \gamma_i + s)} \\
&+ 2x^{1-\gamma_2} \sum_{s=1}^{\gamma_2-\gamma_1} (-1)^{1-s} \Gamma(s) \Psi_{0s}^{21} x^{-s} \prod_{i=2}^4 \frac{\Gamma(1 - \gamma_1 + \gamma_i)}{\Gamma(1 - \gamma_1 + \gamma_i - s)} \\
&+ 2(-1)^{\gamma_1+\gamma_2} \Gamma(1 - \gamma_1 + \gamma_2) \frac{\prod_{i=2}^4 \Gamma(1 - \gamma_1 + \gamma_i)}{\prod_{i=3}^4 \Gamma(\gamma_i - \gamma_2)} \\
&\times x^{-\gamma_2} {}_5F_0([1, 1, 1 + \gamma_2 - \gamma_1, 1 + \gamma_2 - \gamma_3, 1 + \gamma_2 - \gamma_4], [], \frac{1}{x})
\end{aligned} \tag{2.11}$$

where $\bar{z}_2(x)$ is listed in Appendix B.

(III) When four γ_i 's are equal or differ by an integer value.

Under this case, $\lambda = 4$. Then $z_1(x)$ is the only non-logarithmic solution given by Eq. (2.7). There are three logarithmic solutions, namely $z_2(x)$ given by Eq. (2.10), $z_3(x)$ by Eq. (2.11) and $z_4(x)$ which is given by

$$\begin{aligned}
z_4(x) &= z_1(x) \ln^3 x - 3\bar{z}_2(x) \ln^2 x + 3\bar{z}_3(x) \ln x \\
&+ \frac{6(-1)^{\gamma_1+\gamma_2}}{\Gamma(\gamma_4 - \gamma_3)} \prod_{i=2}^4 \Gamma(1 - \gamma_1 + \gamma_i) \prod_{i=1}^2 \Gamma(1 - \gamma_i + \gamma_3) \\
&\times x^{-\gamma_3} {}_5F_0([1, 1, 1 + \gamma_3 - \gamma_1, 1 + \gamma_3 - \gamma_2, 1 + \gamma_3 - \gamma_4], [], \frac{1}{x}) \\
&+ 6(-1)^{\gamma_1+\gamma_2} x^{1-\gamma_2} \prod_{i=2}^4 \Gamma(1 - \gamma_1 + \gamma_i) \sum_{s=1}^{\gamma_3-\gamma_2} \frac{\Gamma(\gamma_2 - \gamma_1 + s) \Gamma(s) \Psi_{0s}^{32} x^{-s}}{\prod_{i=3}^4 \Gamma(1 + \gamma_i - \gamma_2 - s)} \\
&+ 3x^{1-\gamma_1} \sum_{s=1}^{\gamma_2-\gamma_1} \Gamma(s) (-1)^{1-s} x^{-s} [(\Psi_{0s}^{31})^2 + \Psi_{1s}^{31} + 2\pi^2] \prod_{i=2}^4 \frac{\Gamma(1 - \gamma_1 + \gamma_i)}{\Gamma(1 - \gamma_1 + \gamma_i - s)} \\
&+ x^{1-\gamma_1} \sum_{s=0}^{\infty} x^s [(\Psi_{0s}^{30})^3 + \Psi_{2s}^{30} + 3\Psi_{0s}^{30}(\Psi_{1s}^{30} + 3\pi^2)] \prod_{i=1}^4 \frac{\Gamma(1 - \gamma_1 + \gamma_i)}{\Gamma(1 - \gamma_1 + \gamma_i + s)}
\end{aligned} \tag{2.12}$$

where $\bar{z}_2(x)$ and $\bar{z}_3(x)$ are listed in Appendix B.

2.4 Some special cases

The generalized hypergeometric function encompasses many other special functions. Thus the proposed solutions can be reduced to other types of special functions for certain combinations of the parameters m , p , and μ . To compare the present solutions with existing published results, some special cases are considered.

2.4.1 Solution for plates with uniform thickness

First consider a uniform plate, that is $m = 0$, for which

$$\gamma_1 = \frac{1}{2} - \frac{p}{4}, \gamma_2 = \frac{1}{2} + \frac{p}{4}, \gamma_3 = 1 - \frac{p}{4}, \gamma_4 = 1 + \frac{p}{4} \quad (2.13)$$

It can be shown that

$$\left. \begin{array}{l} \gamma_1 = \gamma_2 - n \\ \gamma_3 = \gamma_4 - n \end{array} \right\} \text{if } p \text{ is even} \quad (2.14)$$

$$\left. \begin{array}{l} \gamma_1 = \gamma_4 - n \\ \gamma_3 = \gamma_2 - n \end{array} \right\} \text{if } p \text{ is odd}$$

where n is a non-negative integer. Thus whenever p is odd or even, $z_1(x)$ and $z_3(x)$ are always of non-logarithmic form given by Eq. (2.7) while $z_2(x)$ and $z_4(x)$ are always of logarithmic form given by Eq. (2.10). To simplify the solution and reduce to published closed form solution, the relationship between hypergeometric functions $z_1(x)$, $z_3(x)$ and Bessel functions are shown in the following.

The substitution of Eq. (2.13) into Eq. (2.7) gives

$$\begin{aligned} z_1(x) &= x^{\left(\frac{1}{2} + \frac{p}{4}\right)} {}_0F_3\left(\left[\right], \left[1 + \frac{p}{4}, \frac{3}{2}, \frac{3}{2} + \frac{p}{4}\right], x\right) \\ &= \frac{(p+1)!}{2^{(p+2)}} \sum_{k=0}^{\infty} \frac{(2x^{\frac{1}{4}})^{[2(2k+1)+p]}}{(2k+1+p)!(2k+1)!} \end{aligned} \quad (2.15)$$

$$\begin{aligned} z_3(x) &= x^{\frac{p}{4}} {}_0F_3\left(\left[\right], \left[\frac{1}{2} + \frac{p}{2}, \frac{1}{2}, 1 + \frac{p}{2}\right], x\right) \\ &= \frac{p!}{2^p} \sum_{k=0}^{\infty} \frac{(2x^{\frac{1}{4}})^{[2(2k)+p]}}{(2k+p)!(2k)!} \end{aligned} \quad (2.16)$$

The combination of Eqs. (2.15) and (2.16) may be re-written as a combination of the series

$$\sum_{k=0}^{\infty} \frac{(2x^{\frac{1}{4}})^{(2k+p)}}{(k+p)!(k)!} \text{ and } \sum_{k=0}^{\infty} \frac{(-1)^k (2x^{\frac{1}{4}})^{(2k+p)}}{(k+p)!(k)!}$$

or in Bessel function form as

$$I_p(4x^{\frac{1}{4}}) \text{ and } J_p(4x^{\frac{1}{4}})$$

where J is the Bessel function and I is the modified Bessel function of the first kind.

These Bessel function solutions of Eq. (2.5) considering the variable transform of (2.4) are the conventional solutions for plate of uniform thickness (Rayleigh and Lindsay, 1945). The relationship between the hypergeometric functions $z_2(x)$, $z_4(x)$ and Bessel functions can be similarly shown.

2.4.2 Solution for plates with linearly varying thickness

Another special case is for plates with linearly varying thickness. When $\mu = 1/3$, $m = 1$ (linearly varying thickness) and $p = 0$ (axi-symmetric vibration), the solution may be written in terms of Bessel functions (Conway *et al.*, 1964). For this case, γ_i can be obtained according to Eq. (2.4) as

$$\gamma_1 = \frac{1}{2}, \gamma_2 = \frac{3}{2}, \gamma_3 = 1, \gamma_4 = 2 \quad (2.17)$$

Since

$$\gamma_2 - \gamma_1 = 1, \gamma_4 - \gamma_3 = 1$$

$z_1(x)$ and $z_3(x)$ are of non-logarithmic form given by Eq. (2.7). Substituting Eq. (2.17) into Eq. (2.7) gives

$$z_1(x) = x^{\frac{1}{2}} {}_0F_3\left(\left[\right], \left[\frac{3}{2}, 2, \frac{5}{2} \right], x\right) = \frac{3}{2} \sum_{k=0}^{\infty} \frac{(4x^{\frac{1}{2}})^{(2k+1)}}{(2k+1)!(2k+3)!} \quad (2.18)$$

$$z_3(x) = {}_0F_3\left(\left[\right], \left[\frac{1}{2}, \frac{3}{2}, 2 \right], x\right) = \frac{1}{2} \sum_{k=0}^{\infty} \frac{(4x^{\frac{1}{2}})^{(2k)}}{(2k)!(2k+2)!} \quad (2.19)$$

$z_2(x)$ and $z_4(x)$ are of logarithmic form given by Eq. (2.10). Substituting Eq. (2.17) into Eq. (2.10) gives

$$z_2(x) = z_1(x) \ln x + \sqrt{x} \sum_{s=0}^{\infty} \prod_{i=1}^4 \frac{\Gamma(\frac{1}{2} + \gamma_i) \Psi_{0s}^{10} x^s}{\Gamma(\frac{1}{2} + \gamma_i + s)} + \prod_{i=2}^4 (\gamma_i - \frac{1}{2}) \frac{1}{\sqrt{x}} {}_5F_0([1, 1, 0, \frac{1}{2}, -\frac{1}{2}], [\], \frac{1}{x}) \quad (2.20)$$

To obtain $z_4(x)$, re-arrange γ_i shown in Eq. (2.17) as the order $\gamma_1 = 1, \gamma_2 = 2, \gamma_3 = \frac{1}{2}, \gamma_4 = \frac{3}{2}$ and then substituting into Eq. (2.10), one obtains

$$z_4(x) = z_3(x) \ln x + \sum_{s=0}^{\infty} \prod_{i=1}^4 \frac{\Gamma(\gamma_i) \Psi_{0s}^{10} x^s}{\Gamma(\gamma_i + s)} + \prod_{i=2}^4 (\gamma_i - 1) \frac{1}{x} {}_5F_0([1, 1, 0, \frac{3}{2}, \frac{1}{2}], [\], \frac{1}{x}) \quad (2.21)$$

The combination of Eq. (2.18) and Eq. (2.19) may be re-written as a combination of the series

$$\sum_{k=0}^{\infty} \frac{(4x^{\frac{1}{2}})^k}{k!(k+2)!} \text{ and } \sum_{k=0}^{\infty} \frac{(-1)^k (4x^{\frac{1}{2}})^k}{k!(k+2)!}$$

or in Bessel function form as

$$\frac{J_2(4x^{\frac{1}{4}})}{\sqrt{x}} \text{ and } \frac{I_2(4x^{\frac{1}{4}})}{\sqrt{x}}$$

In the same manner, the combination of the other two series in Eq. (2.20) and Eq. (2.21) is a linear combination of the solution

$$\frac{K_2(4x^{\frac{1}{4}})}{\sqrt{x}} \text{ and } \frac{Y_2(4x^{\frac{1}{4}})}{\sqrt{x}}$$

where Y is the Bessel function and K is the modified Bessel function, both of the second kind.

These Bessel function solutions of Eq. (2.5) considering variable transformation (2.4) are the forms presented by Conway *et al.* (1964)

2.5 Numerical examples

2.5.1 Application of logarithmic solution

To check the correctness of the proposed solutions presented in the chapter, the axisymmetric free vibration of an ultra-high molecular weight polyethylene (UHMWPE)

(Evans and Alderson, 1992; Scarpa and Tomlinson, 2000) plate is studied under two types of boundary conditions: C-C, F-C, where the first and second letter denotes the edge condition at the inner and outer edge, respectively, and C denotes clamped and F denotes free. The material properties and geometry of the UHMWPE plate are shown

Table 2.1: Material and geometrical properties of annular plate

Property	Steel	UHMWPE
Young's module Y (GPa)	210	3
Mass density ρ (kg/m ³)	7800	800
Outer radius a (m)	1.0	1.0
Inner radius b (m)	0.1	0.5
Poisson ratio μ	0.3	-19/45

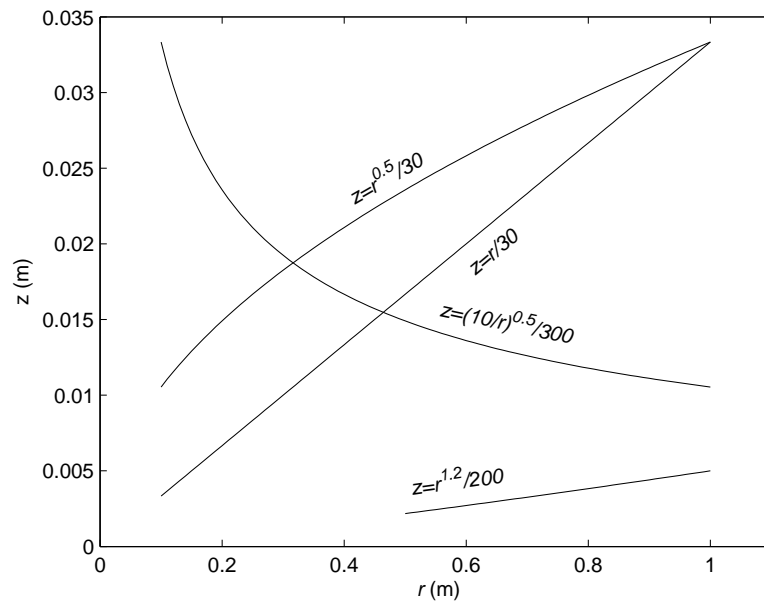


Figure 2.2: Geometry of annular plate with $m = 1, 1/2, -1/2, 6/5$

in Table 2.1 and Fig. 2.2. The reason to choose such material and geometry is that for $m = 6/5$, $\mu = -19/45$ (negative Poisson ratio) and $p = 0$ (axi-symmetric vibration), γ_i according to Eq. (2.4) are $\gamma_1 = 0, \gamma_2 = 1, \gamma_3 = 2, \gamma_4 = 3$, which is the most complex case in the proposed solutions; that is, the free vibration solutions can be written in terms of one non-logarithmic form $z_1(x)$ given by Eq. (2.7) and three logarithmic forms $z_2(x)$, $z_3(x)$ and $z_4(x)$ given by Eqs. (2.10)-(2.12) respectively. A finite element model is also prepared using 13,659 triangular shell elements, STRI3, which is based on Kirchhoff

Table 2.2: Comparison of frequencies (Hz) of annular plate under C-C, F-C boundary conditions between CPT FEM and proposed results for UHMWPE plate

n	p	C-C [†]			F-C		
		FEM	Proposed	Error (%)	FEM	Proposed	Error (%)
0	0	61.991	62.037	0.07%	20.102	20.123	0.10%
	1	166.42	168.04	0.96%	76.381	76.609	0.30%
	2	324.10	326.97	0.88%	182.70	183.74	0.57%

p = number of nodal diameters.

n = number of nodal circles.

C = clamped, F = free.

[†]The first letter denotes the condition at the inner edge.

thin plate theory (CPT), to assess the validity of the results provided by the analytical approach. Lanczos iterative technique was adopted to compute the fundamental natural frequency of the plate. The analytical and numerical results are compared in Table 2.2. The good agreement of less than 1% maximum difference indicates that the correctness of the proposed solutions in this chapter, especially for the case of materials with negative Poisson's ratio.

2.5.2 Effect of plate with varying thickness

To investigate the application of the proposed solutions in conventional materials, consider an annular steel plate where the Young's modulus, mass density and geometric parameters are listed in Table 2.1. Fig. 2.2 plots the geometry of each annular plate. Their FEM mesh are prepared using 3D solid element with 20 nodes, C3D20R, and Lanczos iterative technique with $m = 1$ (linear increasing thickness, 1,242 elements), $m = 1/2$ (non-linear increasing thickness, positive power, 3,195 elements), and $m = -1/2$ (non-linear decreasing thickness, negative power, 2,880 elements). The frequencies for the free vibration of the above plate with 0 to 2 diametrical nodes and 0 to 2 nodal circles are investigated using the solution of Eq. (2.7) and compare well with those from 3D FEM obtained using ABAQUS[®] 6.3, as summarized in Table 2.3. For example, when $m = 1$, $1/2$ and $-1/2$, the respective maximum errors of 2.4%, 6.8% and 3.4% occur at $p = 2$ and $n = 2$ under clamped-clamped boundary condition respectively. Such agreement shows

Table 2.3: Comparison of frequencies (Hz) of annular plate under C-C, F-C boundary conditions between 3D FEM and proposed results for $m = 1, 1/2, -1/2$

$m=1$							
n	p	C-C [†]			F-C		
		FEM	Proposed	Error (%)	FEM	Proposed	Error (%)
0	0	223.460	223.772	0.14%	149.250	149.603	0.24%
	1	258.170	258.972	0.31%	218.330	219.379	0.48%
	2	363.450	366.295	0.78%	352.450	355.647	0.91%
1	0	580.010	582.352	0.40%	382.440	385.354	0.76%
	1	618.090	622.285	0.68%	468.700	473.471	1.02%
	2	737.360	747.363	1.36%	665.410	675.195	1.47%
2	0	1097.600	1114.610	1.55%	750.720	762.903	1.62%
	1	1136.600	1156.676	1.77%	833.160	848.420	1.83%
	2	1257.900	1287.404	2.35%	1055.900	1079.504	2.24%

$m=1/2$							
n	p	C-C [†]			F-C		
		FEM	Proposed	Error (%)	FEM	Proposed	Error (%)
0	0	302.120	306.027	1.29%	153.210	153.859	0.42%
	1	336.990	342.054	1.50%	273.710	276.750	1.11%
	2	459.550	468.545	1.96%	444.780	452.562	1.75%
1	0	821.290	849.045	3.38%	491.620	499.910	1.69%
	1	869.350	900.462	3.58%	670.370	688.640	2.73%
	2	1027.200	1069.060	4.08%	956.330	989.164	3.43%
2	0	1573.400	1669.238	6.09%	1044.400	1081.779	3.58%
	1	1626.600	1728.966	6.29%	1229.000	1286.276	4.66%
	2	1797.400	1919.878	6.81%	1610.100	1699.110	5.53%

$m=-1/2$							
n	p	C-C [†]			C-F		
		FEM	Proposed	Error (%)	FEM	Proposed	Error (%)
0	0	223.240	224.421	0.53%	47.783	47.813	0.06%
	1	227.610	229.730	0.93%	235.320	237.822	1.06%
	2	261.450	264.359	1.11%	277.680	281.165	1.26%
1	0	584.750	594.186	1.61%	227.030	228.568	0.68%
	1	597.870	609.392	1.93%	605.200	617.117	1.97%
	2	658.090	671.925	2.10%	669.630	684.120	2.16%
2	0	1112.500	1145.732	2.99%	590.600	600.318	1.65%
	1	1132.200	1168.831	3.24%	1139.100	1175.481	3.19%
	2	1212.400	1253.376	3.38%	1222.500	1263.459	3.35%

p = number of nodal diameters.

n = number of nodal circles.

C = clamped, F = free.

[†]The first letter denotes the condition at the inner edge.

that the proposed solutions based on CPT are closed to those from FE analysis based on 3D elasticity theory.

The variation of the ratio of frequencies for plates with varying thickness having maximum thickness $h_0 = 1/15$ to those for a plate with uniform thickness of $h_0 = 1/15$ under clamped-clamped boundary conditions is plotted in Fig. 2.3. The variation of the

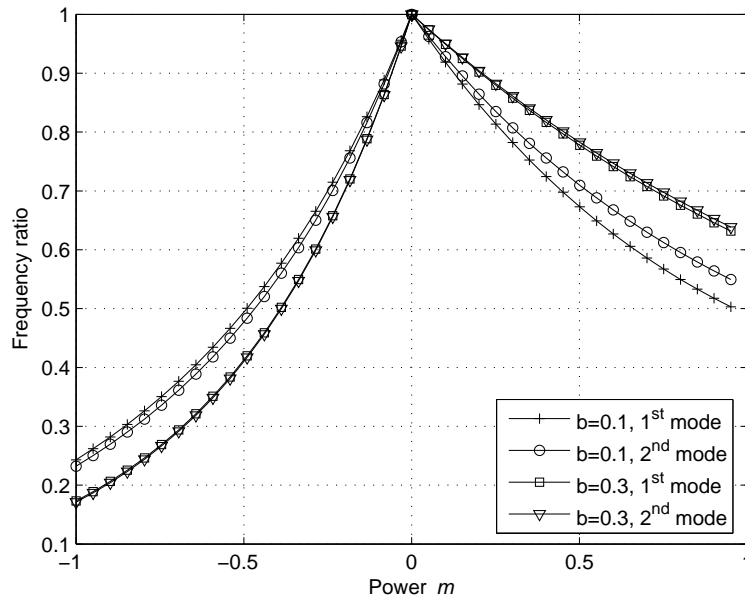


Figure 2.3: Frequency ratio (varying thickness to uniform plate) for different m

first two frequencies with the taper (represented by the power of thickness function) of the plate is illustrated. When the power m is in the range of -1 to 0, the thickness tapers from a value of h at the centre to a smaller value at the circumference. The natural frequency, say ω_N , will be lower than that of a uniform plate of thickness h , say ω_U . As m increases from -1 to 0, the taper reduces until the plate thickness reaches h when $m = 0$, implying that the natural frequency increases from ω_N to ω_U . This is reflected in Fig. 2.3. Similarly, when the power m is in the range from 0 to 1, the thickness tapers from h at the outer edge to a smaller value at the centre. The natural frequency, say ω_P , will be lower than ω_U . As m decreases from 1 to 0, the taper reduces until the plate thickness reaches h when $m = 0$, implying that the natural frequency increases from ω_P to ω_U . This is again consistent with the results of Fig. 2.3. Since $\omega_P > \omega_N$ as the plate is

stiffer where more materials are concentrated towards the circumference, it is consistent that the negative power of thickness function have much effect on the frequencies of the plate than positive power. In addition, when the inner radius b increases, the variation of the frequencies of the plate with negative power varying thickness became larger while that of the plate with positive power varying thickness decreases. This is because the mass of the plate with negative power varying thickness decreases much more than that of the plate with positive power varying thickness with the increased inner radius b .

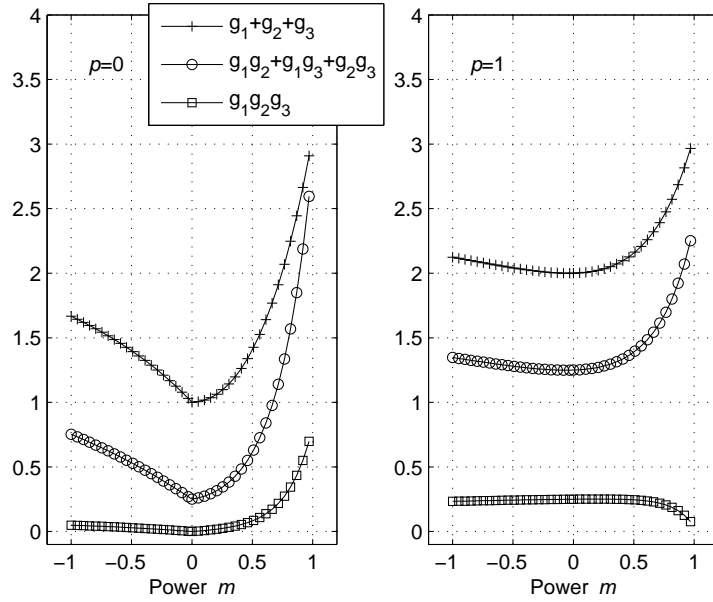


Figure 2.4: Convergence conditions for different m and p (where $g_1 = \gamma_2 - \gamma_1, g_2 = \gamma_3 - \gamma_1, g_3 = \gamma_4 - \gamma_1$)

Another issue to note is the different convergence conditions of hypergeometric functions under negative and positive powers. From Eq. (2.7), one can see the rate of convergence of hypergeometric function is dependent on these difference $g_1 = \gamma_2 - \gamma_1, g_2 = \gamma_3 - \gamma_1$ and $g_3 = \gamma_4 - \gamma_1$. Fig. 2.4 plots the summation of $g_i (i = 1 \dots 3)$ and their bi- and tri-product. For $p = 0$, it is easy to see the slowest convergence rate occurs at m near zero and such conclusion may not hold for $p = 1$; in general, trial and error may be necessary to ensure convergence. In this chapter, all hypergeometric functions are calculated using 20 terms because the 21st term is less than 10^{-30} even for the slowest convergence case.

2.6 Conclusions

The general analytical solutions in terms of generalized hypergeometric function for the free vibration of thin annular plate with thickness varying monotonically in arbitrary power form are presented, which agree with published solutions as special cases. The solutions are verified by comparing with those from Kirchhoff-based and 3D FEM for plates with linear increasing, non-linear increasing and non-linear decreasing thicknesses in the radial direction. The results are consistent, indicating that the negative power of thickness function have a greater effect on the frequencies of the plate than positive power. In addition, when the inner radius b increases, the variation of the frequencies of the plate with negative power varying thickness became larger while that of the plate with positive power varying thickness decreases. Although the solution technique presented in this chapter is based on Kirchhoff plate model, the same approach can be used to solve the free vibration problem of thick plate with varying thickness based on the Mindlin plate model.

CHAPTER 3

Free Vibration Analysis of Piezoelectric Coupled Thin and Thick Annular Plate

In an USM, the stator is usually modeled as an annular plate with surface-mounted piezoceramics patches. As discussed in Chapter 1, the analysis of stator with full piezoelectric coupling effect is important for the design of USMs. However, piezoelectric coupled effect and the laminated nature of the stator have not been modeled and published completely in the open literature. Hence, there may be a need to provide a more accurate model to fully study the coupled piezoelectric effect. In Chapter 2, the free vibration analysis of annular plate with non-uniform thickness has been performed to find the effect of varying thickness on the resonant frequencies of the plate. In this chapter, the coupling effect between the piezoelectric layer and the host structure is investigated to show its relationship with the resonant frequencies of the plate. After a brief background on the vibration of piezoelectric coupled structures in Section 3.1, the strain and stress components in piezoelectric sandwich plate are introduced in Section 3.2. Kirchhoff and Mindlin plate theories are addressed in Sections 3.3 and 3.4. The results are compared with those from FE analysis in Section 3.5.

3.1 Vibration of piezoelectric coupled plates

The study of embedded or surface-mounted piezoelectric materials in structures has received considerable attention in recent years because piezoelectric materials are more extensively used either as actuators or sensors. In order to effectively utilize the piezoelectric effect and actuating properties of piezoelectric materials, the interaction between the host structure and piezoelectric patch must be well understood. Ding *et al.* (1996) obtained the general solution for the dynamic response of a transversely isotropic piezoelectric medium. Chen (1996) simplified the equations of motion of a spherically isotropic elastic medium with radial non-homogeneity by adopting three displacement functions and considered some vibration problems of spherical shells. Sun and Zhang (1995) and Zhang and Sun (1999) presented their research on the analysis of a sandwich beam and plate structure containing a piezoelectric core, where an electric field in the thickness direction may generate shear deformation within the core. Models for composite structures with piezoelectric materials as sensors and actuators have also been published (Han and Lee, 1998; Na and Librescu, 1998). In the latter addressing the mechanics model for the analysis of the coupled structure, the distribution of the electric potential is assumed to be uniform in the longitudinal direction of the piezoelectric actuator and linear in its thickness direction, which may violate Maxwell static electricity equation. Wang *et al.* (2001) and Liu *et al.* (2002) presented their research on the free vibration of piezoelectric sandwich thin and thick circular plates, respectively. Their hypothesis that the distribution of electric potential along the thickness direction in piezoelectric layer can be represented by a sinusoidal function was validated by FE and analytical solutions satisfying Maxwell static electricity equation were presented.

In the present work, through the transformation of variable suggested by Mindlin (1951), analytical solutions for the free vibration of piezoelectric coupled annular plate based on Kirchhoff plate model (otherwise known as classical plate theory, or in short,

CPT) and the Mindlin plate model (also known as improved plate theory or FSDT) are presented. A sinusoidal function (Wang *et al.*, 2001) is used to describe the distribution of electric potential along the thickness direction of both thin and thick plates. Maxwell static electricity equation is included as one of the governing equations. Numerical investigations are performed for annular plates bonded by two piezoelectric layers and the results are verified against three-dimensional (3D) FE analysis using ABAQUS® Version 6.3. The applicability of the proposed models is examined by studying the effect of different thickness ratios of piezoelectric layer to host plate on the vibration of annular plate. Comparing with the published solutions of piezoelectric coupled plate (Wang *et al.*, 2001; Liu *et al.*, 2002), the proposed solutions are more compact and simpler because by using variables transformation, the governing equation - one 6th order differential equation can be decoupled to three 2nd order differential equations.

3.2 Strain and stress components in piezoelectric sandwich plate

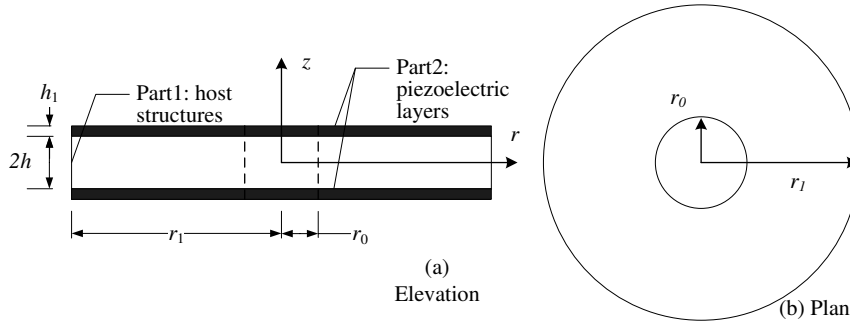


Figure 3.1: Annular plate surface-mounted with two piezoelectric layers

Fig. 3.1 shows the cross section of a laminated annular plate consisting of one host layer and two piezoelectric layers. Both top and bottom surfaces of each piezoelectric layer are fully covered by electrodes that are shortly connected. The cylindrical coordinate system is adopted where the $r-\theta$ plane is coincident with the mid-plane of the undeformed plate. For such plate structures, the bending and twisting moments, and the transverse

shearing forces (all in per unit of length) are defined in the customary manner

$$(M_{rr}, M_{\theta\theta}, M_{r\theta}) = \int (\sigma_{rr}, \sigma_{\theta\theta}, \tau_{r\theta})zdz \quad (3.1a)$$

$$(Q_r, Q_\theta) = \int (\tau_{rz}, \tau_{\theta z})zdz \quad (3.1b)$$

where σ_{rr} , $\sigma_{\theta\theta}$ are normal stress components, and $\tau_{r\theta}$, τ_{rz} , $\tau_{\theta z}$ are shear stress components in the plate.

The kinematic fields in the host plate and piezoelectric layer are given by

$$\epsilon_{rr} = \frac{\partial u_r}{\partial r} \quad (3.2a)$$

$$\epsilon_{\theta\theta} = \frac{u_r}{r} + \frac{\partial u_\theta}{r\partial\theta} \quad (3.2b)$$

$$\gamma_{r\theta} = \frac{\partial u_r}{r\partial\theta} + \frac{\partial u_\theta}{\partial r} - \frac{u_\theta}{r} \quad (3.2c)$$

$$\gamma_{rz} = \frac{\partial u_r}{\partial z} + \frac{\partial u_z}{\partial r} \quad (3.2d)$$

$$\gamma_{\theta z} = \frac{\partial u_\theta}{\partial z} + \frac{\partial u_z}{r\partial\theta} \quad (3.2e)$$

where ϵ_{rr} , $\epsilon_{\theta\theta}$, $\gamma_{r\theta}$, γ_{rz} , and $\gamma_{\theta z}$ are the normal and shear strain components, respectively; and u_z , u_r , and u_θ are the displacements in the transverse, radial and tangential direction of the plate, respectively.

The constitutive relations in the host plate are expressed as

$$\sigma_{rr}^h = \frac{Y}{1-\mu^2}(\epsilon_{rr} + \mu\epsilon_{\theta\theta}) \quad (3.3a)$$

$$\sigma_{\theta\theta}^h = \frac{Y}{1-\mu^2}(\epsilon_{\theta\theta} + \mu\epsilon_{rr}) \quad (3.3b)$$

$$\tau_{r\theta}^h = \frac{Y}{2(1+\mu)}\gamma_{r\theta} \quad (3.3c)$$

$$\tau_{rz}^h = \frac{Y\kappa^2}{2(1+\mu)}\gamma_{rz} \quad (3.3d)$$

$$\tau_{\theta z}^h = \frac{Y\kappa^2}{2(1+\mu)}\gamma_{\theta z} \quad (3.3e)$$

where the superscript h represents the variables in the host structure; Y and μ are the Young's modulus and Poisson ratio of the host material; and κ^2 is the shear factor in Mindlin plate model (Mindlin, 1951) to correct for the shear modulus, chosen as $\pi^2/12$ here.

The constitutive relations in the piezoelectric layer are written as (Wang *et al.*, 2001; Liu *et al.*, 2002)

$$\sigma_{rr}^E = \bar{C}_{11}^E \epsilon_{rr} + \bar{C}_{12}^E \epsilon_{\theta\theta} - \bar{e}_{31} E_z \quad (3.4a)$$

$$\sigma_{\theta\theta}^E = \bar{C}_{12}^E \epsilon_{rr} + \bar{C}_{11}^E \epsilon_{\theta\theta} - \bar{e}_{31} E_z \quad (3.4b)$$

$$\tau_{r\theta}^E = \frac{1}{2}(\bar{C}_{11}^E - \bar{C}_{12}^E)\gamma_{r\theta} \quad (3.4c)$$

$$\tau_{rz}^E = \kappa^2 C_{55}^E \gamma_{rz} + e_{15} E_r \quad (3.4d)$$

$$\tau_{\theta z}^E = \kappa^2 C_{55}^E \gamma_{\theta z} + e_{15} E_\theta \quad (3.4e)$$

where the superscript E represents the variables in the piezoelectric material; $\bar{C}_{11}^E, \bar{C}_{12}^E$ and \bar{e}_{31} are the reduced material constants of the piezoelectric medium for plane stress problems given by $\bar{C}_{11}^E = C_{11}^E - (C_{13}^E)^2/C_{33}^E$, $\bar{C}_{12}^E = C_{12}^E - (C_{13}^E)^2/C_{33}^E$ and $\bar{e}_{31}^E = e_{31} - C_{11}^E e_{33}/C_{33}^E$; $C_{11}^E, C_{12}^E, C_{13}^E, C_{33}^E$ and C_{55}^E are the moduli of elasticity under constant electric field; e_{31}, e_{33} and e_{15} are the piezoelectric constants; and E_z, E_r and E_θ are the electric field intensities in the radial, tangential and transverse direction, respectively. The latter are given by

$$E_r = -\frac{\partial\phi}{\partial r} \quad (3.5a)$$

$$E_\theta = -\frac{\partial\phi}{r\partial\theta} \quad (3.5b)$$

$$E_z = -\frac{\partial\phi}{\partial z} \quad (3.5c)$$

where ϕ is the electric potential at any point of the piezoelectric layers. The corresponding electric displacements D_r, D_θ and D_z are given by

$$D_r = e_{15}\gamma_{rz} + \varepsilon_{11}E_r \quad (3.6a)$$

$$D_\theta = e_{15}\gamma_{\theta z} + \varepsilon_{11}E_\theta \quad (3.6b)$$

$$D_z = \bar{e}_{31}(\epsilon_{rr} + \epsilon_{\theta\theta}) + \bar{\varepsilon}_{33}E_z \quad (3.6c)$$

where $\bar{\varepsilon}_{33}$ is the reduced dielectric constant, ε_{11} and ε_{33} are the dielectric constants, all of the piezoelectric layer, and $\bar{\varepsilon}_{33} = \varepsilon_{33} + e_{33}^2/C_{33}^E$.

3.3 Piezoelectric sandwich Kirchhoff plate

In most practical applications of piezoelectric coupled annular plate shown in Fig. 3.1, the ratio of its radius to the thickness of host plate is more than ten. As such, Kirchhoff assumption for thin plates is applicable, where shear deformation and rotary inertia can be omitted.

3.3.1 Basic equations

The displacement field in Kirchhoff plate is assumed as follows

$$u_r = -z \frac{\partial u_z}{\partial r} \quad (3.7a)$$

$$u_\theta = -z \frac{\partial u_z}{r \partial \theta} \quad (3.7b)$$

$$u_z = w(r, \theta, t) \quad (3.7c)$$

where $w(r, \theta, t)$ is the transverse displacement of the mid-plane. The distribution of the electric potential in the thickness direction is assumed to be sinusoidal (Wang *et al.*, 2001), that is

$$\phi = \varphi(r, \theta, t) \sin\left(\frac{\pi(z-h)}{h_1}\right) \quad (3.8)$$

where φ is the electric potential on the mid-surface of the piezoelectric layer; h and h_1 are the thickness of the host plate and the piezoelectric layer, respectively.

The resultant moments and shear forces can be expressed as follows by substituting Eqs. (3.2)-(3.8) into Eq. (3.1)

$$M_{rr} = -[(d_1 + d_2) \frac{\partial^2 w}{\partial r^2} + (d_1 + d_2 - 2A_1) \left(\frac{\partial w}{r \partial r} + \frac{\partial^2 w}{r^2 \partial \theta^2} \right) + \frac{4}{\pi} h_1 \bar{e}_{31} \varphi] \quad (3.9a)$$

$$M_{\theta\theta} = -[(d_1 + d_2 - 2A_1) \frac{\partial^2 w}{\partial r^2} + (d_1 + d_2) \left(\frac{\partial w}{r \partial r} + \frac{\partial^2 w}{r^2 \partial \theta^2} \right) + \frac{4}{\pi} h_1 \bar{e}_{31} \varphi] \quad (3.9b)$$

$$M_{r\theta} = -2A_1 \left(\frac{\partial^2 w}{r \partial r \partial \theta} - \frac{\partial^2 w}{r^2 \partial \theta^2} \right) \quad (3.9c)$$

$$Q_r = -[(d_1 + d_2) \frac{\partial}{\partial r} \Delta w + \frac{4}{\pi} h_1 \bar{e}_{31} \frac{\partial \varphi}{\partial r}] \quad (3.10a)$$

$$Q_\theta = -\frac{1}{r} [(d_1 + d_2) \frac{\partial}{\partial \theta} \Delta w + \frac{4}{\pi} h_1 \bar{e}_{31} \frac{\partial \varphi}{\partial \theta}] \quad (3.10b)$$

where

$$d_1 = \frac{2}{3} \frac{Yh^3}{1 - \mu^2}, \quad d_2 = \frac{2}{3} C_{11}^E [(h + h_1)^3 - h^3]$$

and

$$A_1 = \frac{1}{2} [(1 - \mu)d_1 + (1 - \frac{C_{12}^E}{C_{11}^E})d_2]$$

The governing equation for the Kirchhoff plate is given by

$$\frac{\partial Q_r}{\partial r} + \frac{\partial Q_\theta}{r \partial \theta} + \frac{Q_r}{r} = \int_{-h}^h \rho_1 \frac{\partial^2 u_z}{\partial t^2} dz + 2 \int_h^{h+h_1} \rho_2 \frac{\partial^2 u_z}{\partial t^2} dz \quad (3.11)$$

where ρ_1 and ρ_2 are the material densities of the host material and piezoelectric layer, respectively.

The electric variables must also satisfy the Maxwell equations which require that the divergence of the electric flux vanishes at any point within the piezoelectric layers. This condition can be satisfied approximately by enforcing the integration of the divergence of the electric flux across the thickness of the piezoelectric layers to vanish for any r and θ

$$\int_h^{h+h_1} (\frac{\partial(rD_r)}{r \partial r} + \frac{\partial D_\theta}{r \partial \theta} + \frac{\partial D_z}{\partial z}) dz = 0 \quad (3.12)$$

The solutions of w and ϕ for wave propagation in θ direction can be written as

$$w(r, \theta, t) = \bar{w}(r) e^{i(p\theta - \omega t)} \quad (3.13a)$$

$$\varphi(r, \theta, t) = \bar{\varphi}(r) e^{i(p\theta - \omega t)} \quad (3.13b)$$

Substituting Eq. (3.13) into Eqs. (3.11) and (3.12) gives

$$(d_1 + d_2) \Delta \Delta \bar{w} + \frac{4}{\pi} h_1 \bar{e}_{31} \Delta \bar{\varphi} - A_2 \omega^2 \bar{w} = 0 \quad (3.14a)$$

$$\frac{h_1^2 \varepsilon_{11}}{\pi^2 \bar{\varepsilon}_{33}} \Delta \bar{\varphi} - \bar{\varphi} + \frac{h_1^2 \bar{e}_{31}}{2\pi^2 \bar{\varepsilon}_{33}} = 0 \quad (3.14b)$$

where

$$\Delta = \frac{\partial^2}{\partial r^2} + \frac{\partial}{r\partial r} - \frac{p^2}{r^2}, A_2 = 2(\rho_1 h + \rho_2 h_1)$$

3.3.2 Solutions for w and ϕ

To solve for w and ϕ , transformation of variable, similar to that in existing reference (Ding *et al.*, 1996), is adopted. That is,

$$\bar{\varphi} = x\bar{w} \quad (3.15)$$

where x is a constant. Substituting Eq. (3.15) into Eq. (3.14), gives

$$\Delta[\Delta\bar{w} - \frac{A_2\omega^2 h_1^2(2\varepsilon_{11}x + \bar{e}_{31}\pi) - 8\pi\bar{\varepsilon}_{33}\bar{e}_{31}h_1x^2}{2\pi^2\bar{\varepsilon}_{33}(d_1 + d_2)}\bar{w}] = 0 \quad (3.16a)$$

$$\Delta\bar{w} - \frac{2\pi^2\bar{\varepsilon}_{33}x}{h_1^2(2\varepsilon_{11}x + \bar{e}_{31}\pi)}\bar{w} = 0 \quad (3.16b)$$

The solution for \bar{w} is unique under the following conditions

$$\frac{A_2\omega^2 h_1^2(2\varepsilon_{11}x + \bar{e}_{31}\pi) - 8\pi\bar{\varepsilon}_{33}\bar{e}_{31}h_1x^2}{2\pi^2\bar{\varepsilon}_{33}(d_1 + d_2)x} = \frac{2\pi^2\bar{\varepsilon}_{33}x}{h_1^2(2\varepsilon_{11}x + \bar{e}_{31}\pi)} \quad (3.17a)$$

$$\frac{2\pi^2\bar{\varepsilon}_{33}x}{h_1^2(2\varepsilon_{11}x + \bar{e}_{31}\pi)} = \lambda \quad (3.17b)$$

where λ is a constant. Under the above condition, Eq. (3.16) can be reduced to

$$\Delta\bar{w} - \lambda\bar{w} = 0 \quad (3.18)$$

Eq. (3.17a) is cubic in x , which given three roots, $x_i (i = 1, 2, 3)$ and $\lambda_i (i = 1, 2, 3)$ can be calculated correspondingly from Eq. (3.17b). Three sets of Bessel functions $c_i w_{i1}(p, \delta_i r) + c_{i+3} w_{i2}(p, \delta_i r)$, $i = 1, 2, 3$ where $\delta_i = \sqrt{|\lambda_i|}$ can be obtained by substituting $\lambda_i (i = 1, 2, 3)$ into Eq. (3.18). The final solutions are given as

$$w = \sum_{i=1}^3 [c_i w_{i1}(p, \delta_i r) + c_{i+3} w_{i2}(p, \delta_i r)] e^{i(p\theta - \omega t)} \quad (3.19a)$$

$$\varphi = \sum_{i=1}^3 x_i [c_i w_{i1}(p, \delta_i r) + c_{i+3} w_{i2}(p, \delta_i r)] e^{i(p\theta - \omega t)} \quad (3.19b)$$

where

$$\begin{aligned} w_{i1}(p, \delta_i r) &= \begin{cases} J_p(\delta_i r) & \lambda_i < 0 \\ I_p(\delta_i r) & \lambda_i > 0 \end{cases} \\ w_{i2}(p, \delta_i r) &= \begin{cases} Y_p(\delta_i r) & \lambda_i < 0 \\ K_p(\delta_i r) & \lambda_i > 0 \end{cases} \end{aligned} \quad (3.20)$$

$$i = 1, 2, 3$$

in which J and Y are Bessel functions of the first and second kind, respectively; I and K are modified Bessel functions of the first and second kind, respectively; and $c_i (i = 1, \dots, 6)$ are six constants of integration.

As usual, the determinant of the matrix containing the system frequencies is considered after imposing the electric and displacement boundary conditions. If the plate is insulated at the edge, the electrical flux conservation equation is given by

$$\int_h^{h+h_1} D_r(r, \theta, t) dz = 0 \quad (3.21)$$

Substituting Eq. (3.6a) into Eq. (3.21) in view of $\gamma_{rz} = 0$, yields the electric boundary condition

$$\frac{\partial \varphi}{\partial r} = 0 \quad (3.22)$$

The standard boundary conditions for the clamped, simply supported and free ends are given respectively as follows (Wang *et al.*, 2001; Liu *et al.*, 2002):

(a) clamped:

$$\begin{aligned} w(r_1, \theta, t) &= \frac{\partial w}{\partial r} \Big|_{r=r_1} = \frac{\partial \varphi}{\partial r} \Big|_{r=r_1} = 0 \\ w(r_0, \theta, t) &= \frac{\partial w}{\partial r} \Big|_{r=r_0} = \frac{\partial \varphi}{\partial r} \Big|_{r=r_0} = 0 \end{aligned} \quad (3.23)$$

(b) simply supported:

$$\begin{aligned} w(r_1, \theta, t) &= M_{rr}(r_1, \theta, t) = \frac{\partial \varphi}{\partial r} \Big|_{r=r_1} = 0 \\ w(r_0, \theta, t) &= M_{rr}(r_0, \theta, t) = \frac{\partial \varphi}{\partial r} \Big|_{r=r_0} = 0 \end{aligned} \quad (3.24)$$

(c) free:

$$\begin{aligned} M_{rr}(r_1, \theta, t) &= Q(r_1, \theta, t) = \frac{\partial \varphi}{\partial r} \Big|_{r=r_1} = 0 \\ M_{rr}(r_0, \theta, t) &= Q(r_0, \theta, t) = \frac{\partial \varphi}{\partial r} \Big|_{r=r_0} = 0 \end{aligned} \quad (3.25)$$

For all possible combinations of clamped, simply-supported and free edge conditions at the inner ($r = r_1$) and outer ($r = r_0$) circular boundaries of the annular plate in Fig. 3.1, a matrix involving the system frequencies can always be formulated. For example, the determinant of frequencies under clamped-clamped (C-C) boundary condition is given by substituting Eq. (3.19) into Eq. (3.23), resulting in

$$\begin{vmatrix} w_{11}(p, \delta_1 r_1) & w_{12}(p, \delta_1 r_1) & w_{21}(p, \delta_2 r_1) & w_{22}(p, \delta_2 r_1) & w_{31}(p, \delta_3 r_1) & w_{32}(p, \delta_3 r_1) \\ w'_{11}(p, \delta_1 r_1) & w'_{12}(p, \delta_1 r_1) & w'_{21}(p, \delta_2 r_1) & w'_{22}(p, \delta_2 r_1) & w'_{31}(p, \delta_3 r_1) & w'_{32}(p, \delta_3 r_1) \\ x_1 w_{11}(p, \delta_1 r_1) & x_1 w_{12}(p, \delta_1 r_1) & x_2 w_{21}(p, \delta_2 r_1) & x_2 w_{22}(p, \delta_2 r_1) & x_3 w_{31}(p, \delta_3 r_1) & x_3 w_{32}(p, \delta_3 r_1) \\ w_{11}(p, \delta_1 r_0) & w_{12}(p, \delta_1 r_0) & w_{21}(p, \delta_2 r_0) & w_{22}(p, \delta_2 r_0) & w_{31}(p, \delta_3 r_0) & w_{32}(p, \delta_3 r_0) \\ w'_{11}(p, \delta_1 r_0) & w'_{12}(p, \delta_1 r_0) & w'_{21}(p, \delta_2 r_0) & w'_{22}(p, \delta_2 r_0) & w'_{31}(p, \delta_3 r_0) & w'_{32}(p, \delta_3 r_0) \\ x_1 w_{11}(p, \delta_1 r_0) & x_1 w_{12}(p, \delta_1 r_0) & x_2 w_{21}(p, \delta_2 r_0) & x_2 w_{22}(p, \delta_2 r_0) & x_3 w_{31}(p, \delta_3 r_0) & x_3 w_{32}(p, \delta_3 r_0) \end{vmatrix} \quad (3.26)$$

where the prime $'$ denotes $\partial/\partial r$; and w_{ij} is given in Eq. (3.20). Setting Eq. (3.26) to zero yields the resonant frequencies and their corresponding mode shapes.

3.4 Piezoelectric sandwich Mindlin plate

In some applications of piezoelectric sandwich plate, the number of nodal diameters (i.e. number of zeros in the θ -direction) is relatively large and the wavelength is not necessarily small compared to the plate thickness. This suggests that shear deformations and/or the rotary inertia have to be taken into account.

3.4.1 Basic equations

Mindlin (1951) and Mindlin and Medick (1959) corrected for the effect of shear and rotary inertia in the plate model and obtained results of wave propagation agreeing better with those using the exact theory. The modified expression for displacement field is written as

$$\begin{aligned} u_r &= z\psi_r(r, \theta, t) \\ u_\theta &= z\psi_\theta(r, \theta, t) \\ u_z &= w(r, \theta, t) \end{aligned} \quad (3.27)$$

where ψ_r and ψ_θ are the rotations of the normal to the mid-plane, measured on the $z - r$ and $z - \theta$ planes, respectively.

The substitution of Eqs. (3.2)-(3.6), (3.8) and (3.27) into Eq. (3.1) yields the following resultant moments and shear forces

$$\begin{aligned} M_{rr} &= (d_1 + d_2) \frac{\partial \psi_r}{\partial r} + (d_1 + d_2 - 2A_1) \left(\frac{\psi_r}{r} + \frac{\partial \psi_\theta}{r \partial \theta} \right) - \frac{4}{\pi} h_1 \bar{e}_{31} \varphi \\ M_{\theta\theta} &= (d_1 + d_2 - 2A_1) \frac{\partial \psi_r}{\partial r} + (d_1 + d_2) \left(\frac{\psi_r}{r} + \frac{\partial \psi_\theta}{r \partial \theta} \right) - \frac{4}{\pi} h_1 \bar{e}_{31} \varphi \\ M_{r\theta} &= A_1 \left(\frac{\partial \psi_r}{r \partial \theta} - \frac{\psi_\theta}{r} + \frac{\partial \psi_\theta}{\partial r} \right) \end{aligned} \quad (3.28)$$

$$\begin{aligned} Q_r &= A_3 \left(\frac{\partial w}{\partial r} + \psi_r \right) - \frac{4}{\pi} h_1 e_{15} \frac{\partial \varphi}{\partial r} \\ Q_\theta &= A_3 \left(\frac{\partial w}{r \partial \theta} + \psi_\theta \right) - \frac{4}{\pi} h_1 e_{15} \frac{\partial \varphi}{r \partial \theta} \end{aligned} \quad (3.29)$$

where $A_3 = \kappa^2(Yh/(1 + \mu) + 2h_1 C_{55}^E)$.

It is to be noted that M_{rr} , $M_{r\theta}$, $M_{\theta\theta}$, Q_r , and Q_θ must satisfy Maxwell equation (3.12) and the following dynamic equilibrium equations

$$\begin{aligned} \frac{\partial Q_r}{\partial r} + \frac{\partial Q_\theta}{r \partial \theta} + \frac{Q_r}{r} &= \int_{-h}^h \rho_1 \frac{\partial^2 u_z}{\partial t^2} dz + 2 \int_h^{h+h_1} \rho_2 \frac{\partial^2 u_z}{\partial t^2} dz \\ \frac{\partial M_{rr}}{\partial r} + \frac{\partial M_{r\theta}}{r \partial \theta} + \frac{M_{rr} - M_{r\theta}}{r} - Q_r &= \int_{-h}^h \rho_1 z \frac{\partial^2 u_r}{\partial t^2} dz + 2 \int_h^{h+h_1} \rho_2 z \frac{\partial^2 u_r}{\partial t^2} dz \\ \frac{\partial M_{r\theta}}{\partial r} + \frac{\partial M_{rr}}{r \partial \theta} + \frac{2M_{r\theta}}{r} - Q_\theta &= \int_{-h}^h \rho_1 z \frac{\partial^2 u_\theta}{\partial t^2} dz + 2 \int_h^{h+h_1} \rho_2 z \frac{\partial^2 u_\theta}{\partial t^2} dz \end{aligned} \quad (3.30)$$

The rotations ψ_r , and ψ_θ are expressed through the transformation (Mindlin, 1951)

$$\begin{aligned} \psi_r &= \frac{\partial R}{\partial r} + \frac{\partial H}{r \partial \theta} \\ \psi_\theta &= \frac{\partial R}{r \partial \theta} - \frac{\partial H}{\partial r} \end{aligned} \quad (3.31)$$

It is assumed that the solution of w , R , H and ϕ for wave propagation in the θ direction take the form

$$\begin{aligned} w(r, \theta, t) &= \bar{w}(r) \cos(p\theta) e^{i\omega t} \\ R(r, \theta, t) &= \bar{R}(r) \cos(p\theta) e^{i\omega t} \\ H(r, \theta, t) &= \bar{H}(r) \sin(p\theta) e^{i\omega t} \\ \varphi(r, \theta, t) &= \bar{\varphi}(r) \cos(p\theta) e^{i\omega t} \end{aligned} \quad (3.32)$$

Eq. (3.32) is adopted as it represents harmonic oscillation and is consistent with the assumption that the plate undergoes small synchronous free vibratory motions. To satisfy Eq. (3.30), the sine instead of cosine function is employed for $H(r, \theta, t)$.

Substituting Eq. (3.31) and (3.32) into Eq. (3.12) and (3.30) gives

$$A_3\Delta\bar{R} + A_3\Delta\bar{w} + A_2\omega^2\bar{w} - A_6\Delta\bar{\varphi} = 0 \quad (3.33a)$$

$$\frac{\partial}{\partial r}[(d_1 + d_2)\Delta\bar{R} - (A_3 - A_4\omega^2)\bar{R} - A_3\bar{w} + A_5\bar{\varphi}] + \frac{p}{r}[A_1\Delta\bar{H} - (A_3 - A_4\omega^2)\bar{H}] = 0 \quad (3.33b)$$

$$\frac{p}{r}[(d_1 + d_2)\Delta\bar{R} - (A_3 - A_4\omega^2)\bar{R} - A_3\bar{w} + A_5\bar{\varphi}] + \frac{\partial}{\partial r}[A_1\Delta\bar{H} - (A_3 - A_4\omega^2)\bar{H}] = 0 \quad (3.33c)$$

$$\Delta\bar{R} + A_7\Delta\bar{w} - A_8\Delta\bar{\varphi} - A_9\bar{\varphi} = 0 \quad (3.33d)$$

where

$$\Delta = \frac{\partial^2}{\partial r^2} + \frac{\partial}{r\partial r} - \frac{p^2}{r^2}, A_4 = \frac{2}{3}[(\rho_1 - \rho_2)h^3 + \rho_2(h + h_1)^3], A_5 = \frac{4h_1}{\pi}(e_{15} - \bar{e}_{31})$$

$$A_6 = \frac{4h_1e_{15}}{\pi}, A_7 = \frac{e_{15}}{e_{15} + \bar{e}_{31}}, A_8 = \frac{2\varepsilon_{11}}{(e_{15} + \bar{e}_{31})\pi}, A_9 = \frac{2\varepsilon_{11}\pi}{(e_{15} + \bar{e}_{31})h_1^2}$$

3.4.2 Solutions for w , ψ_r , ψ_θ and ϕ

\bar{H} may be separated from \bar{R} and \bar{w} by differentiation, addition, and subtraction of Eqs. (3.33b) and (3.33c). These two equations become

$$\Delta[A_1\Delta\bar{H} - (A_3 - A_4\omega^2)\bar{H}] = 0 \quad (3.34a)$$

$$\Delta[(d_1 + d_2)\Delta\bar{R} - (A_3 - A_4\omega^2)\bar{R} - A_3\bar{w} + A_5\bar{\varphi}] = 0 \quad (3.34b)$$

To uncouple \bar{R} , and $\bar{\varphi}$ and \bar{w} in Eqs. (3.33a) and (3.33d), and (3.34b), transformation of variables is applied, similar to that in (Ding *et al.*, 1996; Mindlin, 1951)

$$\bar{R} = x\bar{w} \quad (3.35)$$

$$\bar{\varphi} = y\bar{w}$$

where x , y are constants, Eqs. (3.33a), (3.33d), and (3.34b) can then be simplified to

$$\Delta[\Delta\bar{w} - \frac{A_3 - A_5y + (A_3 - A_4\omega^2)x}{(d_1 + d_2)x}\bar{w}] = 0 \quad (3.36a)$$

$$\Delta\bar{w} - \frac{A_2\omega^2}{A_6y - A_3(x + 1)}\bar{w} = 0 \quad (3.36b)$$

$$\Delta\bar{w} - \frac{A_9y}{A_8y - x - A_7}\bar{w} = 0 \quad (3.36c)$$

respectively. Observe that the terms within the brackets in Eqs. (3.36a), (3.36b) and (3.36c) are of identical form. Hence, for the solution of \bar{w} to be unique,

$$\frac{(A_3 - A_4\omega^2)x + A_3 - A_5y}{(d_1 + d_2)x} = \frac{A_2\omega^2}{A_6y - A_3(x + 1)} = \frac{A_9y}{A_8y - x - A_7} \quad (3.37a)$$

$$\frac{A_9y}{A_8y - x - A_7} = \lambda \quad (3.37b)$$

Eq. (3.36) can be thus reduced to

$$\Delta\bar{w} - \lambda\bar{w} = 0 \quad (3.38)$$

where λ is a constant. Eq. (3.37a) is cubic in x, y , giving rise to three roots, $x_i, y_i (i = 1, 2, 3)$, from which $\lambda_i (i = 1, 2, 3)$ can be computed using Eq. (3.37b). Three sets of Bessel functions $c_i w_{i1}(p, \delta_i r) + c_{i+3} w_{i2}(p, \delta_i r), i = 1, 2, 3$ where $\delta_i = \sqrt{|\lambda_i|}$ are obtained by substituting $\lambda_i (i = 1, 2, 3)$ into Eq. (3.38). The final solutions are given as

$$w = \sum_{i=1}^3 [c_i w_{i1}(p, \delta_i r) + c_{i+3} w_{i2}(p, \delta_i r)] \cos(p\theta) e^{i\omega t} \quad (3.39a)$$

$$R = \sum_{i=1}^3 x_i [c_i w_{i1}(p, \delta_i r) + c_{i+3} w_{i2}(p, \delta_i r)] \cos(p\theta) e^{i\omega t} \quad (3.39b)$$

$$\varphi = \sum_{i=1}^3 y_i [c_i w_{i1}(p, \delta_i r) + c_{i+3} w_{i2}(p, \delta_i r)] \cos(p\theta) e^{i\omega t} \quad (3.39c)$$

where the definition of $w_{i1}(p, \delta_i r)$ and $w_{i2}(p, \delta_i r)$ is the same as Eq. (3.20); and $c_i (i = 1, \dots, 6)$ are integration constants.

Substituting Eq. (3.36a) into Eqs. (3.33b) and (3.33c), gives the following Bessel equation

$$\Delta\bar{H} - \lambda_4\bar{H} = 0 \quad (3.40)$$

where

$$\lambda_4 = \frac{A_3 - A_4\omega^2}{A_1}$$

Finally, H can be expressed as

$$H = [c_7 w_{41}(p, \delta_4 r) + c_8 w_{42}(p, \delta_4 r)] \sin(p\theta) e^{i\omega t} \quad (3.41)$$

where $\delta_4 = \sqrt{|\lambda_4|}$ and the definition of $w_{41}(p, \delta_4 r)$ and $w_{42}(p, \delta_4 r)$ are the same as Eq. (3.20); and $c_i (i = 7, 8)$ are integration constants.

Substituting Eqs. (3.39b) and (3.41) into Eq. (3.31) gives

$$\begin{aligned}\psi_r &= \left[\sum_{i=1}^3 x_i \left(c_i \frac{\partial w_{i1}}{\partial r} + c_{i+3} \frac{\partial w_{i2}}{\partial r} \right) + \frac{p}{r} (c_7 w_{41} + c_8 w_{42}) \right] \cos(p\theta) e^{i\omega t} \\ \psi_\theta &= - \left[\frac{p}{r} \sum_{i=1}^3 x_i (c_i w_{i1} + c_{i+3} w_{i2}) + \left(c_7 \frac{\partial w_{41}}{\partial r} + c_8 \frac{\partial w_{42}}{\partial r} \right) \right] \sin(p\theta) e^{i\omega t}\end{aligned}\quad (3.42)$$

The determinant of the matrix of system frequencies is generated after imposing the electric and displacement boundary conditions. The electric boundary condition can be obtained by substituting Eq. (3.6a) into Eq. (3.21) giving

$$e_{15}\pi \left(\psi_r + \frac{\partial w}{\partial r} \right) - 2\varepsilon_{11} \frac{\partial \varphi}{\partial r} = 0 \quad (3.43)$$

The standard boundary conditions for the clamped, simply supported (soft type) and free ends are given respectively as follow:

(a) clamped:

$$\begin{aligned}w(r_1, \theta, t) = \psi_r(r_1, \theta, t) = \psi_\theta(r_1, \theta, t) &= \left[e_{15}\pi \left(\psi_r + \frac{\partial w}{\partial r} \right) - 2\varepsilon_{11} \frac{\partial \varphi}{\partial r} \right]_{r=r_1} = 0 \\ w(r_0, \theta, t) = \psi_r(r_0, \theta, t) = \psi_\theta(r_0, \theta, t) &= \left[e_{15}\pi \left(\psi_r + \frac{\partial w}{\partial r} \right) - 2\varepsilon_{11} \frac{\partial \varphi}{\partial r} \right]_{r=r_0} = 0\end{aligned}\quad (3.44)$$

(b) simply supported:

$$\begin{aligned}w(r_1, \theta, t) = M_{rr}(r_1, \theta, t) = M_{r\theta}(r_1, \theta, t) &= \left[e_{15}\pi \left(\psi_r + \frac{\partial w}{\partial r} \right) - 2\varepsilon_{11} \frac{\partial \varphi}{\partial r} \right]_{r=r_1} = 0 \\ w(r_0, \theta, t) = M_{rr}(r_0, \theta, t) = M_{r\theta}(r_0, \theta, t) &= \left[e_{15}\pi \left(\psi_r + \frac{\partial w}{\partial r} \right) - 2\varepsilon_{11} \frac{\partial \varphi}{\partial r} \right]_{r=r_0} = 0\end{aligned}\quad (3.45)$$

(c) free:

$$\begin{aligned}M_{rr}(r_1, \theta, t) = M_{r\theta}(r_1, \theta, t) = Q_r(r_1, \theta, t) &= \left[e_{15}\pi \left(\psi_r + \frac{\partial w}{\partial r} \right) - 2\varepsilon_{11} \frac{\partial \varphi}{\partial r} \right]_{r=r_1} = 0 \\ M_{rr}(r_0, \theta, t) = M_{r\theta}(r_0, \theta, t) = Q_r(r_0, \theta, t) &= \left[e_{15}\pi \left(\psi_r + \frac{\partial w}{\partial r} \right) - 2\varepsilon_{11} \frac{\partial \varphi}{\partial r} \right]_{r=r_0} = 0\end{aligned}\quad (3.46)$$

For all possible combinations of clamped, simply supported and free edge conditions at the inner ($r = r_1$) and outer ($r = r_0$) circular boundaries of the annular plate (Fig. 3.1), a

matrix of system frequencies can be formulated. For example, the determinant of system frequencies under clamped-clamped (C-C) boundary condition is given by substituting Eqs. (3.39a), (3.39c), and (3.42) into Eq. (3.44)

$$\begin{vmatrix} w_{11}(\delta_1 r_1) & w_{12}(\delta_1 r_1) & w_{21}(\delta_2 r_1) & w_{22}(\delta_2 r_1) & w_{31}(\delta_3 r_1) & w_{32}(\delta_3 r_1) & 0 & 0 \\ x_1 w'_{11}(\delta_1 r_1) & x_1 w'_{12}(\delta_1 r_1) & x_2 w'_{21}(\delta_2 r_1) & x_2 w'_{22}(\delta_2 r_1) & x_3 w'_{31}(\delta_3 r_1) & x_3 w'_{32}(\delta_3 r_1) & \frac{p}{r_1} w_{41}(\delta_4 r_1) & \frac{p}{r_1} w_{42}(\delta_4 r_1) \\ \frac{px_1}{r_1} w_{11}(\delta_1 r_1) & \frac{px_1}{r_1} w_{12}(\delta_1 r_1) & \frac{px_2}{r_1} w_{21}(\delta_2 r_1) & \frac{px_2}{r_1} w_{22}(\delta_2 r_1) & \frac{px_3}{r_1} w_{31}(\delta_3 r_1) & \frac{px_3}{r_1} w_{32}(\delta_3 r_1) & w'_{41}(\delta_4 r_1) & w'_{42}(\delta_4 r_1) \\ \varphi_{11}(r_1) & \varphi_{12}(r_1) & \varphi_{21}(r_1) & \varphi_{22}(r_1) & \varphi_{31}(r_1) & \varphi_{32}(r_1) & 0 & 0 \\ w_{11}(\delta_1 r_0) & w_{12}(\delta_1 r_0) & w_{21}(\delta_2 r_0) & w_{22}(\delta_2 r_0) & w_{31}(\delta_3 r_0) & w_{32}(\delta_3 r_0) & 0 & 0 \\ x_1 w'_{11}(\delta_1 r_0) & x_1 w'_{12}(\delta_1 r_0) & x_2 w'_{21}(\delta_2 r_0) & x_2 w'_{22}(\delta_2 r_0) & x_3 w'_{31}(\delta_3 r_0) & x_3 w'_{32}(\delta_3 r_0) & \frac{p}{r_0} w_{41}(\delta_4 r_0) & \frac{p}{r_0} w_{42}(\delta_4 r_0) \\ \frac{px_1}{r_0} w_{11}(\delta_1 r_0) & \frac{px_1}{r_0} w_{12}(\delta_1 r_0) & \frac{px_2}{r_0} w_{21}(\delta_2 r_0) & \frac{px_2}{r_0} w_{22}(\delta_2 r_0) & \frac{px_3}{r_0} w_{31}(\delta_3 r_0) & \frac{px_3}{r_0} w_{32}(\delta_3 r_0) & w'_{41}(\delta_4 r_0) & w'_{42}(\delta_4 r_0) \\ \varphi_{11}(r_0) & \varphi_{12}(r_0) & \varphi_{21}(r_0) & \varphi_{22}(r_0) & \varphi_{31}(r_0) & \varphi_{32}(r_0) & 0 & 0 \end{vmatrix} \quad (3.47)$$

where $w_{ij}(p, \delta_i r)$ is expressed as $w_{ij}(\delta_r)$ for concise notation, the factors $\cos(p\theta)e^{i\omega t}$ and $\sin(p\theta)e^{i\omega t}$ have been omitted; $()' = \partial/\partial r$, and

$$\varphi_{ij}(r_0) = e_{15}\pi x_i w_{ij}(p, \delta_i r_0) + (e_{15}\pi - 2\varepsilon_{11}y_i)w'_{ij}(p, \delta_i r_0)$$

$$\varphi_{ij}(r_1) = e_{15}\pi x_i w_{ij}(p, \delta_i r_1) + (e_{15}\pi - 2\varepsilon_{11}y_i)w'_{ij}(p, \delta_i r_1)$$

$$i = 1, 2, 3, j = 1, 2$$

Setting Eq. (3.47) to zero yields the resonant frequencies and their corresponding mode shapes.

3.5 Numerical examples and discussion

The numerical solution for a three-layer laminated annular plate shown in Fig. 3.1 is investigated. The material for the host is steel and that of the piezoelectric layer is PZT4. The material properties are listed in Table 3.1. The inner radius (r_1) and outer radius (r_0) of the annular plate are 0.1 m and 0.6 m respectively.

Table 3.1: Material properties

Property	Steel	PZT4		
Young's module (GPa)	200	$C_{11}^E = 132$	$C_{12}^E = 71$	$C_{13}^E = 73$
		$C_{33}^E = 115$	$C_{55}^E = 73$	-
Poisson ratio	0.3	-		
Mass density (kg/m^3)	7800	7500		
Piezoelectric constant (C/m^2)	-	$e_{31} = -4.1$	$e_{33} = 14.1$	$e_{15} = 10.5$
Permittivity (nF/m)	-	$\varepsilon_{11} = 7.124$	$\varepsilon_{33} = 5.841$	-

3.5.1 Comparisons between proposed models and FEM

To investigate the difference between CPT-based model and FSDT-based model, two steel plates with thickness, $h = 0.01$ m and 0.03 m, are studied under four kinds of boundary conditions: C-C, S-C, C-S and S-S, where the first and second letter denotes the edge condition at the inner and outer edge, respectively, C denotes clamped and S denotes simply supported. The thickness ratio of the piezoelectric layer to the host plate is $1/10$. The results are compared with those of 3D FE analyses using ABAQUS® 6.3.

Table 3.2 lists the frequencies for the free vibration of the annular plate with $h = 0.01$ m corresponding to thin plate, for mode shapes with 0 to 2 diametrical nodes (denoted by p) and 0 to 2 nodal circles (denoted by n). For a thin plate with large radius-thickness ratio ($r_0/h=60$), the frequencies from both CPT-based model and FSDT-based model are in close agreement with the FE results. The FSDT-based model produces (slightly lower) results almost coincident with those from FE analysis while the results from CPT-based model differ by less than 5% for all modes listed in Table 3.2.

Table 3.3 lists the frequencies for the free vibration of the annular plate with $h = 0.03$ m corresponding to moderately thick plate, for mode shapes with 0 to 2 diametrical nodes and 0 to 2 nodal circles. As the radius-to-thickness ratio is small ($r_0/h = 20$), the FSDT-based model provides results lower than those from FE analysis, with a maximum difference of only 3.4% for the case where $p = 2$, $n = 2$ under C-C boundary condition while the frequencies computed by CPT-based model can be 39.7% greater than those from FE analysis.

Both the CPT-based model and FSDT-based model give results closer to the FE analysis results at lower frequencies than they do at higher frequencies as shown in Table 3.2 and Table 3.3. For example, in Table 3.3, the CPT-based model gives a frequency 39.7% greater than that of the FE analysis for $p = 2$ and $n = 2$ while it gives a value of only 11.0% greater than that of the FE analysis for $p = 0$ and $n = 0$ under C-C

Table 3.2: Comparison of frequencies (rad/s) of thin annular plate under C-C, C-S, S-C, S-S boundary conditions for $r_0/h = 60$

BC	p	n	FEM	CPT-based model	Error (%)	FSDT-based model	Error (%)
C [†] -C	0	0	2812	2815	0.09%	2769	-1.53%
		1	7659	7786	1.66%	7517	-1.85%
		2	14753	15306	3.75%	14428	-2.20%
	1	0	2942	2952	0.36%	2899	-1.43%
		1	7882	8030	1.87%	7743	-1.76%
		2	15020	15608	3.91%	14698	-2.14%
	2	0	3471	3506	0.99%	3438	-0.97%
		1	8635	8840	2.38%	8507	-1.48%
		2	15877	16569	4.36%	15566	-1.96%
C-S	0	0	1848	1843	-0.31%	1823	-1.36%
		1	6164	6220	0.92%	6066	-1.59%
		2	12770	13111	2.67%	12523	-1.94%
	1	0	1981	1983	0.10%	1957	-1.21%
		1	6384	6459	1.16%	6289	-1.50%
		2	13038	13411	2.86%	12794	-1.87%
	2	0	2511	2535	0.95%	2495	-0.62%
		1	7134	7259	1.75%	7050	-1.17%
		2	13903	14367	3.34%	13672	-1.66%
S-C	0	0	2213	2216	0.12%	2194	-0.86%
		1	6544	6615	1.08%	6455	-1.37%
		2	13169	13531	2.75%	12934	-1.78%
	1	0	2418	2446	1.13%	2397	-0.89%
		1	6865	6983	1.72%	6774	-1.32%
		2	13528	13961	3.20%	13293	-1.74%
	2	0	3178	3236	1.81%	3159	-0.61%
		1	7902	8119	2.74%	7815	-1.11%
		2	14663	15274	4.16%	14428	-1.61%
S-S	0	0	1395	1396	0.04%	1388	-0.51%
		1	5173	5198	0.49%	5115	-1.11%
		2	11283	11489	1.82%	11114	-1.50%
	1	0	1593	1613	1.30%	1583	-0.58%
		1	5490	5558	1.23%	5433	-1.05%
		2	11647	11918	2.32%	11478	-1.45%
	2	0	2312	2355	1.84%	2306	-0.25%
		1	6521	6669	2.27%	6468	-0.82%
		2	12798	13225	3.34%	12632	-1.30%

p = number of nodal diameters.

n = number of nodal circles.

C = clamped, S = simply supported.

[†]The first letter denotes the condition at the inner edge.

Table 3.3: Comparison of frequencies (rad/s) of moderately thick annular plate under C-C, C-S, S-C, S-S boundary conditions for $r_0/h = 20$

BC	p	n	FEM	CPT-based model	Error (%)	FSDT-based model	Error (%)
C [†] -C	0	0	7608	8444	10.98%	7416	-2.52%
		1	18828	23358	24.06%	18235	-3.15%
		2	33096	45917	38.74%	31869	-3.71%
	1	0	7918	8857	11.86%	7728	-2.40%
		1	19358	24089	24.44%	18774	-3.02%
		2	33685	46824	39.00%	32468	-3.61%
	2	0	9336	10517	12.65%	9169	-1.79%
		1	21199	26520	25.10%	20639	-2.64%
		2	35591	49706	39.66%	34397	-3.35%
C-S	0	0	5171	5528	6.90%	5064	-2.07%
		1	15924	18661	17.19%	15500	-2.66%
		2	30188	39332	30.29%	29201	-3.27%
	1	0	5512	5950	7.95%	5406	-1.91%
		1	16464	19376	17.69%	16048	-2.52%
		2	30803	40232	30.61%	29827	-3.17%
	2	0	6990	7604	8.79%	6907	-1.17%
		1	18376	21776	18.50%	17986	-2.12%
		2	32806	43101	31.38%	31854	-2.90%
S-C	0	0	6218	6647	6.91%	6125	-1.49%
		1	16939	19845	17.16%	16536	-2.38%
		2	31161	40594	30.27%	30197	-3.09%
	1	0	6664	7337	10.10%	6555	-1.64%
		1	17593	20949	19.07%	17172	-2.39%
		2	31809	41883	31.67%	30826	-3.09%
	2	0	8650	9707	12.22%	8528	-1.41%
		1	19909	24357	22.34%	19453	-2.29%
		2	33990	45821	34.81%	32959	-3.03%
S-S	0	0	4032	4187	3.86%	3997	-0.85%
		1	14030	15593	11.14%	13775	-1.82%
		2	28159	34466	22.40%	27430	-2.59%
	1	0	4498	4840	7.60%	4450	-1.06%
		1	14716	16674	13.30%	14443	-1.86%
		2	28852	35753	23.92%	28102	-2.60%
	2	0	6484	7064	8.94%	6433	-0.79%
		1	17162	20008	16.58%	16859	-1.77%
		2	31183	39676	27.23%	30385	-2.56%

p = number of nodal diameters.

n = number of nodal circles.

C = clamped, S = simply supported.

[†]The first letter denotes the condition at the inner edge.

Table 3.4: Comparison of first three displacement mode shapes for annular plate ($h = 0.01$ for thin plate condition and 0.03 for moderately thick plate condition) under C-C and S-S conditions from FE and proposed solutions

$h(m)$	BC	Cases	$p=0, n=0$	$p=1, n=0$	$p=2, n=0$
0.01	C-C†	FE results			
		CPT			
	S-S	FE results			
		CPT			
0.03	C-C†	FE results			
		FSDT			
	S-S	FE results			
		FSDT			

p = number of nodal diameters. n = number of nodal circles.

C = clamped, S = simply supported.

† first letter denotes edge condition at inner edge.

boundary condition. Moreover S-S boundary conditions yield smaller frequencies than those under C-C, C-S and S-C boundary conditions and hence their results are closer to the FE results. The CPT-based model gives higher frequencies than FSDT-based model because the CPT-based model neglects the effect of transverse shear deformation and rotary inertia which implies a stiffer model. Table 3.4 shows the first three mode shapes of the annular plate of thickness $h = 0.01$ m (simulating a thin plate) and 0.03 m (simulating a moderately thick plate) obtained by the proposed models and 3D FE results. The mode shape for the number of nodal diameters $p = 0, 1, 2$ and number of nodal circles $n = 0$ from the proposed models and 3D FE are almost identical.

3.5.2 Effect of piezoelectric layer

To investigate the effect of piezoelectric layer on the vibration of piezoelectric coupled plate, the two plates in Section 5.1 are studied based on the proposed models and FE analysis under C-C boundary condition. Three different thickness ratios of piezoelectric layer to host plate, $h_1/2h = 1/12, 1/8,$ and $1/5,$ are adopted.

Table 3.5 lists the frequencies for free vibration modes with $p = 0$ to 2 diametrical nodes and $n = 0$ to 2 nodal circles, where the case of $h_1 = 0$ provides the base for comparing the effect of the piezoelectric layer on the frequencies (and stiffness) of the system. For CPT-based model with $r_0/h = 60$ (thin plate), the percentage increase is around 2.7% for all modes with $h_1/2h = 1/12$. The effect is higher for thicker piezoelectric layer where with $h_1/2h = 1/8,$ and $1/5,$ the increase is about 4.9% and 10.0%, respectively, for all modes. This is mainly due to the increase in bending stiffness rather than the piezoelectric effect, as confirmed by results shown in Fig. 3.2, where the frequency ratio based on FEM simulation under C-C conditions is plotted (full line shows the effect of stiffness due to increase in thickness from piezoelectric layer whereas dotted line shows the effect of piezoelectricity only for this particular PZT4). Similar findings are obtained for $r_0/h = 20$. For FSDT-based model when $r_0/h = 60$, first, the frequencies are lower

Table 3.5: Frequencies (rad/s) of annular plate under C-C boundary condition with piezoelectric layers of different thickness

p	n	CPT-based model ($r_0/h = 60$)						
		$h_1=0$	$h_1/2h=1/12$	Increments	$h_1/2h=1/8$	Increments	$h_1/2h=1/5$	Increments
0	0	2718	2792	2.70%	2853	4.93%	2989	9.95%
	1	7520	7723	2.70%	7891	4.93%	8268	9.95%
	2	14783	15182	2.70%	15512	4.93%	16253	9.95%
1	0	2851	2928	2.70%	2992	4.93%	3135	9.95%
	1	7755	7965	2.70%	8138	4.93%	8527	9.95%
	2	15075	15482	2.70%	15818	4.93%	16574	9.95%
2	0	3385	3477	2.70%	3553	4.93%	3723	9.95%
	1	8538	8768	2.70%	8959	4.93%	9387	9.95%
	2	16002	16434	2.70%	16791	4.93%	17594	9.95%
p	n	CPT-based model ($r_0/h = 20$)						
0	0	8155	8376	2.71%	8558	4.93%	8967	9.95%
	1	22560	23169	2.70%	23672	4.93%	24804	9.95%
	2	44348	45545	2.70%	46534	4.93%	48760	9.95%
1	0	8554	8785	2.70%	8976	4.93%	9405	9.95%
	1	23266	23894	2.70%	24413	4.93%	25580	9.95%
	2	45224	46445	2.70%	47453	4.93%	49722	9.95%
2	0	10157	10432	2.71%	10659	4.93%	11168	9.95%
	1	25613	26305	2.70%	26877	4.93%	28162	9.95%
	2	48007	49303	2.70%	50374	4.93%	52783	9.95%
p	n	FSDT-based model ($r_0/h = 60$)						
0	0	2681	2748	2.49%	2804	4.57%	2930	9.25%
	1	7302	7465	2.24%	7604	4.14%	7918	8.44%
	2	14069	14339	1.92%	14577	3.61%	15116	7.45%
1	0	2808	2878	2.47%	2936	4.53%	3066	9.19%
	1	7523	7690	2.22%	7833	4.12%	8154	8.39%
	2	14334	14608	1.91%	14849	3.60%	15396	7.41%
2	0	3331	3412	2.45%	3481	4.50%	3635	9.13%
	1	8267	8449	2.20%	8604	4.07%	8955	8.32%
	2	15186	15472	1.88%	15725	3.55%	16299	7.34%
p	n	FSDT-based model ($r_0/h = 20$)						
0	0	7297	7384	1.19%	7471	2.37%	7670	5.10%
	1	18204	18209	0.03%	18287	0.46%	18512	1.69%
	2	32172	31892	-0.87%	31855	-0.99%	31924	-0.77%
1	0	7607	7695	1.15%	7783	2.31%	7989	5.02%
	1	18738	18746	0.04%	18829	0.48%	19069	1.76%
	2	32771	32490	-0.86%	32457	-0.96%	32537	-0.72%
2	0	9025	9130	1.16%	9237	2.34%	9486	5.11%
	1	20594	20607	0.06%	20703	0.53%	20982	1.88%
	2	34711	34418	-0.84%	34389	-0.93%	34492	-0.63%

p = number of nodal diameters.

n = number of nodal circles.

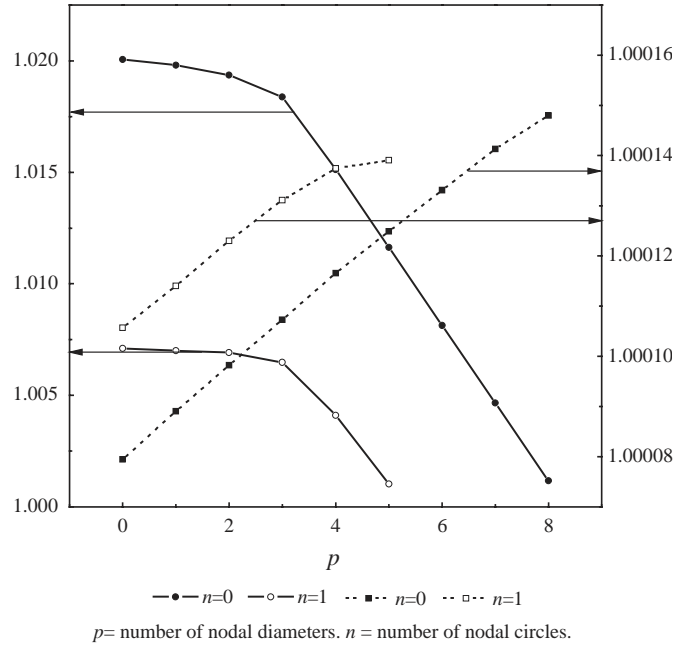


Figure 3.2: Frequency ratio based on FEM simulation under C-C conditions (Full line [left axis] - piezoelectric coupled plate with $r_0/h = 60$ and $h_1/2h = 1/10$ not accounting for piezoelectric effect over plate with piezoelectric layer removed ($h_1 = 0$); dotted line [right axis] - piezoelectric coupled plate accounting for piezoelectric effect over same plate without piezoelectric effect)

than the corresponding CPT-based values even with the presence of piezoelectric layers. Second, the increase in frequency for the FSDT-based for $h_1/2h = 1/12$, $1/8$, and $1/5$ are 2.5%, 4.6% and 9.3% respectively when $p = 0$ and $n = 0$. Both can be attributed by the FSDT-model being less stiff. The increase in resonant frequency is smaller for higher modes indicating reduced bending stiffness effect as confirmed by Fig. 3.2. For example, when $r_0/h = 60$ and $h_1/2h = 1/12$, the increase is 2.5% for $p = 0$ and $n = 0$, and 1.9% for $p = 2$ and $n = 2$. The increase in resonant frequency is also smaller for lower r_0/h values, for example when $r_0/h = 20$ and $h_1/2h = 1/12$, the increase is 1.2% (compared to 2.5% for $r_0/h = 60$ and $h_1/2h = 1/12$) for $p = 0$ and $n = 0$. This effect is not obvious for the CPT-based results as it does not account for the shear effect.

3.6 Conclusions

The free vibration of a three-layer piezoelectric laminated annular plate based on the Kirchhoff and Mindlin plate theories are investigated for the case where the electrodes on the piezoelectric layers are shortly connected. The electric potential distribution across the thickness of the piezoelectric layer is modeled by a sinusoidal function and Maxwell equation is enforced. Analytical solutions based on transformation of variables are presented. Numerical validation of the solutions against 3D FE results was performed for annular plates with different radius-to-thickness ratio under different boundary conditions. The FSDT-based model provides results similar to those from FE analysis for both thin and thick plates. The solutions based on CPT-based model are shown to be valid only for thin plates and diverge from the FE results for thick plates, particularly for high frequencies. Results indicate that thicker piezoelectric layer increases the resonant frequencies of the system but the effect is less significant for higher modes and also plates with lower radius to thickness ratio. The analytical solutions and the findings provided will be used in the design of piezoelectric materials in mechanical systems for practical applications, such as the ultrasonic motor.

CHAPTER 4

Finite Element Solution for Intermittent-Contact Problem in Ring Type USM

The objective of the proposed research is to initiate the framework for a model and the realization of USMs with multiple wave numbers. For efficient conceptual and preliminary design purpose, analytical models of USMs are necessary as they have the advantage of simplicity, allows understanding of the mechanics and performing extensive parametric study. In Chapter 2 closed form solutions for the free vibration problem of annular plates with thickness varying in a power form of arbitrary constants were derived. Such closed form solutions are useful for engineers working on USMs and plated structures. Chapter 3 treats the free vibration problem of a three-layer piezoelectric laminated annular plate. The effects of transverse shear deformation and rotary inertia are taken into consideration by adopting the Mindlin plate theory. Again analytical solutions are obtained which should be useful for the design of USM. However, for a detailed analysis taking into account the complex geometry and piezoelectric-structure interaction of an actual USM, analytical solution becomes cumbersome, if not impossible. As presented in Chapter 1, FE analysis can account for potential complex geometry in the stator and the full piezoelectric coupling effect to facilitate better understanding of the characteristics of an USM.

In this chapter, a complete 3-D FE framework is established, which combines the piezoelectric coupled stator dynamics and intermittent-contact mechanics to simulate the steady state and transient behavior of USM, capable of producing fairly accurate results at moderate computational cost. After a brief description of the USM addressed in Section 4.1, the differential governing equations for the intermittent-contact problem with piezoelectric actuation and their spatial and temporal discretization are introduced in Section 4.2. Difficulties in terms of the incompatibility arising from the mass-less characteristics of electric variables with explicit time integration routine and the incompatibility of intermittent-contact behaviour with implicit time integration routine are addressed. The first difficulty is overcome by the proposed equivalent piezoelectric force (EPF) procedure using explicit time integration in Section 4.3. The second difficulty leads to the proposed steady contact (SC) procedure using implicit time integration. To test the performance of the proposed procedures, numerical simulation of the overall behavior of Kagawa *et al.* (1996) and Glenn (2002) USMs are carried out in Section 4.4. The results are compared with theoretical, numerical and experimental data from published literature.

4.1 Description of USM

Only a brief description of the USM is given here as a detailed description on the configurations and working principle can be found in the literature (Sashida and Kenjo, 1993; Uchino, 1997; Ueha and Tomikawa, 1993; Wallaschek, 1995). One USM configuration based on a contact system comprising a rotor and a stator is shown in Fig. 4.1. A piezoceramic ring (or a number of piezoceramic patches arranged in a ring shape) is bonded to the underside of an elastic ring in the stator to induce a traveling wave. A set of teeth separated in segments is bonded on top of the elastic ring. The geometry, material and position of the teeth in the stator are determined based on the trade-off amongst torque, speed and efficiency. The rotor is aligned on top of the stator with a small gap between

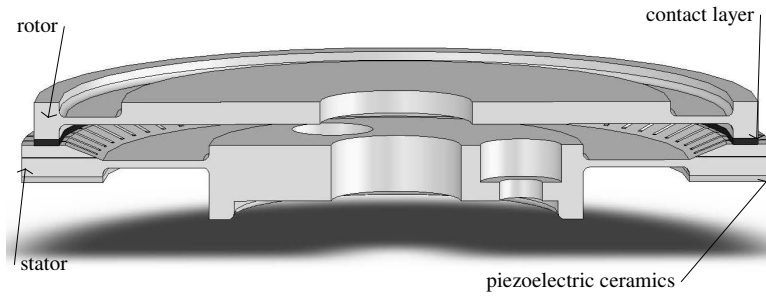


Figure 4.1: Geometry of generic USM

them. A layer of contact material is bonded to bottom of the rotor as shown in Fig. 4.1. The rotor contacts with the stator top surface at areas corresponding to the crests of the traveling wave resulting in a vertical compressive force and a horizontal frictional force at their interface. This generates a steady state rotary action on the rotor. The operation of USM can be simulated as an intermittent-contact problem with piezoelectric actuation. Solution via FE analysis will involve special difficulties in view of the mass-less electrical variables and the contact being a highly discontinuous, nonlinear problem. Before presenting the solution technique, the governing equations and prescribed boundary conditions are first presented.

4.2 Overall behavior analysis of USM by finite element method

The basic equations governing the overall behavior of USM in obtaining the FE solution are first presented. An essential step in FE analysis is the spatial and temporal discretization, which is formulated herein using the principle of virtual work. The advantages and disadvantages of conventional explicit and implicit routine are discussed.

4.2.1 Governing equations

The overall behavior of USM system from time $t = [0, T]$ will be studied assuming that the stator and rotor undergo small displacement and small strain. Assuming that they occupy the domain $\bar{\Omega}$ in a fixed global Cartesian coordinate system (x_1, x_2, x_3) , then

$\bar{\Omega} = \bar{\Omega}^I \cup \bar{\Omega}^J$, where $\bar{\Omega}^I$ denotes the stator domain and $\bar{\Omega}^J$ that of the rotor. Denoting the boundaries and interior volumes of $\bar{\Omega}$ as S and Ω respectively, then $\bar{\Omega} = \Omega \cup S$.

The entire intermittent-contact system are governed by five main groups of equations, namely, those of equilibrium, constitutive, compatibility, boundary and initial conditions (ABAQUS, 2003; Kim *et al.*, 1997; Landis, 2002; Zhong, 1993). In the following equations, all the indices range over 1, 2, and 3 to represent the three orthogonal directions.

The mechanical dynamic and electrostatic equilibrium equations (Trindade *et al.*, 2001a,b; Vasques and Rodrigues, 2005; Yi *et al.*, 1999) are as follows:

$$\sigma_{ij,j} + f_i^B = \rho \ddot{u}_i \quad (4.1)$$

$$D_{i,i} - q = 0 \quad (4.2)$$

where, f_i^B , q , ρ and u_i are the mechanical body force components, electric body charge, mass density and mechanical displacements, respectively; and σ_{ij} and D_i are the stress tensor and electric displacement vector components. They are related to strain tensor ϵ_{ij} and electric field vector E_i through the converse and direct linear piezoelectric constitutive equations,

$$\sigma_{ij} = C_{ijkl}\epsilon_{kl} - e_{mij}E_m \quad (4.3)$$

$$D_i = e_{ikl}\epsilon_{kl} + \varepsilon_{im}E_m \quad (4.4)$$

C_{ijkl} , e_{mij} and ε_{im} denote elastic, piezoelectric and dielectric material constants. The strain tensor and electric field vector components are linked to mechanical displacement components u_i and electric field potential ϕ by the following relations,

$$\epsilon_{ij} = \frac{1}{2}(u_{i,j} + u_{j,i}) \quad (4.5)$$

$$E_i = -\phi_{,i} \quad (4.6)$$

The boundary conditions are given by:

(a) natural mechanical boundary condition on S_f :

$$\sigma_{ij}n_j = f_i^S \quad (4.7)$$

(b) natural electrical boundary condition on S_q :

$$n_i D_i = q^S \quad (4.8)$$

(c) essential mechanical boundary condition on S_u :

$$u_i = U_i \quad (4.9)$$

(d) essential electrical boundary condition on S :

$$\phi = \Phi \quad (4.10)$$

where f_i^S is the surface force, q^S is the surface charge, and Φ is the electrical potential.

The remaining contact boundary conditions (Bathe, 1996; Eterovic and Bathe, 1991; Hughes *et al.*, 1976; Wriggers, 2002) on S_c are non-trivial. Assume that the body I (stator) and the body J (rotor) are supported such that without contact between them, no rigid body motion is possible. Let surfaces S^{IJ} and S^{JI} be a "contact surface pair", and $S_c = S^{IJ} \cup S^{JI}$. It is convenient to call S^{IJ} the "contact surface" and S^{JI} the "target surface". Let \mathbf{f}^{IJ} be the vector of contact surface tractions on body I due to contact with body J , then $\mathbf{f}^{IJ} = -\mathbf{f}^{JI}$. Let \mathbf{n} be the unit outward normal to S^{JI} and let \mathbf{s}_1 and \mathbf{s}_2 be vectors such that \mathbf{n} , \mathbf{s}_1 and \mathbf{s}_2 form a set of right-hand bases. The contact tractions \mathbf{f}^{IJ} acting on S^{IJ} can be decomposed into normal (denoted as λ) and tangential (denoted as t_1 and t_2) components relative to S^{JI} as

$$\mathbf{f}^{IJ} = \lambda \mathbf{n} + \mathbf{t} \quad (4.11)$$

$$\mathbf{t} = t_1 \mathbf{s}_1 + t_2 \mathbf{s}_2 \quad (4.12)$$

where

$$\begin{aligned}\lambda &= \mathbf{f}^{IJ} \cdot \mathbf{n} \\ t_1 &= \mathbf{f}^{IJ} \cdot \mathbf{s}_1 \\ t_2 &= \mathbf{f}^{IJ} \cdot \mathbf{s}_2\end{aligned}\tag{4.13}$$

Consider a generic point \mathbf{x} on S^{IJ} and let $\mathbf{y}^*(x, t)$ be the point on S^{JI} satisfying

$$\|\mathbf{x} - \mathbf{y}^*\|_2 = \min_{\mathbf{y} \in S^{JI}} \{\|\mathbf{x} - \mathbf{y}\|_2\}\tag{4.14}$$

The gap function for the contact surface pair (distance from \mathbf{x} to S^{JI}) is then given by

$$g(\mathbf{x}, t) = (\mathbf{x} - \mathbf{y}^*) \cdot \mathbf{n}(\mathbf{y}^*)\tag{4.15}$$

Using such definition, the conditions for normal contact can be stated as

$$g \geq 0; \lambda \geq 0; g\lambda = 0\tag{4.16}$$

where the last equation expresses the fact that if $g > 0$, then $\lambda = 0$, and vice versa.

To include friction conditions, Coulomb's law of friction is assumed to hold point-wise on the contact surface. If μ is the coefficient of friction, the non-dimensional variable τ is defined by

$$\tau = \frac{\|\mathbf{t}\|}{\mu\lambda}\tag{4.17}$$

The magnitude of the relative tangential velocity is

$$\dot{u}(\mathbf{x}, t) = (\dot{\mathbf{u}}^J(\mathbf{y}^*, t) - \dot{\mathbf{u}}^I(\mathbf{x}, t)) \cdot \frac{\mathbf{t}(\mathbf{y}^*, t)}{\|\mathbf{t}\|}\tag{4.18}$$

Hence, $\dot{u}(x, t)$ is the tangential velocity at time t of the material point at $\mathbf{y}^*(\mathbf{x}, t)$ relative to the material point at x . With these definitions Coulomb's law of friction states

$$|\tau| \leq 1\tag{4.19}$$

and $|\tau| < 1$ (stick state) implies $\dot{u} = 0$ (λ , t_1 and t_2 are independent variables), while $|\tau| = 1$ (slip state) implies $sign(\dot{u}) = sign(\tau)$ (λ are related to t_1 and t_2 by the friction coefficient μ).

For the boundary surface S , one can write [$S_u \cup S_f = S$ and $S_u \cap S_f = 0$] and [$S_q \cup S_\phi = S$ and $S_q \cap S_\phi = 0$].

The initial conditions here are set to be

$$\left. \begin{array}{l} u_i(x, 0) = 0 \\ \dot{u}_i(x, 0) = 0 \end{array} \right\} \text{ on } \Omega \quad (4.20)$$

4.2.2 Variational formulation

To formulate the intermittent-contact problem with piezoelectric patch actuation, the principle of virtual work is adopted. The virtual work done by a stress field σ_{ij} on a virtual strain field $\delta\epsilon_{ij}$ is

$$\delta W_S = \int_{\Omega} \sigma_{ij,j} \delta\epsilon_{ij} d\Omega \quad (4.21)$$

The virtual work done by the mechanical loads, the contact loads, the inertial forces through the virtual displacement field δu are denoted by δW_R , δW_C and δW_I respectively and are calculated as

$$\delta W_R = \int_{\Omega} f_i^B \delta u_i d\Omega + \int_{S_f} f_i^S \delta u_i dS \quad (4.22)$$

$$\delta W_C = \int_{S^{IJ}} f_i^{IJ} \delta u_{ci}^I dS + \int_{S^{JI}} f_i^{JI} \delta u_{ci}^J dS \quad (4.23)$$

$$\delta W_I = - \int_{\Omega} \rho \ddot{u}_i \delta u_i d\Omega \quad (4.24)$$

where δu_{ci}^I and δu_{ci}^J are the components of the virtual displacements on the contact surfaces of bodies I and J respectively.

According the principle of virtual work and letting $\delta u_{ci}^{IJ} = \delta u_{ci}^I - \delta u_{ci}^J$,

$$\int_{\Omega} \sigma_{ij,j} \delta\epsilon_{ij} d\Omega = \int_{\Omega} f_i^B d\Omega + \int_{S_f} f_i^S dS - \int_{\Omega} \rho \ddot{u}_i \delta u_i d\Omega + \int_{S^{IJ}} f_i^{IJ} \delta u_{ci}^{IJ} dS \quad (4.25)$$

Analogous to the principle of virtual work, the principle of virtual electric potentials can be stated as follows

$$\int_{\Omega} D_i \delta E_i d\Omega = - \int_{S_q} q_i \delta \phi dS \quad (4.26)$$

In variational principles, no restrictions on constitutive relations are imposed up to this stage. Substituting the linear constitutive relationships of Eqs. (4.3) and (4.4) into Eqs. (4.25) and (4.26), the following set of equations are obtained

$$\int_{\Omega} c_{ijkl}\epsilon_{kl}\delta\epsilon_{ij}d\Omega - \int_{\Omega} e_{mij}E_m\delta\epsilon_{ij}d\Omega = \int_{\Omega} f_i^B d\Omega + \int_{S_f} f_i^S dS - \int_{\Omega} \rho\ddot{u}_i\delta u_i d\Omega + \int_{S^{IJ}} f_i^{IJ}\delta u_{ci}^{IJ} dS \quad (4.27)$$

$$\int_{\Omega} e_{ikl}\epsilon_{kl}\delta E_i d\Omega + \int_{\Omega} d_{ij}E_j\delta E_i d\Omega = - \int_{S_q} q_i\delta\phi^S dS \quad (4.28)$$

From Eq. (4.27), one can see that the contact force effect is included as a contribution in the externally unknown applied tractions. To solve for this force, contact boundary conditions will be imposed.

Let w be a function of g and λ such that the solutions of $w(g, \lambda) = 0$ satisfy the conditions of (4.16). Similarly, let v be a function of τ and \dot{u} such that the solutions of $v(\tau, \dot{u}) = 0$ satisfy the conditions of (4.19). Then the contact conditions are given by

$$w(g, \lambda) = 0 \quad (4.29)$$

and

$$v(\tau, \dot{u}) = 0 \quad (4.30)$$

Two widely used procedures are available, namely, Lagrange multiplier method and penalty function method, to impose the contact constraints. Here, Lagrange multiplier method is adopted as it is exact. The variables λ , t_1 , t_2 can be considered as Lagrange multipliers and so the constraint equation can be written as

$$\int_{S^{IJ}} [\delta\lambda w(g, \lambda) + \delta t_1 v(\tau, \dot{u}) + \delta t_2 v(\tau, \dot{u})] dS^{IJ} = 0 \quad (4.31)$$

In summary, the governing equations to be solved for intermittent-contact problem with piezoelectric patch actuation are the usual principle of virtual work equations of (4.27) and (4.28), with the effect of the contact tractions included through externally applied (but unknown) forces, and the constraint equation given in Eq. (4.31).

4.2.3 Spatial and temporal discretization for nonlinear dynamics

In FE analysis, the displacements and electrical potentials are approximated within the element and expressed in terms of their nodal values as (ABAQUS, 2003; Zienkiewicz and Taylor, 2000)

$$\mathbf{u} = \mathbf{N}^N u^N \quad (4.32)$$

and

$$\phi = \mathbf{N}^N \phi^N \quad (4.33)$$

where \mathbf{N}^N is the array of interpolating functions, u^N and ϕ^N are nodal quantities, and N is the number of nodes in each element. The body forces and charges as well as the surface normal force, contact traction and charges are interpolated in a similar manner.

The strains and electrical potential gradients are given as

$$\epsilon = \mathbf{B}_u^N u^N \quad (4.34)$$

$$\mathbf{E} = -\mathbf{B}_\phi^N \phi^N \quad (4.35)$$

where \mathbf{B}_u^N and \mathbf{B}_ϕ^N are the spatial derivatives of \mathbf{N}^N .

With these approximate fields and the constitutive properties given in Eqs. (4.3) and (4.4), in conjunction with the equilibrium, conservation and contact constraint equations, the following system of equations is derived in terms of nodal quantities:

$$\begin{bmatrix} M & 0 & 0 \\ 0 & 0 & 0 \\ 0 & 0 & 0 \end{bmatrix} \begin{bmatrix} \ddot{U} \\ \ddot{\phi} \\ \ddot{F}_c \end{bmatrix} + \begin{bmatrix} C & 0 & 0 \\ 0 & 0 & 0 \\ 0 & 0 & 0 \end{bmatrix} \begin{bmatrix} \dot{U} \\ \dot{\phi} \\ \dot{F}_c \end{bmatrix} + \begin{bmatrix} K_{uu} & K_{\phi u} & R_2 \\ K_{\phi u} & K_{\phi\phi} & 0 \\ R_1 & 0 & 0 \end{bmatrix} \begin{bmatrix} U \\ \phi \\ F_c \end{bmatrix} = \begin{bmatrix} F \\ Q \\ P \end{bmatrix} \quad (4.36)$$

where

$$M = \rho \int_{\Omega} (\mathbf{N}^N)^T \cdot \mathbf{N}^N d\Omega \quad (4.37)$$

is the mass matrix (note that no inertia terms exist for the electrical flux conservation equation), ρ is the mass density and K_{uu} is the displacement stiffness matrix given by

$$K_{uu} = \int_{\Omega} (\mathbf{B}_u^N)^T \cdot [C] \cdot \mathbf{B}_u^N d\Omega \quad (4.38)$$

The dielectric "stiffness" matrix is given by

$$K_{\phi\phi} = \int_{\Omega} (\mathbf{B}_{\phi}^N)^T \cdot [\varepsilon] \cdot \mathbf{B}_{\phi}^N d\Omega \quad (4.39)$$

and the piezoelectric coupling matrix is

$$K_{u\phi} = (K_{\phi u})^T = \int_{\Omega} (\mathbf{B}_u^N)^T \cdot [e] \cdot \mathbf{B}_{\phi}^N d\Omega \quad (4.40)$$

For simplicity, the Rayleigh damping matrix is often expressed as

$$C = \alpha M + \beta K_{uu} \quad (4.41)$$

where α and β are constants to be determined from two target damping ratios corresponding to two selected modes of vibration. The mechanical force vector and the electrical charge vector are given respectively by

$$F = \int_{\Omega} \mathbf{N}^N \cdot f^B d\Omega + \int_S \mathbf{N}^N \cdot f^S dS \quad (4.42)$$

$$Q = \int_S \mathbf{N}^N \cdot q^S dS \quad (4.43)$$

F_c is the Lagrange multiplier vector, which in this application is the unknown normal contact and tangential frictional forces, R_1 and R_2 are contributions due to normal contacts and tangential frictional effects which vary with different contact cases and their details can be found in references (Ayari and Saouma, 1991; Bathe and Chaudhary, 1985; Matthies and Strang, 1979). If contact occurs without friction, then $R_1 = R_2$, and thus the stiffness matrix in Eq. (4.36) is symmetric. Otherwise, $R_1 \neq R_2$, and the matrix is non-symmetric, which is a well-known feature of contact friction problems. P is the initial penetration force between stator and rotor. It should be noted that in the penalty function method, F_c is set to be the multiplication of an artificially assumed stiffness and contact displacement, and the third row in Eq. (4.36) can be removed.

Eq. (4.36) can be solved using numerical time integration method, which can be either implicit or explicit. Explicit routines, such as the conditionally stable central difference method, obtain values for dynamic quantities at $t + \Delta t$ based entirely on

available values at time t . The stability limit is approximately proportional to the smallest period, say T_c , of the discretized system. The mass-less property of ϕ implies that the fundamental period is zero leading to instability of the method.

Implicit routines, such as Newmark's method, relax this upper bound on time step size by solving iteratively for dynamic quantities at time $t + \Delta t$ based on values of the previous iteration at t and $t + \Delta t$. However, for problems with highly discontinuous nonlinearities, convergence may not be reached or can only be reached under an impractically small time step, say $10^{-12}T_c$. For the case of USM, intermittent contact and stick/slip frictional sliding will result in the tangent coefficient matrix being not sufficiently smooth or the predicted intermediate state being too far from the actual solution, giving rise to convergence problem.

It therefore appears that solution to Eq. (4.36) may be achieved by the two different time integration routines for different segments of the USM. Specifically, the explicit time integration using the conditionally stable central difference method is employed to obtain the contact response and the implicit unconditionally stable time integration method (such as Newmark's method) is used to solve for the piezoelectric patch dynamics. However, such hybrid method raised other problems, such as the choice of finite difference methods and the coupling of the methods (Bathe, 1996; Bathe and Sonnad, 1980; Belytschko *et al.*, 1979).

4.3 Proposed procedures for overall behavior analysis of USM

It is proposed to use an equivalent piezoelectric force (EPF) procedure to avoid the incompatibility between mass-less characteristic of electric potential and explicit solution techniques to solve for the transient response of the USM. In the case of steady-state response of the USM, a more efficient steady-state contact (SC) procedure to overcome

the incompatibility in the implicit time integration routine resulting from intermittent contact is proposed.

4.3.1 Equivalent piezoelectric force (EPF) routine

In the EPF routine, thermal analogy (Cote *et al.*, 2004; Gaudenzi and Bathe, 1995) is employed to simulate the converse piezoelectric effects and the direct piezoelectric effect is ignored for piezo-actuation. Substituting Eq. (4.6) into the constitutive relation in Eq. (4.3) and considering $e_{mij} = C_{ijkl}d_{mkl}$ gives (Wang, 2004)

$$\sigma_{ij} = C_{ijkl}(\epsilon_{kl} + d_{mij}\phi_{,m}) \quad (4.44)$$

where d_{mkl} is piezoelectric constant. The generalized Hooke's law taking into account the thermal effect can be written as (Hanagud *et al.*, 1992)

$$\sigma_{ij} = C_{ijkl}(\epsilon_{kl} - \alpha\theta^0) \quad (4.45)$$

where α is thermal expansion coefficient matrix, and θ^0 is temperature difference, relative to a reference temperature, say 0°C.

Comparing Eqs. (4.44) and (4.45), the piezoelectric strain enters into the elasticity equations in the same manner as thermal strain. Making them analogous lead to

$$\alpha = d_{mij} \quad (4.46)$$

$$\theta^0 = -\phi_{,m} \quad (4.47)$$

Utilizing thermal analogy and penalty function, Eq. (4.36) can be simplified as

$$M\ddot{U} + C\dot{U} + (K_{uu} + K_{\alpha})U = F \quad (4.48)$$

where vector F contains the equivalent piezoelectric force from thermal analogy, and K_{α} is the assumed penalty stiffness. An explicit routine, such as the central difference, can be adopted to solve Eq. (4.48). This proposed procedure allows the transient responses of overall behavior of USM with piezoelectric actuation to be solved as a coupled dynamic stator-rotor-contact system.

4.3.2 Steady-state contact (SC) procedure

If the transient response of intermittent-contact is ignored, the overall analysis of USM can be performed by a steady-state contact procedure using the following proposed iterative routine:

- (a) Eigenvalues of piezoelectric coupled stator is first extracted;
- (b) For USM, the operating frequency is known. The piezoelectric coupled dynamics analysis of the stator is then performed using an implicit routine from which the steady- state displacement and velocity field of the stator are obtained;
- (c) From the stator response in step (b) and a prescribed velocity of the rotor, the steady- state contact force and deformation between the deformed stator and rotor is computed. From this, the torque can be estimated;
- (d) If the stator contact displacement is larger than the criterion set based on accuracy requirement, step (b) will be iterated by imposing the contact force obtained from step (c) until the contact displacement of stator becomes acceptable.

In this iterative procedure, the implicit dynamic time integration and steady-state contact are combined to perform the analysis of steady state operation of USM. No assumption of the stator bending profile is needed. The converse and direct piezoelectric effect can be accurately simulated using 3D piezoelectric element in the implicit routine. Steady-state contact allows the use of Lagrange multipliers for imposing the contact constraints in the normal and tangential directions exactly. Interaction between stator and contact interface is achieved through the iterative procedure between the dynamics and steady-state contact solution, minimizing computational cost. This procedure however does not give the transient response of USM due to startup or load variation.

4.4 Numerical demonstration and discussion

To demonstrate the capability of the proposed procedures in performing an overall analysis, the numerical results obtained are compared with published numerical and experimental results. The simulation will be performed on two motors, namely that of Kagawa *et al.* (1996) and Glenn (2002). The FEM models adopted for both motors are first detailed in Section 4.4.1. Section 4.4.2 provides a discussion on the results of Kagawa motor and comparison with theoretical results based on a simplified model. Free vibration, stator dynamics and the overall behavior of the motor are addressed. Section 4.4.3 describes the results of Glenn motor and evaluates the accuracy of the proposed routines against experimental results. All computations are performed using ABAQUS® version 6.4.

4.4.1 FEM models of Kagawa and Glenn USMs

The finite element discretization and electrode configuration of Kagawa motor and Glenn motor considered are shown in Fig. 4.2.

The Kagawa stator is made of an annular plate of brass with thickness of 2.5 mm, and a piezoelectric ceramic plate with thickness of 0.5 mm is bonded on the lower surface of the brass ring. They have the same inner diameter of 40 mm and outer diameter of 60 mm. For computation purpose, the brass plate is sub-divided into 2 layers, one with thickness of 0.5 mm (contact layer) and the other with thickness of 2.0 mm (structural layer). The rotor is an annular steel plate, assumed to be rigid.

The Glenn stator comprises an annular plate of 544 phosphor bronze with thickness of 1.5 mm, on top of which is bonded 72 teeth made of the same material with height 1.0 mm. A piezoelectric ceramic plate with thickness of 0.5 mm is bonded on the lower surface of the annular plate. They have the same inner diameter of 47 mm and outer diameter of 60 mm. The Glenn rotor comprises an annular aluminum plate with a 0.2 mm

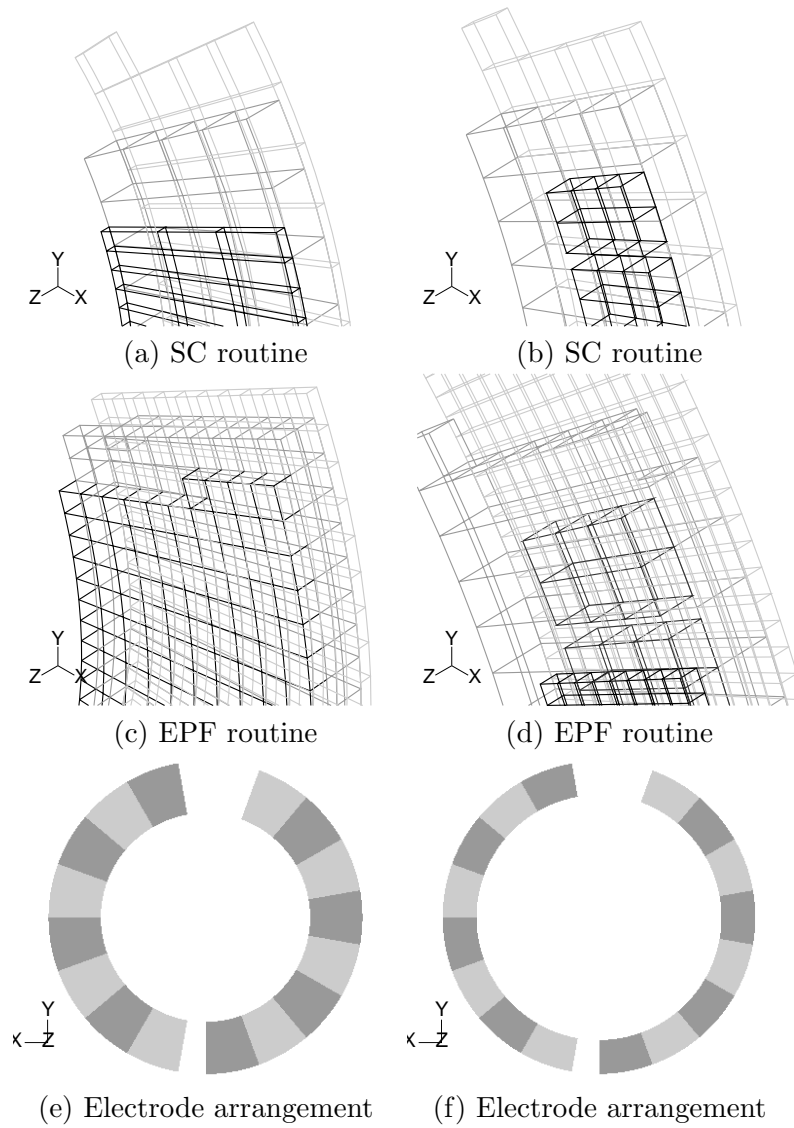


Figure 4.2: FE discretization in SC and EPF routines and electrode arrangement of Kagawa (a, b and c) and Glenn motors (d, e and f)

thick contact layer of Ekonol/PTFE bonded on its lower surface. Their inner diameter is 53 mm and outer diameter is 61 mm.

The finite element discretizations are different for the two procedures. In the SC procedure, the number of finite elements in (r, θ, z) directions for the Kagawa stator with respect to the piezoelectric patch, annular plate and contact layer are $4 \times 72 \times 1$, $4 \times 60 \times 1$ and $3 \times 144 \times 1$ respectively as shown in Fig. 4.2 (a). The number of elements for the Glenn motor with respect to the piezoelectric patch, annular plate, teeth and rotor are $4 \times 108 \times 1$, $4 \times 108 \times 1$, $3 \times 2 \times 1$, and $4 \times 178 \times 1$ respectively as shown in Fig. 4.2 (d). To simulate the bending behavior, solid elements with 20 nodes (C3D20RE and C3D20R) are adopted for the piezoelectric patch and structural ring in both stators. For the contact layer in the Kagawa stator and the teeth and rotor in the Glenn motor, solid elements with 8 nodes (C3D8) are adopted.

In the EPF procedure, the finite elements used for the Kagawa stator and Glenn motor comprise 1 mm cuboids as shown in Fig. 4.2 (b) and Fig. 4.2 (e). Solid elements with 8 nodes and reduced integration (C3D8R) are adopted.

Electric potential ϕ exists explicitly only in the SC procedure and are assumed to be zero on the top surfaces of the piezoelectric patches for both motors. Specific distribution of electric potential ϕ is prescribed on the bottom surface to generate traveling waves. The piezoelectric patch is assumed to be uniformly polarized along the z -direction. Its bottom electrode is divided into 18 segments (or groups of elements) as shown in Fig. 4.2 (c) and Fig. 4.2 (f). Of these, two groups of 8 segments are separated by 2 white segments. The electrical potential on the left group of 8 segments follows a cosine time function and that on the right follows a sine time function. In each group, the electrical potential on the darker shaded part are always out-of-phase with that on the lighter part. The

prescribed potential ϕ on the bottom surface can be written as follows:

$$\phi = \begin{cases} -V_0 \sin(\omega t) & \theta \in [0, \frac{1}{9}\pi] \cup [\frac{2}{9}\pi, \frac{1}{3}\pi] \cup [\frac{4}{9}\pi, \frac{5}{9}\pi] \cup [\frac{2}{3}\pi, \frac{7}{9}\pi] \\ V_0 \sin(\omega t) & \theta \in [\frac{1}{9}\pi, \frac{2}{9}\pi] \cup [\frac{1}{3}\pi, \frac{4}{9}\pi] \cup [\frac{5}{9}\pi, \frac{2}{3}\pi] \cup [\frac{7}{9}\pi, \frac{8}{9}\pi] \\ -V_0 \cos(\omega t) & \theta \in [\frac{19}{18}\pi, \frac{21}{18}\pi] \cup [\frac{23}{18}\pi, \frac{25}{18}\pi] \cup [\frac{3}{2}\pi, \frac{29}{18}\pi] \cup [\frac{31}{18}\pi, \frac{33}{18}\pi] \\ V_0 \cos(\omega t) & \theta \in [\frac{21}{18}\pi, \frac{23}{18}\pi] \cup [\frac{25}{18}\pi, \frac{3}{2}\pi] \cup [\frac{29}{18}\pi, \frac{31}{18}\pi] \cup [\frac{33}{18}\pi, \frac{35}{18}\pi] \end{cases} \quad (4.49)$$

where ω is the frequency of the electrical potential.

Using a thermal analogy, the corresponding temperature distribution to simulate the converse piezoelectric effect in the EPF routine is obtained via Eqs. (4.47) and (4.49). The material constants used in the calculation are tabulated in Table 4.1. The thermal expansion coefficient should be set according to Eq. (4.46).

Table 4.1: Material properties

Property	Brass	Bronze	Ekonal/PTFE	PZT4		
Young's module (GPa)	100.6	103.5	0.7	$C_{11}^E = 139$	$C_{12}^E = 77.8$	$C_{13}^E = 74.3$
				$C_{33}^E = 115$	$C_{44}^E = 25.6$	$C_{66}^E = 30.6$
Poisson ratio	0.35	0.33	0.33	-		
Mass density (kg/m ³)	8560	8893	1950	7600		
Piezoelectric constant (C/m ²)	-	-	-	$e_{31} = -5.2$	$e_{15} = 12.7$	$e_{33} = 15.1$
Permittivity(nF/m)	-	-	-	$\epsilon_{11}^S = 13.06$	$\epsilon_{33}^S = 11.51$	-

4.4.2 Analysis of Kagawa motor

4.4.2.1 Free vibration of stator

The eigenvalues for the Kagawa stator with free boundary condition used in both SC and EPF procedures are extracted and listed in Table 4.2. They agree with those obtained by Kagawa *et al.* (1996), especially the frequency corresponding to the ninth mode.

4.4.2.2 Input parameters for SC and EPF procedures

In the SC procedure, the frequency of the ninth flexural mode is 45.39 kHz, and its period T_9 is 22.03 μ s. Setting the electrical voltage at this frequency with amplitude of 50V, the dynamic responses of the stator are computed using Newmark time integration with

Table 4.2: Comparison of frequencies (kHz) of Kagawa stator

n	p	SC routine ^a	EPF routine	Kagawa ^b	Difference between a and b(%)
0	2	1.934	1.921	-	-
	3	5.328	5.268	-	-
	4	9.928	9.840	-	-
	5	15.568	15.486	14.760	5.47%
	6	22.080	22.055	21.228	4.01%
	7	29.307	29.396	28.601	2.47%
	8	37.115	37.402	36.785	0.90%
	9	45.393	45.912	45.685	-0.64%
	10	54.057	54.879	55.210	-2.09%

p = number of nodal diameters.

n = number of nodal circles.

a time step of $0.5 \mu\text{s}$ (or about $T_9/44$). The stator is assumed to have free boundary conditions. Rayleigh damping coefficients are set to be $\alpha = 116.491$, $\beta = 3.364 \times 10^{-8}$, which correspond to the first and ninth flexural mode each with damping ratio of 0.5%.

In the EPF procedure, the frequency of the ninth flexural mode is 45.91 kHz. Setting the temperature at this frequency with amplitude of 100000° , the dynamic responses of the stator are computed using explicit central difference integration. The stator is assumed to have free boundary conditions (kinematics coupling constraints). The damping ratios are set to be the same as those in the SC procedure.

4.4.2.3 Dynamic analysis of stator

The time history of u_θ , u_z and v_θ of the upper surface of the stator computed by the SC and EPF procedures from 3.8 - 4.0 ms are in a good agreement as can be seen by comparing Fig. 4.3 (a) and (b); for example, the amplitudes of u_θ , u_z and v_θ are $0.7128 \mu\text{m}$, $2.347 \mu\text{m}$ and 0.202 m/s by SC and $6.621 \mu\text{m}$, $2.167 \mu\text{m}$ and 0.207 m/s by EPF. The phase relationships between u_θ , u_z and v_θ are also the same in both Fig. 4.3 (a) and (b). The phase difference between u_z and v_θ is zero, and between u_θ and u_z is $\pi/2$.

From the amplitude and phase difference between u_θ , and u_z in Fig. 4.3, it can be concluded that a traveling wave is generated on the stator. This is reasonable theoretically

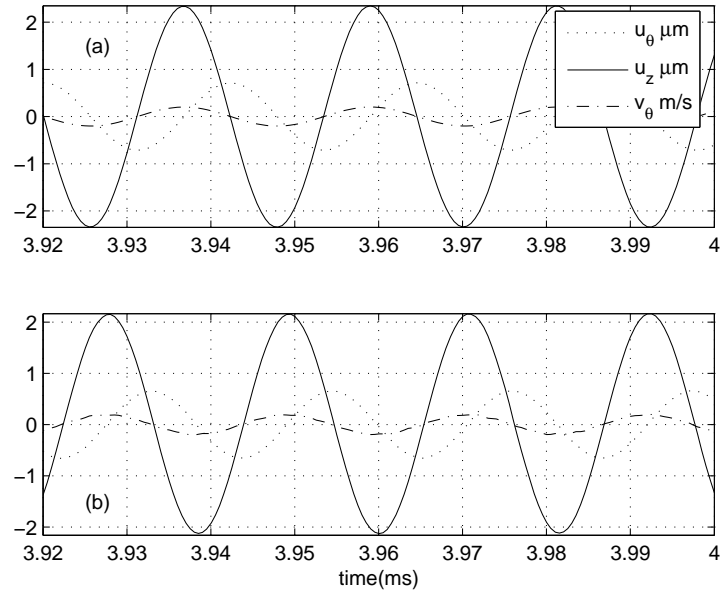


Figure 4.3: Displacements and velocity at upper surface of Kagawa stator by (a) SC and (b) EPF routines

(Wallaschek, 1998) as shown in Eqs. (1.7)-(1.10). The conclusions from Fig. 4.3 can be obtained that (1) the circumferential velocity v_θ of the material points becomes maximum when the transverse displacement u_z reaches its maximum; and (2) the displacement trajectory becomes elliptic.

4.4.2.4 Steady-state analysis by SC procedure

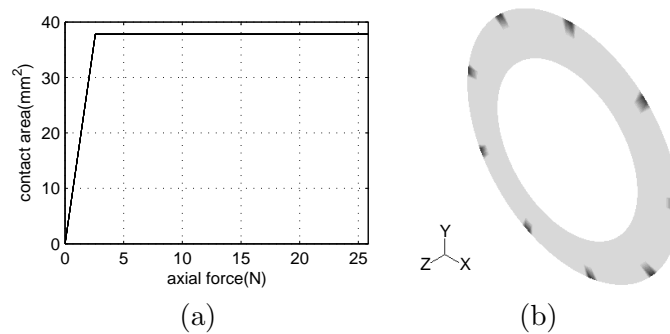


Figure 4.4: (a) Axial force applied on rotor and (b) corresponding contact area in Kagawa motor by SC routine

Based on the displacement and velocity fields of the stator from dynamic analysis using the SC procedure presented above, the steady-state contact between the deformed stator and rotor can be quantified. The stator is assumed to be fixed on the inner edge

at the deformed configuration in order to compute the contact force and the coefficient of friction μ is assumed to be isotropic with a value of 0.3. The rotational speed and axial displacement u_z of the rotor are prescribed. For a range of speed from 0 to 60 rpm and u_z from 0 to 1.5 μm , the axial force computed varies from 0 to 26 N.

The axial force applied on the rotor and the corresponding contact area between the rotor and stator is plotted in Fig. 4.4 (a), from which one can see the contact area is virtually constant (about 38 mm^2 or 2.3% of the top surface area of the stator) during contact beyond a small force level. The nine contact areas located at the outer edge on the top surface of the stator are plotted in Fig. 4.4 (b). In view of the small areas and contact pressure, it may be assumed that the vibration of the stator is not affected by the contact force significantly.

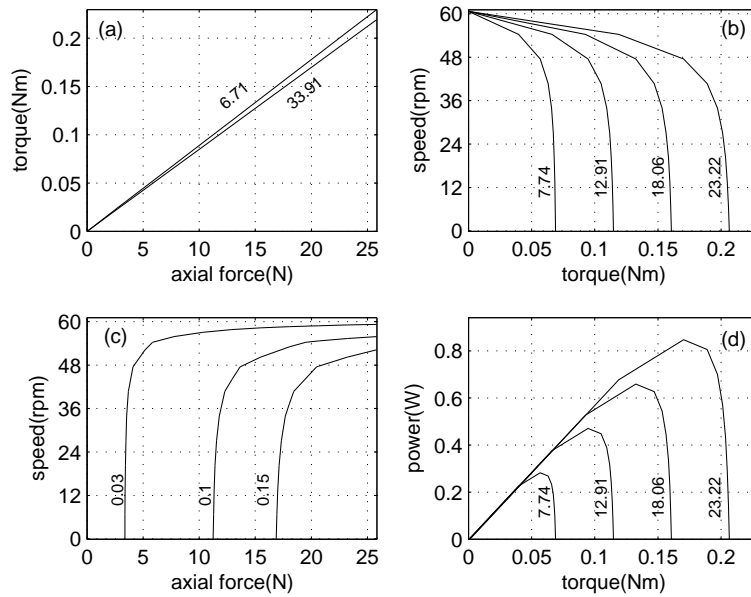


Figure 4.5: Overall behavior of Kagawa motor by SC routine

The overall behavior of USM are computed and shown in Fig. 4.5. They are the relationship between (a) axial force and torque with varying rotor speed; (b) torque and rotor speed with varying axial force; (c) axial force and rotor speed with varying torque and (d) torque and power with varying axial force. From Fig. 4.5 (b), (c) the stick

and slip contact status is obvious although the transition between them is not so sharp because the stator is not an ideally rigid in the FEM model. The stick speed ranges from 0 to 40 rpm where the rotor speed is almost independent of the axial force and torque. In addition, the power increases with torque as shown in Fig. 4.5 (d) and the torque is proportional to the normal force as shown in Fig. 4.5 (a). Beyond 40 rpm where slipping occurs, the torque and axial force are independent of the rotor speed shown in Fig. 4.5 (b) and (c) and the power is independent of torque as shown in Fig. 4.5 (d).

These results are reasonable theoretically. From Fig. 4.4, point contacts may be assumed (Flynn, 1995; Wallaschek, 1998) and the interaction between stator and rotor can be described by the normal and tangential forces F_N and F_T , respectively. For the case of stick (no slipping), the contact points of stator and rotor have the same velocity. For a traveling wave, the circumferential velocity of the stator's contact point v_ϕ^* is given by Eq. (1.11) and the resulting rotational speed of the rotor is

$$\omega_{rotor} = \frac{h_c}{r_c} \frac{AR(r)}{r_c} \omega n \quad (4.50)$$

In this equation, r_c is the radius of contact and h_c the distance between contact interface and middle surface of the stator; $R(r)$ is a dimensionless function of the stator's deflection in the r -direction, which is usually normalized so that A can be interpreted as the modal amplitude for a particular radius of interest. For the case of slipping, the motor torque is constant

$$M_T = \mu F_N \text{sign}(\omega_{rotor}) r_c \quad (4.51)$$

for all rotary speeds. Eqs. (4.50) and (4.51) verified the results of Fig. 4.5, that is, the rotary speed in the stick regime is independent of the normal (axial) force, while the motor torque in the slip regime is proportional to the axial force and independent of the rotor speed.

The no-load speed and stall torque are two characteristic parameters for performance of USMs. The torque produced by an ultrasonic motor is determined by the friction force

Table 4.3: Comparison of operational parameters of Kagawa motor

Parameters	SC routine	Kagawa <i>et al.</i> (1996)	
		Numerical results	Experimental results
v_{θ}^* (m/s)	0.2	0.138	-
ω_{rotor} (rpm)	60.6	50.2	56
Stall torque (Nm)	0.138	0.123	-

at the rotor-stator interface. For a given excitation voltage and applied normal force, there will be a set of speed-torque operating points at which the motor will run, depending on the load it must drive. With no load, the motor will spin at its no-load speed and when the load is increased to the point that the rotor no longer moves, the motor is delivering its stall torque. The no-load speed and stall torque provide two operating points on the speed-torque curve. ω_{rotor} without load, stall torque (axial force 15.6N) and v_{θ}^* , are computed and compared with experimental and numerical results (Kagawa *et al.*, 1996) shown in Table 4.3. The results from proposed routine are reasonable, for example, v_{θ}^* and stall torque are 0.2 and 0.138 by the proposed routine and 0.138 and 0.123 provided by Kagawa *et al.* (1996) respectively. In addition, for ω_{rotor} without load, a more accurate value of 60.6 is given by the proposed routine compared to 50.2 provided by Kagawa using the equivalent electric circuit method.

4.4.2.5 Transient analysis by EPF procedure

The importance of a contact layer in practical USM is demonstrated by the results from the EPF model. The results of transient overall behavior analysis by EPF exhibit some problems as shown in Fig. 4.6. Under some small axial displacement of stator, u_z , say 0.5×10^{-5} m, which results in small contact force, Kagawa motor can work properly. However, when the displacement of the stator gets larger, the contact between the stator and rotor becomes stronger and the stator resonates at a lower frequency causing the EPF procedure to fail, which replicates the actual case in practice. Hence, the contact layer is necessary for the steady operation of USM.

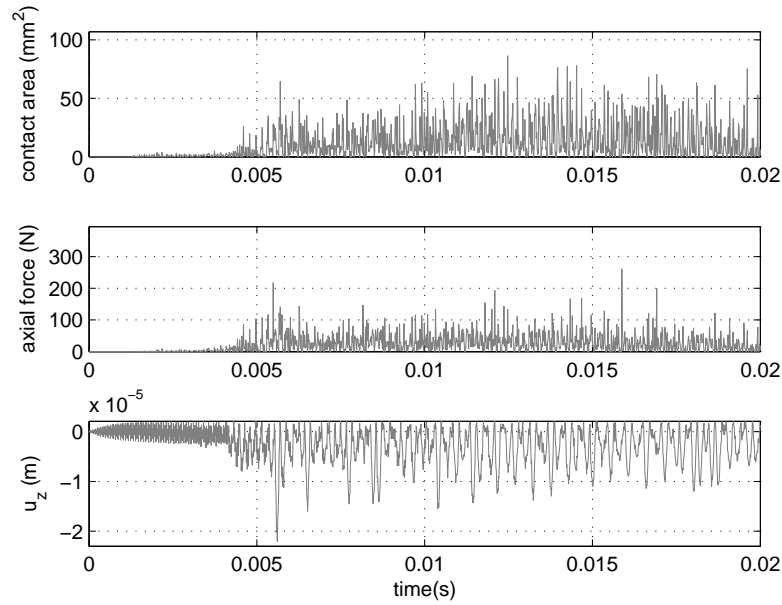


Figure 4.6: Transient response of intermittent-contact in Kagawa motor by EPF routine

4.4.3 Analysis of Glenn motor

4.4.3.1 Free vibration of stator

Table 4.4: Comparison of frequencies (kHz) of Glenn stator

n	p	SC routine ^a	EPF routine	Glenn ^b	Difference between a and b(%)
0	0	18.691	18.352	-	-
	1	18.873	18.545	-	-
	2	19.446	19.148	-	-
	3	20.479	20.223	-	-
	4	22.060	21.851	-	-
	5	24.270	24.105	-	-
	6	27.158	27.032	-	-
	7	30.734	30.647	-	-
	8	34.974	34.932	-	-
	9	39.832	39.851	39.957	-0.3%
10	45.250	45.353	-	-	

p = number of nodal diameters.

n = number of nodal circles.

The eigenvalues of Glenn stator used in both SC and EPF procedures are extracted and listed in Table 4.4. The kinematics coupling constraints based boundary conditions are set such that the value for the ninth mode agrees with that given by Glenn (2002).

4.4.3.2 Input parameters for SC and EPF procedures

The input values for the load, boundary conditions and damping ratio are the same as those for the Kagawa motor.

4.4.3.3 Steady-state analysis by SC procedure

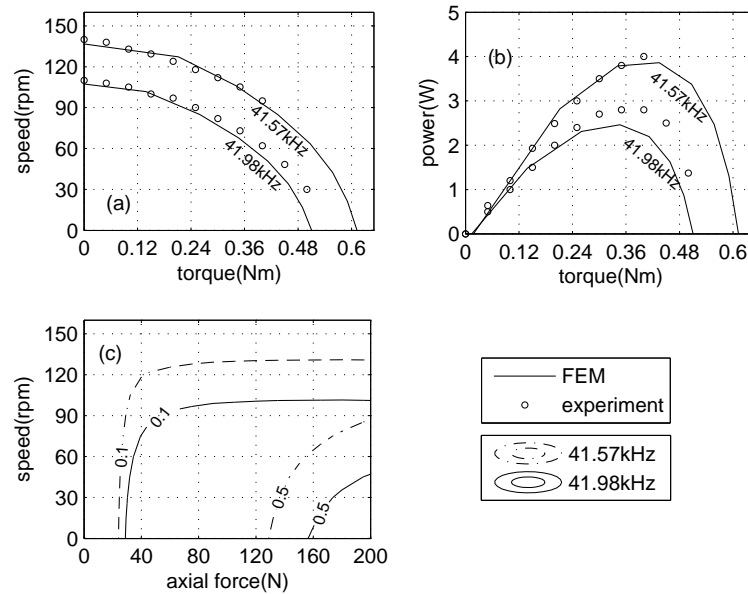


Figure 4.7: Glenn motor overall behavior vs. frequency at $150 V_p$ by SC routine

The overall behavior of Glenn stator (Glenn, 2002) is first solved at a fix drive voltage of $150 V_p$ for two different drive frequencies: 41.57 kHz and 41.98 kHz, same as those adopted in reference (Glenn, 2002). The computed performance curves at these frequencies are plotted in Fig. 4.7, comprising the relationship between (a) torque and rotor speed; (b) torque and power; (c) axial force and rotor speed with two cases of torque, 0.1 and 0.5 Nm. The experimental results of reference (Glenn, 2002) are compared in Fig. 4.7(a) and (b).

The results compare well. For example, with frequency of 41.57 kHz and torque of 0.40 Nm, the rotor speeds predicted by the FE model and experiment are 92 rpm and 96 rpm respectively, and the output powers are 3.9 W and 4.0 W, respectively.

Another observation is that the effect of driving frequency on the overall behavior of USM, namely, motor speed, torque and power increases as the drive frequency approaches that of resonance. For example, in Fig. 4.7(a) with a torque of 0.40 Nm, the rotor speeds predicted by FE model are 96 rpm and 58 rpm at frequencies of 41.57 and 41.98 kHz respectively, and with rotor speed of 100 rpm, the corresponding torques predicted by FE model are 0.37 and 0.15 Nm. In Fig. 4.7(b) with a torque of 0.40 Nm, the power predicted by FE model are 3.8 and 2.3 W at frequencies of 41.57 and 41.98 kHz respectively. This effect may be due to the electrical-mechanical energy transition in the piezoelectric ceramics attaining its highest efficiency when the ceramics is in its resonant state.

A third observation can be made by comparing the speed-axial force and torque-axial force curves in Fig. 4.7 with those of Fig. 4.3. In Fig. 4.3, the transition between stick and slipping is more distinct because the contact area is small. However in Fig. 4.7, the boundary between stick and slip is less distinct because of the larger contact area due to the presence of the softer contact layer. The effect of the soft layer is also illustrated by the fact that the rotor speed and torque are highly dependent on axial force when the latter is large, in contrast with those for the case of point contact shown in Fig. 4.3 (Flynn, 1995; Wallaschek, 1998).

To investigate the overall behavior of USM for different drive voltages, Glenn motor is solved at a fix drive frequency of 41.57 kHz for drive voltages of 50 V_p , 100 V_p , 150 V_p and the results are shown in Fig. 4.8, namely, the relationship between voltage and (a) amplitude of u_z ; (b) speed at a torque of 0.2 Nm; (c) torque at a rotor speed of 70 rpm; (d) power at a torque of 0.2 Nm. Although steady state displacement amplitude on the surface of the stator is linear with voltage amplitude as shown in Fig. 4.8(a), the speed, torque and power vary non-linearly with the voltage amplitude as shown in Fig. 4.8(b)-(d). In fact, the speed, torque and power are about 5, 1 and 4 times higher at 150 V_p than those at 50 V_p respectively, demonstrating the non-linear characteristic of intermittent contact.

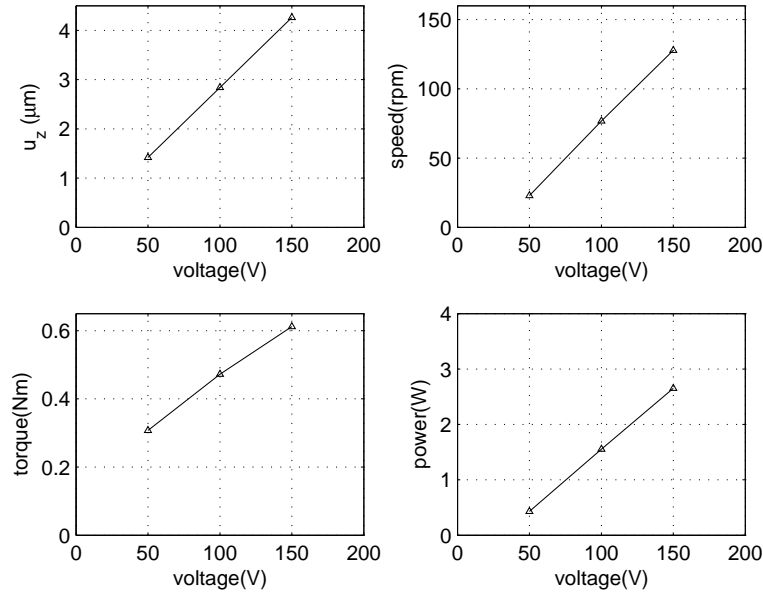


Figure 4.8: Glenn motor overall behavior vs. voltage at 41.57 kHz by SC routine

4.4.3.4 Dynamic analysis by EPF procedure

The overall behavior of Glenn stator (Glenn, 2002) is solved using the EPF routine at a drive voltage of $150 V_p$ and drive frequency of 41.57 kHz. The transient responses of Glenn motor with zero rotor speed are plotted in Fig. 4.9. The speed and torque curve plotted in Fig. 4.10 compares well with that from the SC procedure.

The ability to simulate transient response is shown in Fig. 4.9. The dynamics resulting from the intermittent-contact are reflected in the high frequency but small amplitude fluctuations exhibited by the start-up curves shown in Fig. 4.9(a)-(c). The importance of a softer contact in damping out the transient vibration to achieve steady-state operation is obvious by comparing Fig. 4.9 with Fig. 4.6. Hence, the contact layer, structural details and control system must be properly designed for operational efficiency.

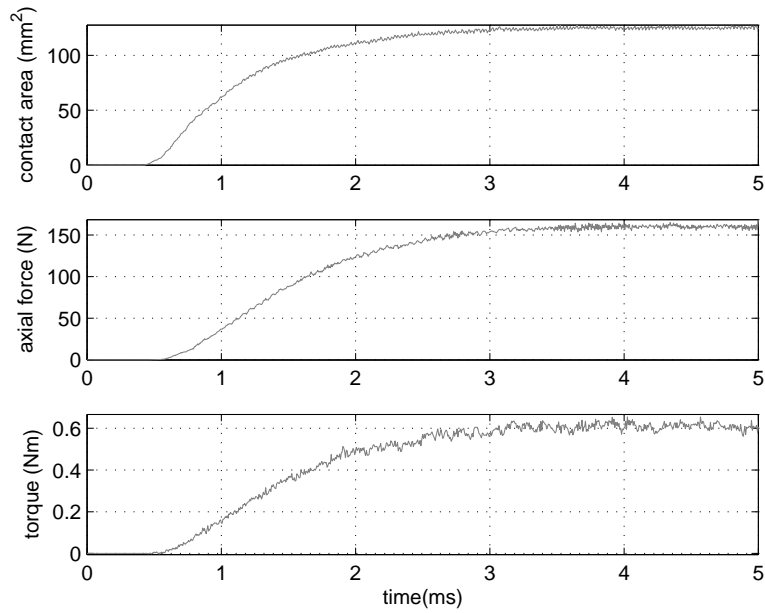


Figure 4.9: Transient responses of Glenn motor at 41.57 kKz and 150 V_p by EPF routine

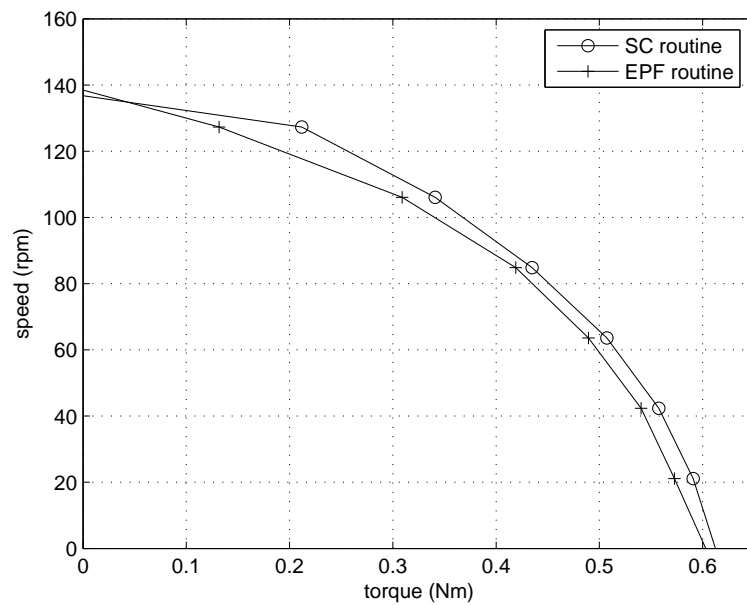


Figure 4.10: Comparison of speed torque curve of Glenn motor by SC and EPF routine at 41.57 kKz and 150 V_p

4.5 Conclusion

Procedures for analyzing the overall behavior of USM have been proposed and demonstrated by FE analysis using commercial software ABAQUS[®] version 6.4. The difficulties of FE analysis for the intermittent-contact problem with piezoelectric actuation are highlighted and the SC and EPF procedures are proposed. Numerical examples are used to obtain the stator dynamics, steady-state and transient behavior of USM to illustrate the feasibility of the two procedures. The results are consistent with published numerical and experimental results. Transient intermittent-contact responses which are not available in published literature are presented and show the advantage of EPF over the SC procedure. In addition, the contact layer, structural details and control system must be properly designed for operational efficiency. Although the solution techniques presented in this chapter are based on piezoelectric traveling wave USM, the same approach can be used to solve other intermittent-contact problems with piezoelectric actuation, such as linear USM.

CHAPTER 5

Design, Fabrication and Characterization of a Ring Type USM with Multiple Wave Numbers

Analytical model and numerical procedures have been developed in Chapters 2, 3 and 4 for efficient conceptual and preliminary design purpose of piezoelectric coupled structures. Another objective of the proposed research, the realization of USM with multiple wave numbers, is experimentally studied in this chapter. In Section 5.1, the basic concept for the novel implementation of USM with multiple wave numbers is introduced. The fabrication of USM prototype is detailed in Section 5.2. This is followed by the characterization of USM prototype including that of its experimental and simulated overall performance.

5.1 Design of USM with multiple wave numbers

In recent years, tremendous attention has been drawn to a new type of motor, namely the traveling-wave USM. It offers many advantageous features over the traditional electromagnetic motor, namely high torque at low speed, light weight, compact size, fast response, no electromagnetic interference, and quiet operation as described in Chapter 1.

However, the USM suffers from some shortcomings, such as exhibiting unsteady performance characteristics. The reason is mainly because of the fluctuation in the system parameters with time caused by wear, temperature built-up and load variation. In order to overcome these problems, many control algorithms, such as proportional integral and derivative (PID) control (Izuno *et al.*, 1998; Senjyu *et al.*, 2001, 1996), fuzzy logic control (Bai *et al.*, 2004; Izuno *et al.*, 1992), adaptive control (Senjyu *et al.*, 2002, 1998), neural network control (Bekiroglu and Daldal, 2005; Lin *et al.*, 2001; Shi *et al.*, 2004), and combined control algorithms (Chau *et al.*, 2003; Lin *et al.*, 1999a; Senjyu *et al.*, 2000), have been proposed to improve the performance of USM with respect to speed (Bal and Bekiroglu, 2005; Chen and Lin, 2002; Xu *et al.*, 2003), position (Chau and Chung, 2001; Lin *et al.*, 2000) and torque (Giraud *et al.*, 2004). In these control algorithms, frequency, phase shift and amplitude of electrical voltage sources are adopted as control variables. However, each of these control variables has its own disadvantages, such as very narrow controllable frequency range, dead-zone intervals in phase control, and voltage amplitude threshold. Therefore, it is of significance in theory and applications to introduce a new control variable, namely the wave number, as the fourth variable in a traveling wave USM besides amplitude, frequency, and phase angle. In conventional USM, such as the Sashida motor (Ueha and Tomikawa, 1993), the wave number is fixed due to the alternating piezoelectric polarization directions.

The purpose of this chapter is to design, fabricate and characterize a novel USM with multiple wave numbers, which is realized by a new design of piezoelectric electrode configuration and corresponding driving electronics. It is hoped that this novel design of USM can give wider controllability to improve the performance of USM.

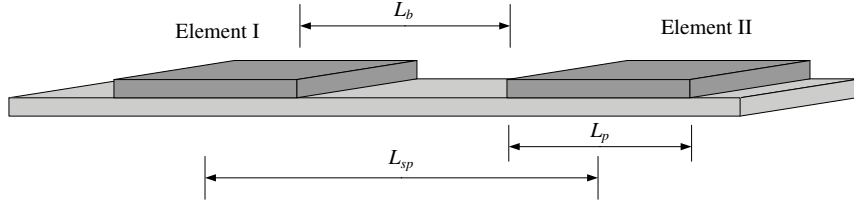


Figure 5.1: Excitation of a traveling wave by bonded piezoelectric ceramics

5.1.1 Piezoelectric configuration

5.1.1.1 Conditions for excitation of traveling waves in a ring

To understand the multiple wave numbers operation in an USM, the generation of traveling waves in USM using piezoelectric ceramics is first investigated first. Two piezoelectric ceramic elements I and II are bonded on an infinite bar as shown in Fig. 5.1. It is assumed that these two piezoelectric ceramic elements have the same material properties and geometry. From elastic mechanics theory, standing waves will propagate along two directions of the bar when one of two piezoelectric ceramic elements is excited. When equal electrical voltages are applied on two elements, four standing waves are generated and the transverse displacement of the stator's middle surface can be expressed respectively as

$$w_1 = A \sin(\omega t - kx) + A \sin(\omega t + kx) \quad (5.1)$$

$$w_2 = A \sin(\omega t - k(x + L_{sp}) + \varphi) + A \sin(\omega t + k(x + L_{sp}) + \varphi) \quad (5.2)$$

where kL_{sp} is the spatial phase shift between piezoelectric elements and φ the phase shift in time.

By defining the following variable transformations:

$$-kL_{sp} + \varphi = \varphi_1, \quad kL_{sp} + \varphi = \varphi_2 \quad (5.3)$$

Eq. (5.2) can be rewritten as

$$w_2 = A \sin(\omega t - kx + \varphi_1) + A \sin(\omega t + kx + \varphi_2) \quad (5.4)$$

In Chapter 1 it is mentioned that a traveling wave can be generated by combination of two standing waves with $\pi/2$ phase shift in both time and spatial domains. If the following conditions are satisfied:

$$\begin{aligned}\varphi_1 &= m\pi, & m &= 0, \pm 2, \pm 4, \dots \\ \varphi_2 &= n\pi, & n &= \pm 1, \pm 3, \pm 5, \dots\end{aligned}\tag{5.5}$$

then the combined wave of Eqs. (5.1) and (5.4) is expressed by

$$\begin{aligned}w &= w_1 + w_2 = A \sin(\omega t - kx) + A \sin(\omega t + kx) \\ &+ A \sin(\omega t - kx + m\pi) + A \sin(\omega t + kx + n\pi) \\ &= 2A \sin(\omega t - kx)\end{aligned}\tag{5.6}$$

resulting in a traveling wave.

From these results, the conditions for excitation of a traveling wave using the set-up in Fig. 5.1 can be found from Eqs. (5.3) and (5.5):

$$L_{sp} = \lambda(n - m)/4, \quad \varphi = (n + m)\pi/2 \quad (m \neq n)\tag{5.7}$$

That is, the following four cases can exist:

$$L_{sp} = \lambda/4, \quad \varphi = \pi/2, \quad (n = 1, m = 0)\tag{5.8a}$$

$$L_{sp} = 3\lambda/4, \quad \varphi = 3\pi/2, \quad (n = 3, m = 0)\tag{5.8b}$$

$$L_{sp} = 5\lambda/4, \quad \varphi = 5\pi/2, \quad (n = 5, m = 0)\tag{5.8c}$$

$$L_{sp} = 7\lambda/4, \quad \varphi = 7\pi/2, \quad (n = 7, m = 0)\tag{5.8d}$$

5.1.1.2 Comparison of excitation conditions

Some limitations of the application of conditions in Eq. (5.8) need to be noted. For high power actuation, the length of piezoelectric patches, L_p , should be as large as possible, however, its maximum length is $\lambda/2$ for the actuation of elastic wave with wavelength λ ; while the spacing between two piezoelectric elements, L_b , should be as short as possible. However, it is confined by $L_{sp} = L_b + L_p$. Considering these limitations, the configurations 5.8a and 5.8b are better than other two cases 5.8c and 5.8d, and their application in a

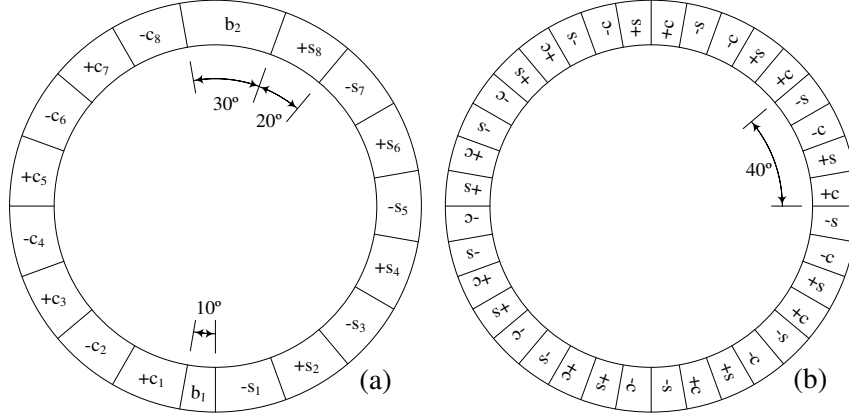


Figure 5.2: Comparison of piezoelectric ceramic electrode configurations with wave number 9

ring type USM with wave number 9 is shown in Fig. 5.2. Case 5.8a is plotted in Fig. 5.2 (a) while case 5.8b in Fig. 5.2 (b).

In Fig. 5.2 (a), the electrode of piezoelectric ring is divided into 18 segments with three sizes of $\lambda/4$ (10°), $\lambda/2$ (20°) and $3\lambda/4$ (30°), where the segments with size $\lambda/2$ are for actuation, and the segments with sizes $\lambda/4$ and $3\lambda/4$ are blank segments (b_1 and b_2). The two blank segments separate the actuation segments into two groups c_i and s_i ($i = 0 \dots 8$). The electrical potential on c_i ($i = 0 \dots 8$) follows a cosine time function and that on s_i ($i = 0 \dots 8$) follows a sine time function. In each group, the input power for each segment, for example $+c$ and $-c$ (similarly, $+s$ and $-s$) are 180° out of phase. Electrical voltages are not normally applied on b_1 and b_2 and are used as sensors. Thus, each set, $[c_i, b_1, \text{ and } s_i]$ ($i = 0 \dots 8$), forms one configuration corresponding to Case 5.8a.

In Fig. 5.2 (b), the electrode of piezoelectric ring is divided into 36 segments with equal length of $\lambda/4$ (10°). These form nine groups of $+c$, $-c$, $+s$ and $-s$ covering the whole surface of the ring, each group realizing the configuration corresponding to Case 5.8b.

By comparing Figs. 5.2 (a) and (b), one can see more piezoelectric elements is involved in the actuation in Case 5.8b. If the polarization of piezoelectric elements is reversed every half wavelength (indicated by $+$ and $-$), only two channels of driving

electronics are necessary to actuate the motor in Case 5.8a while Case 5.8b needs four channels which is harder to realize in practice. So Case 5.8a is widely adopted in commercial USM, such as the Sashida motor (Ueha and Tomikawa, 1993). However if reversed polarization at every half wavelength is difficult, for example when piezoelectric film is used, Case 5.8b is more suitable. An example of which is the Flynn motor (Flynn, 1995).

5.1.1.3 Realization of multiple wave numbers operation

With the above background on the generation of traveling waves in USM using piezoelectric ceramics, piezoelectric electrode configurations of USM with 8 different wave numbers, 3, 4, 5, 6, 9, 10, 18 and 20 are proposed and shown in Figs. 5.3 and 5.4 respectively. Similar to the segmentation of distributed piezoelectric sensors and actuators in vibration control (Bailey and Hubbard, 1985; Lee and Moon, 1990; Sun *et al.*, 1999; Tzou and Fu, 1994b,a), all piezoelectric patches have the same polarization direction, which is normal to the plate. Its electrodes on top in the piezoelectric patch are divided into 80 equal segments shown in Fig. 5.3 (a), which can realize wave number 20 corresponding to Case 5.8b. The multiple wave numbers, 4, 5 and 10, are realized by controlling the

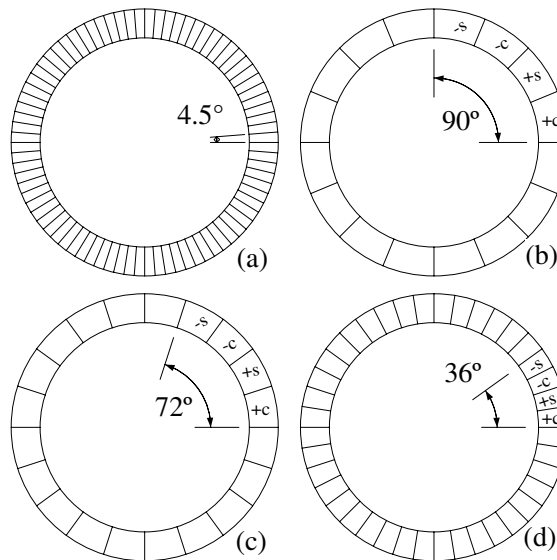


Figure 5.3: Piezoelectric ceramic electrode configurations of USM with wave number (a) 20, (b) 4, (c) 5 and (d) 10

connection between the segmented electrodes shown in Fig. 5.3 (b-d). Specifically, the

combination of blocks of 5, 4 and 2 segments of the electrode from the 80 segments give rise to the configurations with wave numbers 4, 5 and 10. Similarly, if the electrodes on bottom of the piezoelectric ring patch are divided into 72 equal segments shown in Fig. 5.4 (a), wave number 18 corresponding to Case 5.8b can be realized. The multiple wave numbers, 3, 6 and 9, are realized by controlling the connection between the segmented electrodes shown in Fig. 5.4 (b-d).

For clarity in each of Figs. 5.3 (b-d) and 5.4 (b-d), the applied voltage on the electrodes are only shown over one wavelength as $+s$, $+c$, $-s$ and $-c$, with phase shifts of 90° . The electrodes on the other eight groups have the same set of voltage arrangement. It is noted that the resonant frequencies corresponding to the wave numbers may not be as high as that in the range of ultrasonic wave. Hence, the term "ultrasonic motor" may not be truly appropriate while the phrase "piezoelectric driving motor" would be a better description for such motor with multiple wave numbers. However, following the current accepted terminology, the term "ultrasonic motor" is still used in this thesis.

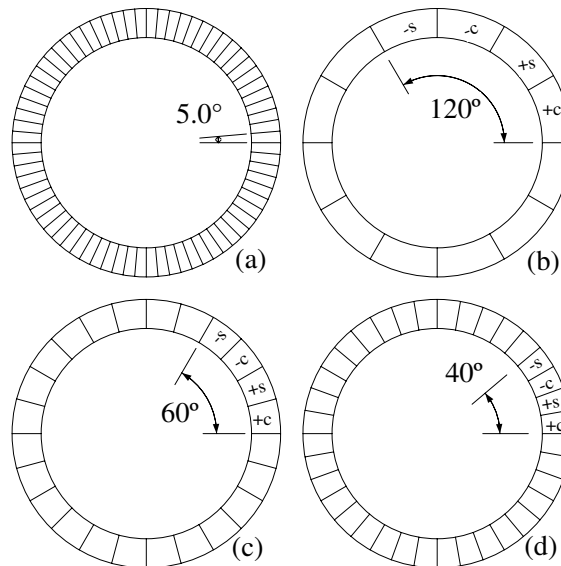


Figure 5.4: Piezoelectric ceramic electrode configurations of USM with wave number (a) 18, (b) 3, (c) 6, and (d) 9

In order to generate a traveling wave along the ring, it is necessary for the driving electronics to have four channels, each separated by a phase shift of 90° as shown in

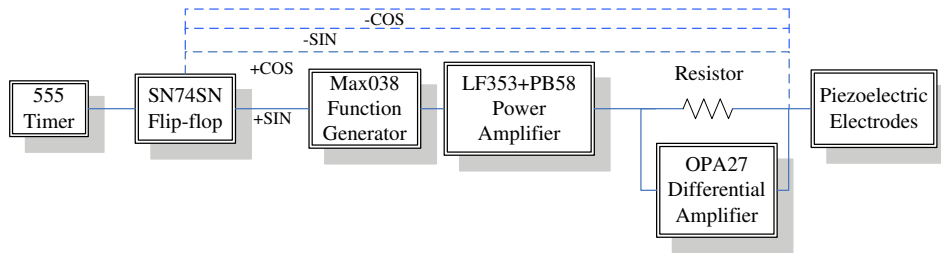


Figure 5.5: Integrated electronics used in the actuation and sensing of the stator's piezoceramic elements

following section.

5.1.2 Driving electrical circuit

Several circuits are required to properly drive and amplify the signals sent to the electrodes of the piezoceramics and to monitor the current flow through the piezoceramics. Section 5.1.2.1 describes the circuit used to generate the four channels waveforms (\pm sine, \pm cosine) needed to create a traveling wave within the stator. The waveforms alone are not enough, however, to create motion in the stator. Section 5.1.2.2 illustrates the details of the high power amplifiers used to increase the voltage and current to produce sufficient deflection (at resonance) in the stator to accomplish rotor motion. Lastly, as input power to the stator is a parameter of interest, it becomes necessary to monitor not only the input voltage but the input current as well. This requires a differential amplifier circuit, as will be explained in Section 5.1.2.3. Fig. 5.5 shows how all these electronics interact with one another and Appendix C shows the detailed drawing of the driving electrical circuit. All designs have been accomplished using Orcad[®].

5.1.2.1 Waveform generator

To generate the four channels waveforms $+s$, $+c$, $-s$ and $-c$ that are mentioned earlier, three ICs, namely MAX038, TCL555 and SN74SN74A, are used as shown in Figs. 5.6 and 5.7, where MAX038 adjusts the four channels waveforms frequency and TCL555 and SN74SN74A ensure their phase shift.

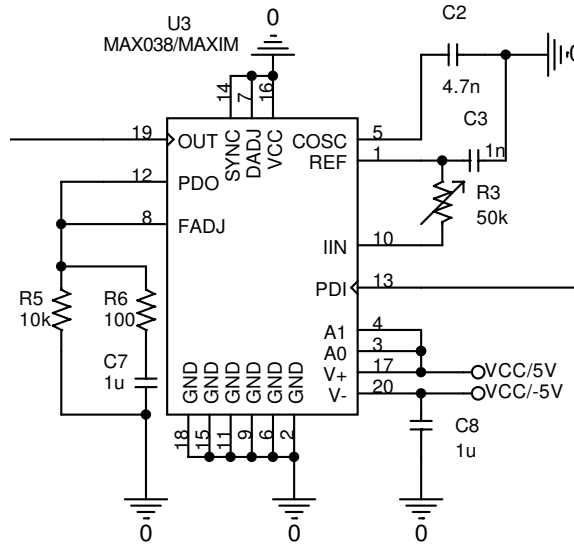


Figure 5.6: Waveform generator MAX038

Four MAX038 High Frequency Waveform Generators (Maxim, 2005) as shown in Fig. 5.6 are used to produce low-distortion sine, triangle, saw-tooth, or square (pulse) waveforms at frequencies from below 1Hz to more than 20MHz. The TTL/CMOS-logic address pins (A0 and A1) are used to set the waveform. For example, the sine waveform can be set by connecting A1 with V+. The output frequency is determined by the current (I_{IN}) injected into the IIN pin, the COSC capacitance (C2), and the voltage on the FADJ pin. When $V_{FADJ} = 0V$, the fundamental output frequency (F_o) is given by the formula

$$F_o(\text{MHz}) = I_{IN}(\mu\text{A}) \div C2 (\text{pF}) \quad (5.9)$$

IIN can be driven with a voltage (REF) in series with a resistor (R3), where REF is a stable 2.50V internal reference. Hence the formula for the oscillator frequency is

$$F_o(\text{MHz}) = V_{REF} \div [R3 \times C2 (\text{pF})] \quad (5.10)$$

The voltage on DADJ controls the waveform duty cycle (defined as the percentage of time that the output waveform is positive). Normally, $V_{DADJ} = 0V$, and the duty cycle is 50%.

After setting the 4 channels waveforms frequency, the next problem is to set their phase shift. The MAX038 contains a TTL/CMOS phase detector that can be used in a

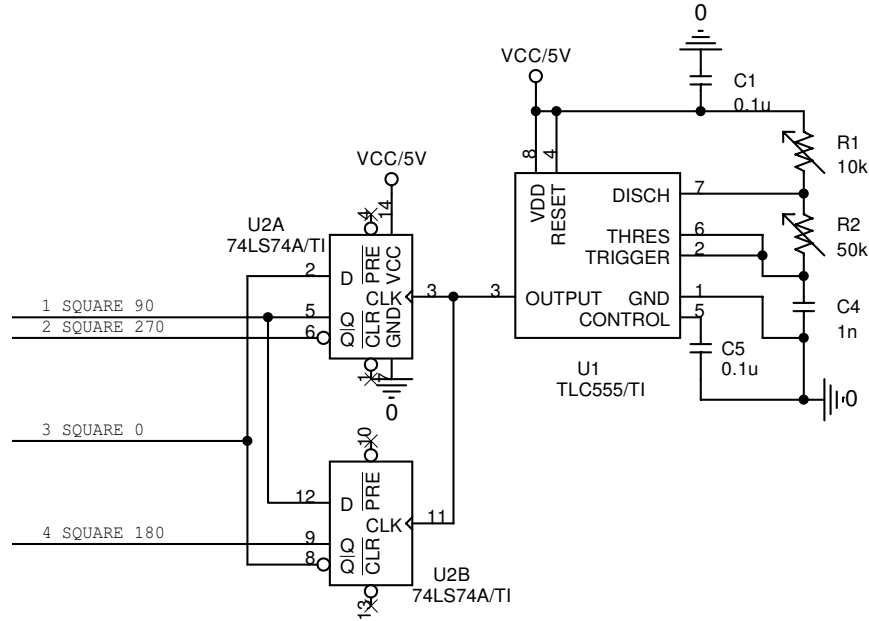


Figure 5.7: TLC555 timer and SN74LS74A flip-flop

phase-locked loop (PLL) to synchronize its output to an external signal. For example, suppose MAX038 has a wave output with frequency $\omega + \Delta\omega$, where $\Delta\omega$ is the frequency fluctuation. The external wave with frequency ω is connected to the phase-detector input (PDI). MAX038 will conduct phase detection and the phase-detector output (PDO) is a set of rectangular current waveforms at frequencies equal to the sum ($2\omega + \Delta\omega$) and difference ($\Delta\omega$) of the external wave frequency and the MAX038 output frequency. The high-frequency component $2\omega + \Delta\omega$ will be attenuated by a low-pass filter formed by R5, C7, and R6, and the $\Delta\omega$ component is connected to FADJ (FADJ is mainly intended for fine frequency control) to remove the MAX038 output frequency fluctuation so that the MAX038 output and external waves have same frequency.

To generate an external source which synchronize the MAX038 output, TLC555 timer (TI, 2005a) and SN74LS74A dual-D positive edge-triggered flip-flop (TI, 2005b) (U1 and U2 shown in Fig. 5.7) are used. The output frequency of TCL555 (F_o) is given by the formula

$$F_o = 1/[C4(R1 + 2R2) \times \ln 2] \quad (5.11)$$

Its output will connect to the flip-flop SN74SN74A, and then the flip-flop's outputs

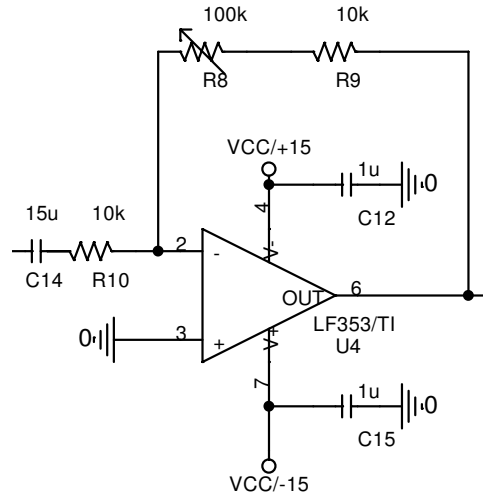


Figure 5.8: LF353 power amplifier

provide the square-wave signals with 0, 90, 180 and 270 degrees phase shift.

Both ceramic and electrolytic bypass capacitors between the power pins and ground shown in Figs. 5.6 and 5.7 ensure that only DC voltages are supplied to the ICs. This is a precaution taken to prevent any oscillation that may have fed through to the output signal.

5.1.2.2 Power amplifiers

The drive electronics explained in the previous section provide the four channels of voltage signals necessary to generate the traveling wave. The purpose of the power amplifiers is to increase the voltage and provide the necessary current. The electrical voltage of power amplifiers is set to have a variable range from $10V_p$ to $100V_p$ based on the rated voltage of commercial Sashida USM (Ueha and Tomikawa, 1993). The current requirement of USM can be found from capacitor characteristics of piezoelectric ceramics. The current flow through a capacitor is given by

$$I = \omega CV_p \quad (5.12)$$

where ω and V_p are the frequency and voltage respectively. Using Eq. (5.12) with a 18 nF piezoelectric load (measured value) and a 100 V_p drive signal oscillating at the resonant

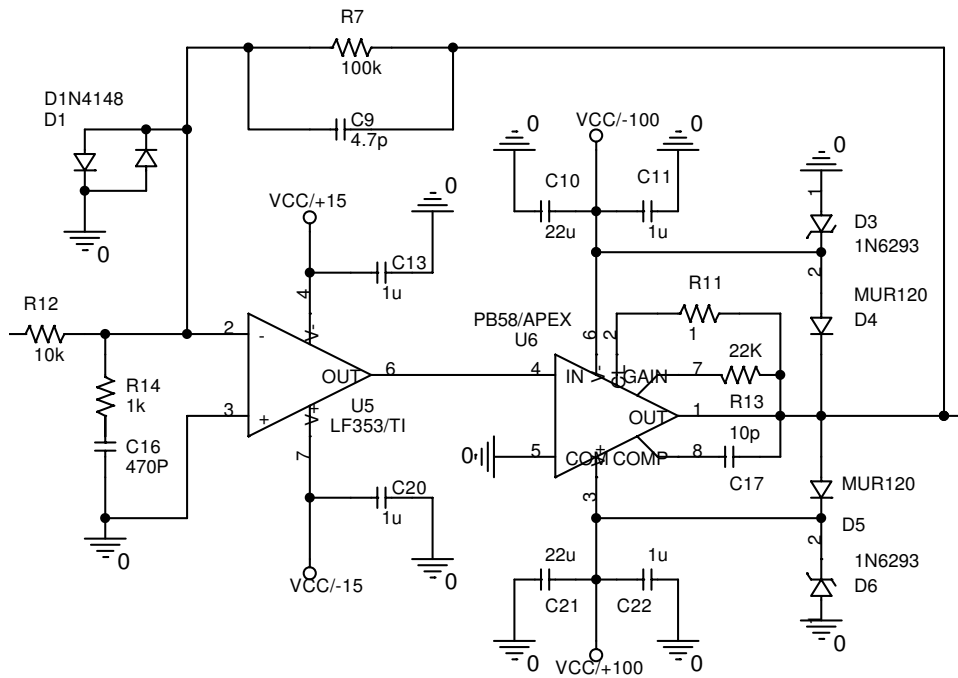


Figure 5.9: Composite amplifier by LF353 and PB58

frequency of roughly 40 kHz, an estimated current of 450 mA is required.

From the datasheet of MAX038 (Maxim, 2005), the amplitude of its voltage output is $1.0 V_p$, so the power amplifier needs a gain of 100 to increase the voltage to $100 V_p$. The power amplifier circuit consists of two stages. The first is an attenuator, LF353 op-amp (TI, 2005c) (U4 shown in Fig. 5.8), which is set to have a gain 1-10 with the values of $R9 = 10 \text{ k}$, $R10 = 10 \text{ k}$ and trimmer R8 with a maximum value of 100 k. The attenuator allows the voltage output at Pin 6 to range between 1 and $10 V_p$. The second stage is a composite amplifier comprising a LF353 op-amp and a PB58 op-amp (Apex, 2005c) (U5 and U6 shown in Fig. 5.9) with a fixed gain of 10 accomplished by setting the ratio of the feedback to input impedance at 10 with the values of $R12 = 10 \text{ k}$ and $R7 = 100 \text{ k}$. So the voltage applied on the piezoelectric ceramics can be varied from 10 to $100 V_p$. The current output requirement of 450 mA can be satisfied based on the datasheet of PB58 where a maximum current output of 1.5A can be achieved.

There are several components that need to be carefully set to ensure performance of the composite amplifier. First is the setting of gain resistor R13. Although the total

gain of the composite amplifier is targeted as 10, there is still a need to determine how much amplification the driver LF353 and the booster PB58 perform individually. It is desirable that the booster has as small a voltage gain as possible because it is responsible for all of the current supplied and thus heat dissipation becomes an issue. However, the driver with a maximum input voltage of $10 V_p$ from the attenuator is operating near its saturation limit. Therefore, the booster performs all the voltage and current amplification. Based on the data sheet of PB58 (Apex , 2005c), it is estimated that the gain resistor, R13, should have a value of 21.7 k for the booster to have a gain of 10. For ease of construction, a 22 k resistor is used.

Second is the current limiting resistor R11. From the datasheet of PB58 (Apex , 2005c), the following formula is given by

$$I \approx 0.65 \div R3 \quad (5.13)$$

Considering the current requirement of piezoelectric load is 450 mA, according Eq. (5.13), the resistor is then set at 1Ω .

Third is the compensation of the composite amplifier for stability. All the compensation are designed by an Apex Application Engineer (Apex , 2005b) and is summarized concisely here. The compensation capacitor is attached directly to the PB58, C17 with a value of 10 pF, to tailor between the slew rate and loop stability of PB58. The effects of capacitive load induced by the piezoceramics on the amplifier is countered by feedback compensation, accomplished by the use of C9 with a value of 4.7 pF, and noise gain compensation network, realized through the use of R14 with a value of 1 k and C16 with a value of 470 pF.

Fourth is the protection of the composite amplifier. The diode network D1 and D2 at the input terminal protects the LF353 and PB58 from large transients caused by feedback of C9 from the output to the input. The diodes attached to the output, D4 and D5, ensure that the output voltage does not overwhelm the rail voltages, which may occur

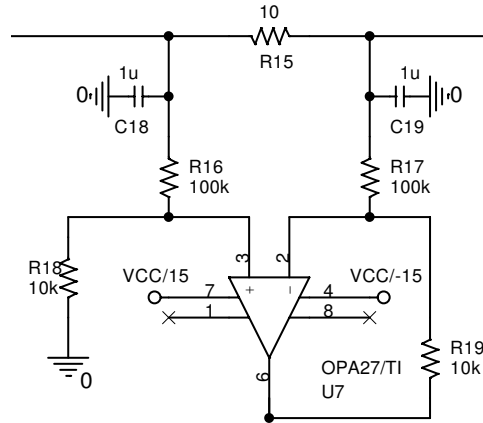


Figure 5.10: Current monitor differential amplifier OPA27

in a piezoelectric drive situation where the piezoelectric ceramics is stressed mechanically, thereby creating an electrical voltage. Lastly, the diodes D3 and D6 associated with the rail voltages are used to provide protection from undesired transients on the power supply.

5.1.2.3 Differential amplifiers

In order to monitor the current flow through the piezoelectric ceramics, four identical ultra-low noise precision op-amp OPA27 (TI, 2005d) (U7 shown in Fig. 5.10) are used, one for each channel. The working principle of OPA27 can be shown in Eq. (5.14). In general, if $R16/R18=R17/R19$, the current flow through the piezoelectric ceramics is directly a function of the differential amplifier's output voltage:

$$I_{\text{piezo}} = \frac{R16 \times V6}{R18 \times R15} \quad (5.14)$$

where I_{piezo} is the current flowing through the piezoelectric ceramics and $V6$ is the voltage of pin 6 in U7.

To have a good performance of OPA27, the voltage divider, R16 and R18 need to be set carefully. The rail voltage of OPA27 is $+15 V_p$, and the piezoelectric drive voltage is nominally $100 V_p$. Op-amp saturation can easily occur. Resistors 16 and 18 is set up with values chosen to drop the voltage at the positive input terminal to a reasonable level, in this case to $10 V_p$.

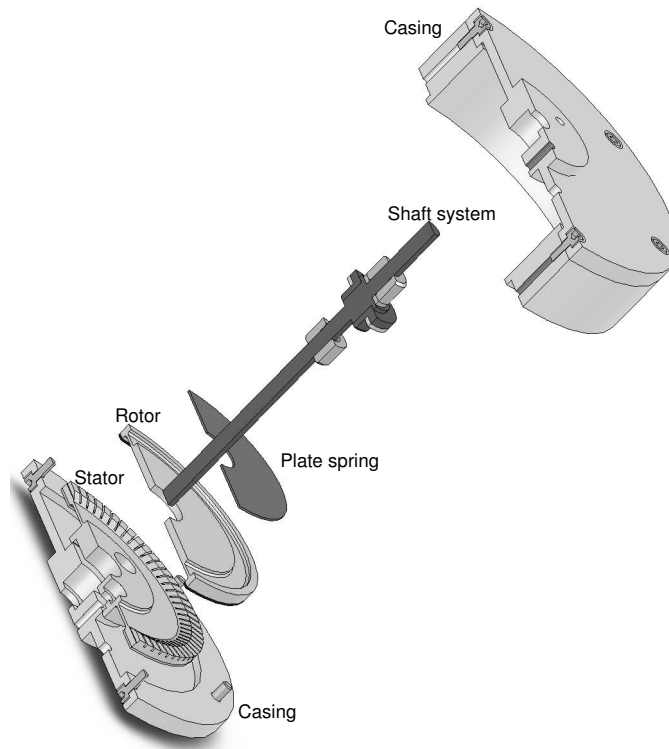


Figure 5.11: Explode view of USM prototype

5.1.3 Mechanical parts

Having discussed the piezoelectric configurations, and electronic components and circuit for the power supply to the USM with multiple wave numbers, the next problem is the design of mechanical parts. Sashida motor (Ueha and Tomikawa, 1993) is a well documented example of a piezoelectric traveling wave motor and is therefore adopted as a reference for designing the rotor and the stator. An exploded view of the mechanical assembly of the USM prototype developed is shown in Fig. 5.11. The stator is made of an annular plate of aluminum with thickness of 2.0 mm, on top of which is 72 teeth made of the same material with height of 1.0 mm. A piezoelectric ceramic plate (C91H) with thickness of 0.5 mm is bonded on the lower surface of the annular plate. They have the same inner diameter of 47 mm and outer diameter of 60 mm. The rotor comprises an annular aluminum plate with a 1.0 mm thick contact layer of PolyTetraFluoroEthylene (PTFE) bonded on its lower surface. Their inner diameter is 54 mm and outer diameter is 58 mm. The detailed mechanical drawings are presented in Appendix D using

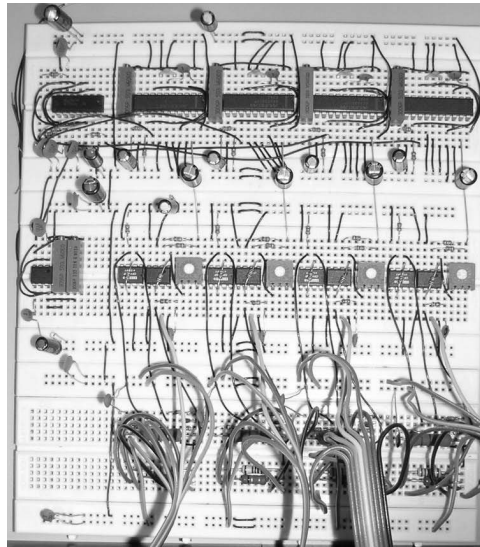


Figure 5.12: Power supply of USM

SolidWorks®.

5.2 Fabrication of USM prototype

To validate the concept of USM with multiple wave numbers, the electrical and mechanical designs discussed above are used to fabricate a prototype motor. The assembly of the driving electronics is done in-house using breadboard as shown in Fig. 5.12. However, the machining of the mechanical components are outsource to a professional workshop in view of the tight tolerances needed to build a functioning ultrasonic motor. Outlined here are the steps and practices followed during the preparation and assembly of the various components of the USM. These include etching, bonding, lapping and wiring.

5.2.1 Piezoelectric ceramics preparation

In Section 5.1.1, a piezoelectric electrode configuration with 8 different wave numbers are presented as shown in Figs. 5.3 and 5.4. However considering the machinability, the configurations of wave number 5 and 10 are experimentally realized in this dissertation.

The piezoceramic rings are supplied by FUJI® with a uniformly poled state in the z



Figure 5.13: Fabricated piezoelectric ring in USM prototype

direction and silver powder electrodes plated on either side. In-house preparation includes dividing the bottom electrode of the ring into 40 equal segments as shown in Fig. 5.13, to correspond to Fig. 5.3 (d). This configuration can realize the operation corresponding to wave number 10. For wave number 5, it can be realized by connecting two adjacent segments into one segment.

To minimize stress fracture of the fragile wafers, chemical etching is adopted instead of using electric-arc or more abrasive techniques. Nitric acid (37% wt) is used to etch the silver powder electrodes, while paraffin wax is used to mask off the desirable electrode surfaces and steel needle with 0.05 mm diameter needlepoint is adopted to remove paraffin wax on the etch line. As seen in Fig. 5.13, the etched lines between electrode sectors are approximately 0.1 mm wide.

5.2.2 Stator preparation

Stator preparation includes teeth polishing on the top surface of stator and piezoelectric ceramics ring bonding on the bottom surface as shown in Fig. 5.11. Before bonding the piezoceramic rings, the stator teeth are polished on a flat Perspex surface using silicon carbide papers as shown in Fig. 5.14 (a). Starting with a 400-grit paper for coarse material removal, the process is repeated with increasingly finer papers down to 1200-grit to produce the very flat, smooth finish required for efficient operation. A final polish with 2000-grit silicon carbide paper provides a mirror-like finish. To ensure the removal

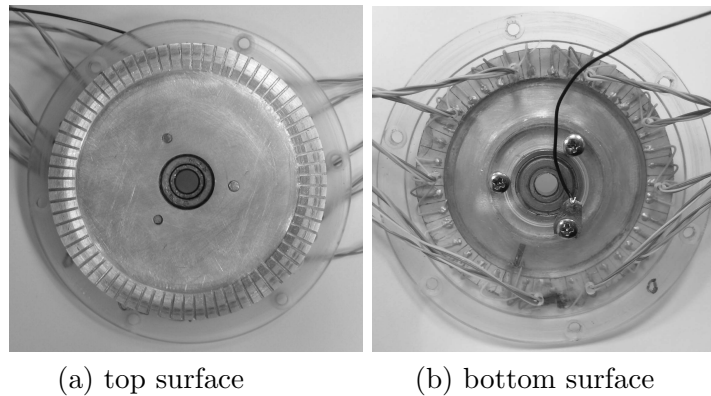


Figure 5.14: Fabricated stator in USM prototype

of all silicon carbide particles, de-greasing of the stator in an acetone bath is needed in the final step.

While taking care not to scratch the finely polished teeth, the bonding surfaces of the stator substrate and piezoelectric wafer are then wet grind with 400-grit sand paper and again de-greased with acetone to remove any fingerprints. Circuitworks Model CW2400 conductive epoxy is chosen for bond application because of its excellent electrical conductivity and high strength conductive bonding. The bonding is secured under a normal pressure of 100 kPa maintained at a curing temperature of 80C using model VT 5042EK vacuum drying oven (Heraeus®) for two hours.

Piezoceramic ring is bonded with its segmented electrodes facing outward in order to provide full access to the individual sectors for multiple wave numbers drive operation as shown in Fig. 5.14 (b). Consequently, an additional step is necessary to wire the segmented electrode arrays. Connection between wires and piezoelectric electrodes arrays is realized by CW2400 conductive epoxy to complete the assembly.

5.2.3 Rotor preparation

As seen in Fig. 5.15, preparing the rotors involved two steps. One step is the bonding of rotor and polymer layer and other is lapping the polymer contact surface.

The polymer material of PolyTetraFluoroEthylene (PTFE) is highly resistant to



(a) Bonding of rotor and polymer (b) Contact surface on polymer

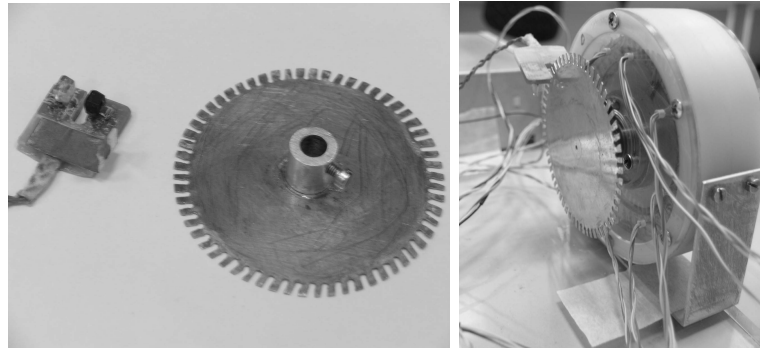
Figure 5.15: Fabricated rotor in USM prototype

bonding in its natural state. Polymer preparation is limited to cutting the ring and scrubbing the treated bonding surfaces with acetone. The bonding surfaces of the aluminum rotor are roughened and cleaned following the procedures specified for the preparation of the stator described in the previous sub-section. Devcon 2-Ton white epoxy is chosen for fixing the polymer ring to the aluminum rotor after preliminary tests demonstrated that the bond is stronger than the polymer and hence will not peel under load. Following the procedures developed for the stator, the sandwiched rotors are cured at 80°C for two hours under a normal pressure of 100 kPa using weights as shown in Fig. 5.15 (a).

The contact surface of polymer layer on the rotor are polished on silicon carbide paper starting with 400-grit for bulk removal and working down to 1000-grit as shown in Fig. 5.15 (b). Flatness is maintained by firmly securing the paper to a Perspex slab, and the paper is kept wet to ensure constant removal of material. Finer grits are unnecessary as the soft polymer would naturally achieve its final finish during the initial wear period of motor operation.

5.3 Preparation for characterization

To this end, an USM prototype with multiple wave numbers has been constructed. This section is dedicated to describing the preparation for the characterization of USM prototype and verification of a numerical simulation model presented in Section 5.4.



(a) Light source and receiver and wheel (b) Assemble of encoder

Figure 5.16: Experimental setup for speed measurement

In this context, characterization refers to measurements and calculations of the motor performance including rotational speed, torque, power and efficiency. Mechanical output power can be computed once the speed and torque are determined. Efficiency is determined once the electrical input power and mechanical output power are known. As shown in Chapter 4, the control of preload (axial force) for the good contact between stator and rotor is needed for the operation of USM. For the numerical simulation model, modal parameters such as resonant frequencies and their corresponding damping of the stator must be determined to actuate the piezoelectric ceramics to achieve resonance. In addition, frictional coefficient between PTFE and aluminum is needed as input in the simulation of contact.

There are eight variables that need to be measured, namely, rotational speed, torque, preload, input electrical voltage and current, resonant frequencies and damping of stator, and coefficient of friction. The experimental instruments for measurements are presented in Section 5.3.1 and the controlling experimental conditions are presented in Section 5.3.2.

5.3.1 Experimental instruments

5.3.1.1 Speed measurement

Speed is monitored by an optical encoder, where the encoder wheel has 60 slots and a light source and a receiver are shown in Fig. 5.16 (a). They are mounted on a virtually

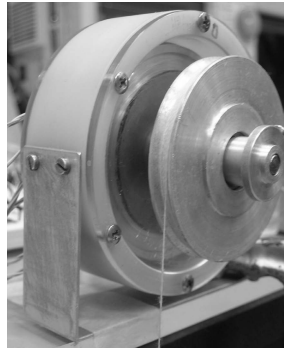


Figure 5.17: Experimental setup for torque measurement

frictionless shaft for accurate speed measurement and a resolution of 6° can be achieved as shown in Fig. 5.16 (b). A pulse counter (Microcontroller AT89S51) is employed to interpret the digital signal coming from the light receiver and is programmed to display the measurement directly in revolutions per minute (rpm).

5.3.1.2 Torque and coefficient of friction measurement

A pulley with a radius of 23.5 mm and weights are used to load the motor as shown in Fig. 5.17. Once the weight used is known, the torque can be easily calculated. Nylon thread, chosen for its lightness, is used to support the weight. The weights used ranges from 5.0g - 50.0g N. To generate the empirical performance curves, several input torques are used.

An experiment is performed to estimate the coefficient of friction between PTFE and aluminum to be used in the simulation. When the stator is turned on, the rotor spins due to the effect of friction. If an opposite torque is applied through added weights on the pulley system, a stage can be reached where the pulley begins to stall. An additional small amount of weight will cause the rotor to slip in a direction opposite the stator's surface motion. The dynamic coefficient of friction can be derived from this torque. If the stator is not switched on, the static coefficient of friction can be obtained using the same concept.



Figure 5.18: Strain gage for axial force measurement

5.3.1.3 Axial force measurement

The preload is set by varying the thickness of the appropriate washer. In order to know the force applied at the rotor/stator interface, several steps are taken. A strain gage is attached on the stator as shown in Fig. 5.18. A calibration curve for the stator spring is determined by applying known forces and measuring the resulting strains and the correlation between them is obtained. In this case, a linear curve fit is found to be suitable and used to determine the preload. A digital strain meter TC-31K (Tokyo Sokki Kenkyujo Co., Ltd.) is used to measure the strain in a half-bridge Wheatstone set-up.

5.3.1.4 Electrical variables measurement

The detailed electronics are described in Section 5.1.2. To measure the input power to the motor, input voltage and current to the piezoelectric ceramics, an oscilloscope (Yokogawa Model DL708E) with a maximum acquisition rate of 10 million samples per second is used.

5.3.1.5 Resonant frequencies and damping coefficients measurement

Resonant frequencies and damping can be measured using the *single degree of freedom curve fit* (often called the SDOF method) approach (Ewins, 2000; He and Fu, 2001; Inman, 1994; Maia *et al.*, 1997). In this method of resonance testing, the stator is excited

harmonically by four adjacent segments of piezoelectric ceramics (one wavelength), and the re-activated voltage amplitudes on other piezoelectric electrodes are measured. The piezoelectric ceramics are taken here as actuators and sensors simultaneously based on piezoelectric coupling effects. The amplitude is then plotted against driving frequency, which is named as amplitude-frequency curve of stator. From this curve, the modal damping ratio is calculated by using the *half-power* method.

5.3.2 Controlling experimental conditions

The prototype is tested under controlled conditions. Some factors need to be set carefully. A major concern is initial wear. When a motor is first assembled, performance can change dramatically over time as the newly-mat polymer surface temporarily undergoes some wear. With use, the mating improves and wear then slows to a negligible rate resulting in a more stable motor performance. Consequently, before any valid measurements are documented, the newly assembled motor is driven continuously for an appropriate period of time until its speed and input power are observed to be steady. The burnt-in procedure typically lasts several hours.

Another important concern while testing the motors is the internal heating caused by the contact interface. Essentially, performance is strongly influenced by temperature and must be recognized. Therefore, to provide validity and consistency of the experimental performance measurements, it is deemed necessary to stabilize the temperature. The experiments are performed in an air conditioned room with a stable environmental air temperature of 20°C. In addition, a fan is used to extract the local heat in the USM. Finally throughout all experimental testing, each measurement is finished within one minute and the USM is cooled down for 10 minutes before operating for the next measurement.

5.4 Characterization of USM with multiple wave numbers

To demonstrate the extent to which the preceding design concept of multiple driving wave numbers operation of USM can be realized, the operation of the prototype motor is characterized. The results are also used to validate a numerical simulation model so that the latter can be used to further characterize the motor to minimize the need to resort to additional physical experimental test.

Using the set-up described in Section 5.3, steady-state motor performance is measured under carefully controlled conditions. Parametric studies on varying drive frequency and voltage, and the effect of contact layer have been studied in Chapter 4. This chapter focused mainly on the performance of USM with different wave numbers. Three cases are studied, namely, wave number 10 with voltage $60 V_p$ (denoted by w10v60), wave number 10 with voltage of $20 V_p$ (w10v20) and wave number 5 with voltage of $60 V_p$ (w5v60). Preload for all cases are set at 4.1 N. To verify the FEM simulation model presented in Chapter 4, using the procedure demonstrated in Chapter 4 the numerical results are obtained for all cases performed experimentally. All computations are performed using ABAQUS[®] version 6.4.

Table 5.1: Material properties

Property	Al	PTFE	C91H		
Young's modulus (GPa)	70	0.56	$C_{11}^E = 138.1$	$C_{12}^E = 89.3$	$C_{13}^E = 93.1$
			$C_{33}^E = 131.3$	$C_{44}^E = 24.0$	$C_{66}^E = 24.4$
Poisson ratio	0.33	0.46	-		
Mass density (kg/m ³)	2700	2170	8110		
Piezoelectric constant (C/m ²)	-	-	$e_{31} = -18.81$	$e_{15} = 22.16$	$e_{33} = 24.34$
Relative dielectric constants	-	-	$\epsilon_{11}^S/\epsilon_0 = 2699$	$\epsilon_{33}^S/\epsilon_0 = 2383$	-
Coefficient of friction	0.07 (Counterparts: Al and PTFE)				

5.4.1 Modal parameters of stator

The resonant frequencies are first extracted from FEM model of the stator, which is the same as those shown in Chapter 4. The material constants used in the calculation are

tabulated in Table 5.1, in which, the dynamic coefficient of friction is measured using the method described in Section 5.3.1.2. The frequency results are shown in Table 5.2. Next,

Table 5.2: Comparison of resonant frequencies (kHz) of stator

n	p	FEM	Measured	p	FEM	Measured
0	1	-	-	6	21.77	-
	2	5.17	-	7	28.10	-
	3	8.07	-	8	35.20	-
	4	11.72	-	9	42.97	-
	5	16.29	16.1	10	51.34	48.8

p = number of nodal diameters.

n = number of nodal circles.

the resonant frequencies and damping ratios are measured using the methods described in Section 5.3.1.5. At the motor start-up, the frequency of the drive signal is varied in the vicinity of the predicted resonant frequency until maximum re-activated voltage occurred. The amplitude is plotted against driving frequency shown in Fig. 5.19. The dominant peak value is taken as the experimental value of resonant frequencies, which are not far from the predicted ones.

In the third step, the Rayleigh damping coefficients (α and β) are determined from the resonance curve shown in Fig. 5.19. The resulting damping coefficients and damping ratios are summarized in Table 5.3.

Table 5.3: Experimental results of damping

Paramters	Value
Damping ratio ξ for the fifth mode (%)	1.0
Damping ratio ξ for the tenth mode (%)	1.6
α	1.120×10^3
β	8.843×10^{-8}

5.4.2 Overall behavior of USM with multiple wave numbers

Steady-state motor performance of the cases w10v60, w10v20 and w5v60 are measured. In Section 5.4.2.1, the experimental data are compared with those from FEM model to verify the numerical method. In Section 5.4.2.2, four control variables, namely amplitude,

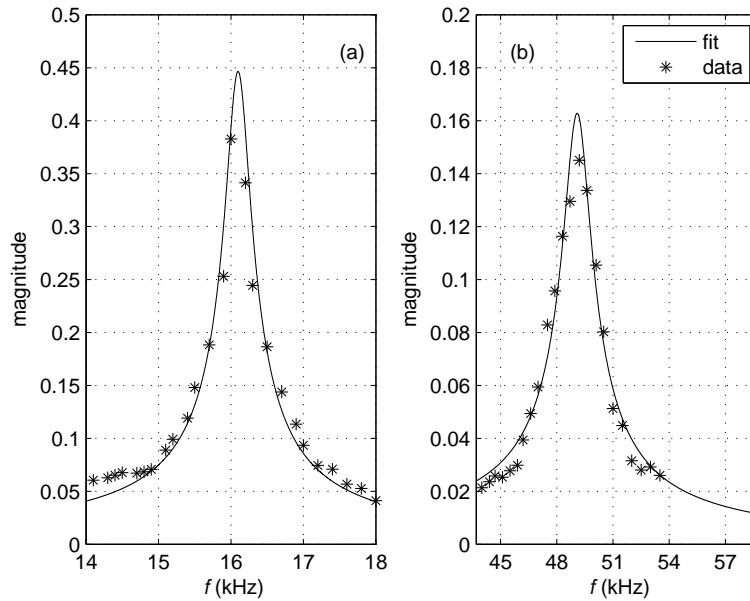


Figure 5.19: Resonant frequency behavior of stator for (a) fifth and (b) tenth modes

frequency, phase and wave number are compared based on stator dynamics, meaning that the effect of these control variables on the traveling wave on the stator are investigated instead of contact. Further comparison between amplitude and wave number is then performed in terms of contact and power performance.

5.4.2.1 Experimental results and numerical verification

To investigate the operational characteristics of USM with multiple wave numbers, the overall behaviors of the USM prototype are measured and shown in Figs. 5.20 and 5.21. Simulation is also performed and presented for all cases for comparison purpose. The SC procedure developed and demonstrated in Chapter 4 is adopted in this chapter.

As expected, the shapes of the predicted curves are in agreement with the actual measurements. For example, the variation of the speed-torque curve, that is high speed with low torque while low speed with high torque are exhibited experimentally for all cases shown in Figs. 5.20 and 5.21. However, both speed and output power are slightly over-predicted. For example, the predicted no-load speed of 106 rpm, 38 rpm and 34

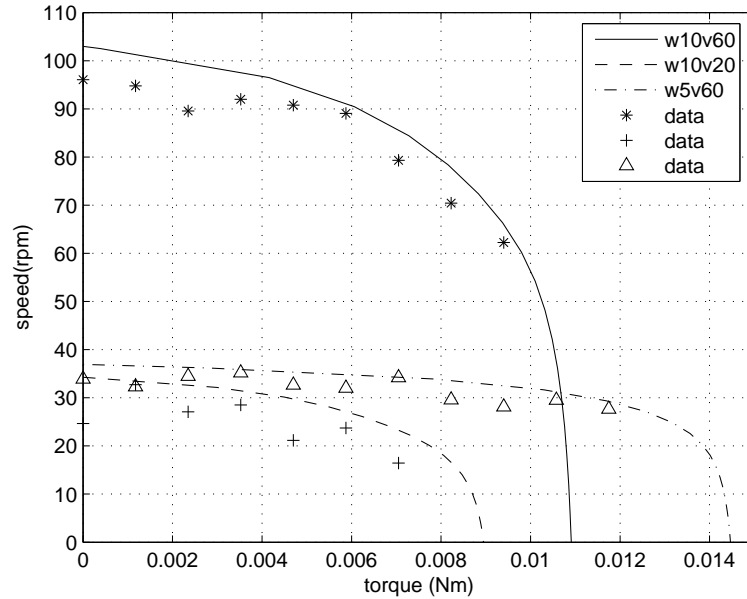


Figure 5.20: Simulated vs. measured speed and torque

rpm are all slightly higher than the measured values of 96 rpm, 35 rpm and 25 rpm, while the predicted maximum output powers are 0.65 W, 0.33 W and 0.18 W, slightly higher than the measured values of 0.59 W, 0.30 W and 0.15 W respectively. A possible explanation for this could be the slight difference in the resonant condition between the actual and the modeled USM. Experimentally, although the driving frequencies are controlled carefully, fully resonant status is harder to achieve, while this is not a problem in simulation. In addition, other environmental variations such as temperature of the mechanical components are not modeled numerically.

5.4.2.2 Comparison of speed control variables

From Eqs. (5.1), (5.4) and (5.6), it can be seen there are three variables - frequency, phase and amplitude of driving signal to be adopted as control variables. Ferreira and Minotti (1998) provided a comparison and comment of these in terms of stator dynamics:

Firstly, because the stator structure is being exploited near mechanical resonance, the vibration amplitude of stator is highly sensitive to the difference between the excitation

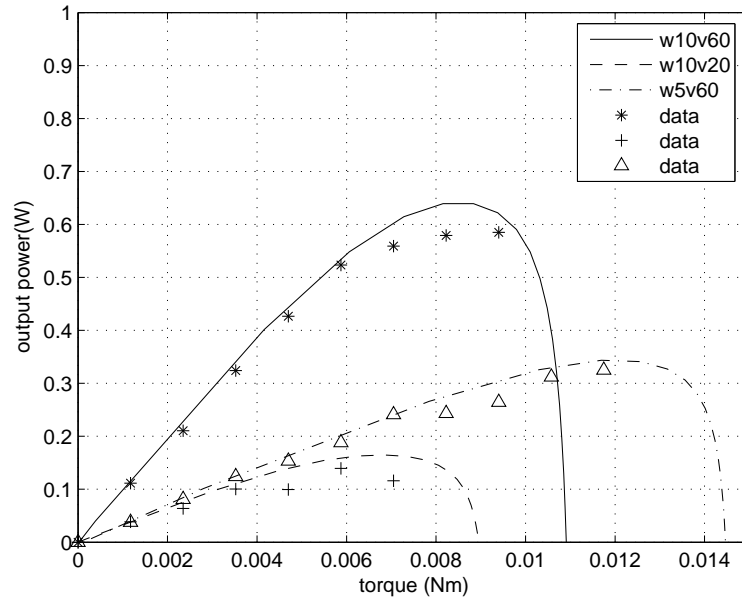


Figure 5.21: Simulated vs. measured output power

frequency and the resonance frequency of the stator. Hence, the variation of the driving signal frequency near the resonance frequency of the stator can be adopted to adjust the speed. However, non-resonant vibration lowers the performance of the USM.

Secondly, the contact points on the surface of stator will move from perfect elliptical motion (phase shift $\pi/2$) to rectilinear reciprocating motion (phase shift 0). Therefore the variation of the driving signals phase shift can also be adopted to adjust the speed. However, phase shifts differing from $\pi/2$ cause the horizontal component of motion to decrease, thereby lowering the performance of the USM.

Thirdly, vibration amplitudes on the contact points of the surface of the stator can be assumed to be linearly dependent on the applied voltages; hence theoretically, rotational speed can be controlled in a linear manner. Amplitude control is better than frequency and phase control due to the perfect elliptical motion and resonant status.

In this chapter, the fourth control variable, wave number is introduced. For example, considering the speed variation of USM for wave number 10 with voltage of 20, and 5 with voltage of 60 shown in Fig. 5.20, the speed differs only slightly for these two cases

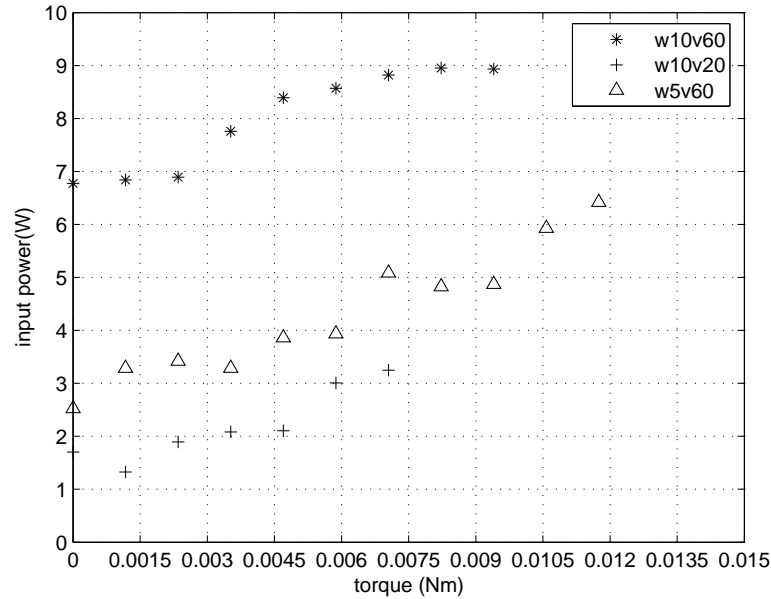


Figure 5.22: Measured input power

in the small torque range. This means that the speed control can be achieved by varying either the voltage or wave number. For example, if the initial operational state is at wave number 10 with voltage of 60 inducing a speed of 106 rpm, by varying either the wave number from 10 to 5, or by varying voltage from 60 to 20, the final speed of approximately 35 rpm can be achieved.

From the above comparison, due to the perfect elliptical motion and resonant status, amplitude and wave number seem to be a better method to achieve speed control. However, their physical backgrounds are different. For amplitude control, variation of the amplitude of external voltage controls the speed of the contact points on the surface of the stator. For wave number control, the resonant frequency is varied to change the speed. Considering the piezoelectric ceramics as the capacitor, its impedance is varied with the frequency of input signal from Eq. (5.12). So mechanically, amplitude control will change the external force, which is similar to active control and susceptible to instability, while wave number control will change the stiffness of the system, which belongs to either passive or semi-active control and has no stability problems. However, control variables voltage and wave number have different mathematical property. The wave

number is non-continuous with large steps while amplitude can be changed continuously. For example, from Table 5.2, if the initial operational state is at wave number 3 with voltage 100, by varying the wave number from 3 to 10, theoretically, the speed of the contact points on the surface of stator can increase to 6 times; while by varying voltage, it is not easy to do because high voltage will cause electrical problems, such as component broken-down. So they may work together in different ranges. For example, the wave number control can vary the speed with large steps while the voltage can do fine control.

Table 5.4: Contact parameters of different cases

Cases	Amplitude (μm)	Axial force (N)	Contact area (mm^2)
Initial status	0	4.1	429/100%
w10v60	2.36	5.5	53/12%
w10v20	0.89	4.6	95/22%
w5v60	5.88	7.6	57/13%

Following the review of the advantages and disadvantages of voltage and wave number control on stator dynamics, their contact performances are compared. From the simulated results listed in Table 5.4, their torque outputs are different. Larger vibration amplitude of stator surface in the case of w5v60 resulted in larger axial force than that of case w10v20. Therefore the case of w5v60 has more torque output despite having smaller contact area. The contact stress in the case of w5v60 should be larger (due to the smaller contact area) than that of case w10v20, the wear will more serious. However, because the peak value of wave crest in the case w5v60 is larger than that of case w10v20, it is more reliable.

Next, the power and efficiency of amplitude and wave number control is examined. Based on measured values as shown in Figs. 5.22, and 5.23, for the case of wave number 10 with voltage of 60, the input power ranged from 7-9 W thus yielding a maximum efficiency of 6.5%. For wave number 10 with voltage of 20, the input power ranged from 3-6 W thus yielding a maximum efficiency of 5.5%. For wave number 5, input power

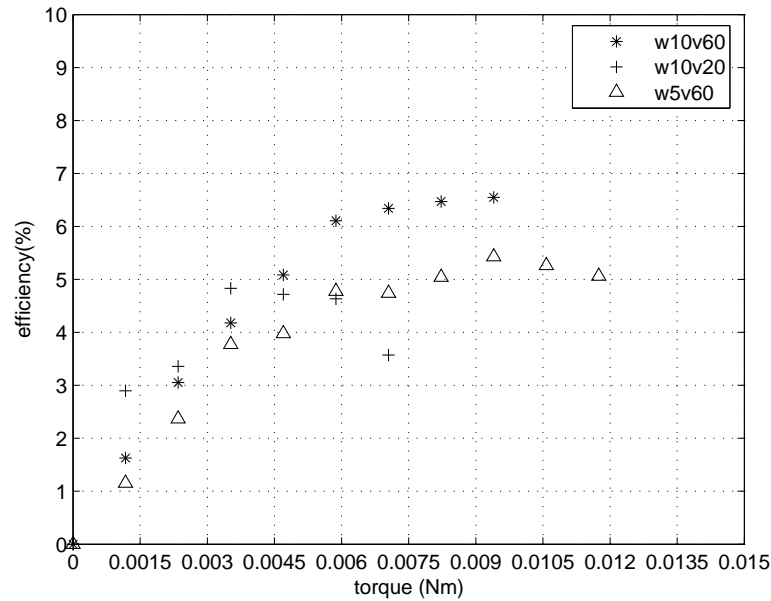


Figure 5.23: Measured efficiency

ranged from 2-3 W thus yielding a maximum efficiency of 5.0%. Comparing the input power and efficiency for different voltages, 60 and 20, as one can see, power consumed by driving electronics increases quickly. However, case w5v60 gives more output power as shown in Fig. 5.21 due to larger torque output over case w10v20. Their efficiencies are similar probably because they all worked at resonant condition as shown in Fig. 5.23. One thing should be noted that the efficiency of the designed USM is unexpectedly low, being $< 7\%$ while most reported works give an efficiency of $> 15\%$ (Cagatay *et al.*, 2003). One of possible reasons is that the drawback of power supply design makes it consume much power because the booster performs all the voltage and current amplification as mentioned in Section 5.1.2.2.

5.5 Conclusions

The design, fabrication and characterization of an USM prototype with multiple wave numbers are performed, in which the wave number has the potential to be the fourth control variable. A number of noteworthy observations are made during the performance

studies. First, the experimental results and predicted values agree well, meaning that the design and fabrication effort including the piezoelectric ring, driving circuit and mechanical parts is successful. Second, the advantages and disadvantages of wave number control and amplitude control are discussed. The speed control range of wave number is larger than that of amplitude control; it is more stable in low speed while amplitude control can work continuously with less wear. Their incorporation may result in better performance of USM. Although the varying wave number concept presented in this chapter is realized in piezoelectric traveling wave USM, the same idea can be used in other piezoelectric device, such as linear USM.

CHAPTER 6

Conclusions and Recommendations

The objective of this research is to study the modeling, design and development of USM. This work is carried out in two parts. The first part (Chapters 3 and 4) is to develop advanced models for the accurate prediction of performance of piezoelectric traveling-wave USM. In the second part (Chapters 2 and 5) improvement upon the typical piezoelectric traveling-wave motor configuration is performed by investigating novel designs of the stator.

6.1 Conclusions

Broadly, the proposed models will be beneficial during the preliminary design stage of USM. Novel USM designs will further expand the application of this kind of piezoelectric actuator. The significant points and findings of this research can be summarized as follows:

- Free vibration characteristics are a prelude to the dynamic analysis of piezoelectric coupled stator, the coupling effect between the piezoelectric layer and the host structure is investigated to show its relationship with the resonant frequencies of

the plate. An analytical model for the free vibration analysis of piezoelectric coupled thin and thick circular plate is presented. The equations are solved using transformation of variables into a second order PDE instead of a sixth order PDE as presented by Liu *et al.* (2002). The displacement assumption follows Kirchhoff plate theory and the improved plate theory (IPT) respectively. A sinusoidal function is adopted to describe the distribution of electric potential along the thickness direction. The Maxwell static electricity equation is included as one of the governing equations. The differential equations of motion are solved for two boundary conditions: clamped edge and simply supported edge and detailed mathematical derivations are presented. Numerical investigations are performed for plates bonded by two piezoelectric layers of various diameter-thickness ratios and the results are verified by the results of three-dimensional finite element analyses using ABAQUS[®]. Results indicate that thicker piezoelectric layer increases the resonant frequencies of the system but the effect is less significant for higher modes and also plates with lower radius to thickness ratio. The analytical solutions and findings provided will be used in the design of USM for practical applications.

- On the potential of designing stator with varying thickness, free vibration analysis of thin annular plate with thickness varying monotonically in arbitrary power form are performed to find the effect of varying thickness on the resonant frequencies of the stator. Transformation of variable is introduced to translate the governing equation for the free vibration of thin annular plate into a fourth-order generalized hypergeometric equation. The analytical solutions in terms of generalized hypergeometric function taking either logarithmic or non-logarithmic forms are proposed. To illustrate the use of the closed form solutions presented, free vibration analyses of a thin annular plate with uniform, linear and nonlinear thickness variation are performed and the results compared with published exact solutions and those from 3D FEM. The results are consistent, indicating that the negative power of thickness

function have greater effect on the frequencies of the plate than positive power. In addition, when the inner radius b increases, the variation of the frequencies of the plate with negative power varying thickness became larger while that of the plate with positive power varying thickness decreases.

- Besides analytical model development, methodologies for analyzing overall behavior of USM are proposed and demonstrated by FE analysis because FE analysis has the advantage of modeling the complicated geometry and boundary conditions. The proposed model yields one of the more complete data sets on simulation of piezoelectric ultrasonic motors in the open literature. Numerical results, such as resonant frequencies and elliptic motion at the surface of stator, steady and transient relationship between axial force, rotor speed and torque, agree with published theoretical, numerical and experimental results. The good correlation between FEM model and experimental results validate to a fairly good extent the proposed procedures for analyzing the overall behavior of USM and also provide good potential as a fairly accurate design tool to minimize the need to resort to extensive physical experimental test of USM.
- The design and fabrication of the piezoelectric traveling-wave USM prototype with multiple wave numbers have been performed. This multiple wave numbers operation is realized by a new electrode configuration of the piezoelectric element. Besides the design of electrodes, drive electronics with four channels compatible with multiple wave numbers operation are also designed, tested and fabricated. The experimental performance results of the multiple wave numbers show that USM with multiple wave numbers significantly outperform the single wave number motor with regard to the range of speed and torque output. This novel implementation of the traveling-wave motor also offers extra control for stable operation of USM. The performance of control variables, wave number and amplitude is compared to show their advantages and disadvantages. The speed control range of wave number is

larger than that of amplitude control; wave number control has better stability at low speed while the amplitude control can work continuously with less wear. Hybrid control using both methods may result in better performance of USM.

6.2 Recommendations for future work

Despite the findings of this dissertation, the study on USM is far from complete. Rather the experience reinforce that innovations on USM is still an emerging area to explore with promising future once other practical issues are addressed. Some recommendations for future work are listed as below:

- Analytical
 - (a) **Model of USM with non-uniform stator:** in the design of an USM, one essential factor is to determine the point of application of the frictional force to effect rotation of the rotor. The best point is considered as that of maximum displacement under bending vibration, because high rotational speed of rotor is obtained. This location is affected by the geometrical shape of the stator. If the stator is of non-uniform thickness, then the distribution of the thickness can affect the location of maximum displacement. In this dissertation, the analytical model to study free vibration of annular thin plate with varying thickness has been proposed. As the next logical step, the forced vibration, i.e. the dynamics of stator with varying thickness can be investigated. The technical challenge will be to design and build the contact model between rotor and stator with varying thickness and adequate stiffness to achieve an optimal bending profile of the stator.
 - (b) **Model of USM accounting for full piezoelectric coupled interaction:** in modeling USM, the coupling effect between the piezoelectric layer and the host structure is important to obtain accurate prediction. In this dissertation,

the analytical model to study free vibration of laminated annular thin and thick plate taking into account piezoelectric coupling effect has been proposed. In the second step, the forced vibration i.e. the dynamics of stator with laminated layer considering piezoelectric effect can be studied. The analytical model of free vibration presented in this dissertation is based on 2-dimensional theory and the extension to the hand the geometry of the stator teeth and boundary support pose a challenge.

- FE analysis

Develop of time integration scheme: as mentioned in Chapter 4, Eq. (4.36) can be solved using numerical time integration method, which can be either implicit or explicit. The mass-less property of electrical potential ϕ implies that the fundamental period is zero leading to instability of the explicit method. In applying the implicit scheme in the case of USM, intermittent contact and stick/slip frictional sliding will result in the tangent coefficient matrix being not sufficiently smooth or the predicted intermediate state being too far from the actual solution, giving rise to convergence problem. It therefore appears that new solution procedure can be developed for the two different time integration routines for different segments of the USM. Specifically, the explicit time integration using the conditionally stable central difference method is employed to obtain the contact response and the implicit unconditionally stable time integration method (such as Newmark's method) is used to solve for the piezoelectric patch dynamics. However, such hybrid method raised other problems, such as the choice of finite difference methods and the coupling of the methods.

- Experimental

-
- (a) **Design of USM with more wave numbers:** in the Section 5.1.1, a piezoelectric electrode configuration with 8 different wave numbers are presented. However, given the available machinability and limitation of time, the USM prototype with only two wave numbers, wave number 5 and 10 are experimentally realized in this dissertation. Further design and fabrication of USM prototype with more wave numbers are expected to provide more insight on the practical performance of USM with multiple wave numbers. The main obstacle is probably the choice of the geometry and size of stator and the segmentation of the piezoelectric electrode.
- (b) **Design of control algorithm:** in this dissertation, an USM prototype with multiple wave numbers are fabricated, the advantages and disadvantages of control variables, wave number and amplitude are discussed. The research finds that hybrid control employing both variables may result in better performance of USM. Although in concept this may be simple, practical realization of hybrid control algorithm combining wave number and amplitude is an experimental challenge. It is envisaged that the results of such research may open new concepts, designs and applications bringing to birth yet further interesting challenges.

References

- ABAQUS. ABAQUS Version 6.4 Documentation. 2003.
- Airey, J. The vibration of circular plates and their relation to Bessel functions, Proceedings in the Physical Society, London. 23225-232. 1911.
- Allik, H. and T.J.R. Hughes. Finite element method for piezoelectric vibration, Int. J. Numer. Methods Eng. 2(2): p. 151-157. 1970.
- Aoyagi, M., Y. Nakano, and Y. Tomikawa. Rod-type ultrasonic motor using 2 degenerate 2nd flexural vibration modes and characteristic consideration using its equivalent-circuit expression, Jpn. J. Appl. Phys. Part 1 - Regul. Pap. Short Notes Rev. Pap. 34(9B): p. 5292-5297. 1995.
- Aoyagi, M., F. Suzuki, Y. Tomikawa and I. Kano. High-speed thin ultrasonic spindle motor and its application, Jpn. J. Appl. Phys. Part 1 - Regul. Pap. Short Notes Rev. Pap. 43(5B): p. 2873-2878. 2004.
- Aoyagi, M. and Y. Tomikawa. Ultrasonic rotary motor using longitudinal and bending multimode vibrator with mode-coupling caused by external additional asymmetry, Jpn. J. Appl. Phys. Part 1 - Regul. Pap. Short Notes Rev. Pap. 32(9B): p. 4190-4193. 1993.
- Aoyagi, M. and Y. Tomikawa. Improvement in performance of longitudinal and torsional vibrator combination-type ultrasonic motor, Jpn. J. Appl. Phys. Part 1 - Regul. Pap. Short Notes Rev. Pap. 38(5B): p. 3342-3346. 1999.
- Aoyagi, M., Y. Tomikawa, and T. Takano. Ultrasonic motors using longitudinal and bending multimode vibrators with mode-coupling by externally additional asymmetry or internal nonlinearity, Jpn. J. Appl. Phys. Part 1 - Regul. Pap. Short Notes Rev. Pap. 31(9B): p. 3077-3080. 1992.
- Aoyagi, M., Y. Tomikawa, and T. Takano. Simplified equivalent circuit of an ultrasonic motor and its applications, Ultrasonics. 34(2-5): p. 275-278. 1996.
- Aoyagi, M., S. Tsuchiya, and Y. Tomikawa. Trial production of an ultrasonic motor using longitudinal and torsional vibrations of a rod vibrator driven by piezo-ceramic plates inserted in its axial direction, Jpn. J. Appl. Phys. Part 1 - Regul. Pap. Short Notes Rev. Pap. 36(9B): p. 6106-6109. 1997.
- Apex Microtechnology Corporation, Application note 19: stability for power operational amplifiers. <http://www.apexmicrotech.com/>
- Apex Microtechnology Corporation, Application note 25: driving capacitive loads. <http://www.apexmicrotech.com/>

- Apex Microtechnology Corporation, PB58 datasheet. <http://www.apexmicrotech.com/>
- Ayari, M.L. and V.E. Saouma. Static and Dynamic Contact Impact Problems Using Fictitious Forces, *Int. J. Numer. Methods Eng.* 32(3): p. 623-643. 1991.
- Bai, D. Z., T. Ishii, K. Nakamura, S. Ueha, T. Yonezawa and T. Takahashi. An ultrasonic motor driven by the phase-velocity difference between two traveling waves, *IEEE Trans. Ultrason. Ferroelectr. Freq. Control.* 51(6): p. 680-685. 2004.
- Bailey, T., J.E. Hubbard. Distributed piezoelectric-polymer active vibration control of a cantilever beam (flexible spacecraft structures), *J. Guid. Control Dyn.* 8(5): p. 605-611. 1985.
- Bal, G. and E. Bekiroglu. A PWM technique for DSP controlled ultrasonic motor drive system, *Electr. Power Compon. Syst.* 33(1): p. 21-38. 2005.
- Bambill, D.V., J.A. Reyes, and P.A.A. Laura. A note on transverse axisymmetric vibrations of annular plates of non-uniform thickness, *J. Sound Vibr.* 191(4): p. 584-589. 1996.
- Barth, H.V. Ultrasonic driven motor, *IBM Tech. Disclosure Bull.* 162263. 1973.
- Bathe, K.-J. Finite element procedures. pp.xiv, 1037 p., Englewood Cliffs, N.J.: Prentice Hall. 1996.
- Bathe, K.-J. and A.B. Chaudhary. A solution method for planar and axisymmetric contact problems, *Int. J. Numer. Methods Eng.* 21:65-88. 1985.
- Bathe, K.-J. and V. Sonnad. On effective implicit time integration in analysis of fluid-structure problems, *Int. J. Numer. Methods Eng.* 15(6): p. 943-948. 1980.
- Bekiroglu, E. and N. Daldal. Remote control of an ultrasonic motor by using a GSM mobile phone, *Sens. Actuator A-Phys.* 120(2): p. 536-542. 2005.
- Belytschko, T., H.-J. Yen, and R. Mullen. Mixed methods for time integration, *Comput. Meth. Appl. Mech. Eng.* 17-18(Part 2): p. 259-275. 1979.
- Bexell, M. and S. Johansson. Fabrication and evaluation of a piezoelectric miniature motor, *Sens. Actuator A-Phys.* 75(1): p. 8-16. 1999.
- Biwersi, S., P. Gaucher, J. Hector, J. F. Manceau and F. Bastien. Production of a quasi-travelling wave in silicon membranes with a thin deposited layer of sol-gel PZT, *Sens. Actuator A-Phys.* 70(3): p. 291-295. 1998.
- Cagatay, S., B. Koc, P. Moses and K. Uchino. A piezoelectric micromotor with a stator of $\phi=1.6$ mm and $l=4$ mm using bulk PZT, *Jpn. J. Appl. Phys. Part 1 - Regul. Pap. Short Notes Rev. Pap.* 43(4A): p. 1429-1433. 2004.
- Cagatay, S., B. Koc, and K. Uchino. A 1.6-mm, metal tube ultrasonic motor, *IEEE Trans. Ultrason. Ferroelectr. Freq. Control.* 50(7): p. 782-786. 2003.
- Carotenuto, A., N. Lamberti, A. Iula and M. Pappalardo. A new low voltage piezoelectric micromotor based on stator precessional motion, *IEEE Trans. Ultrason. Ferroelectr. Freq. Control.* 45(5): p. 1427-1435. 1998.

- Carotenuto, R., G. Caliano, A. Iula and M. Pappalardo. Langevin flexural piezoelectric motor based on stator precessional motion, *Sens. Actuator A-Phys.* 113(2): p. 189-197. 2004.
- Carrington, H. The frequencies of vibration of flat circular plates fixed at the circumference, *Philos. Mag.* 50126ff. 1925.
- Chau, K.T. and S.W. Chung. Servo position control of ultrasonic motors using fuzzy neural network, *Electr. Power Compon. Syst.* 29(3): p. 229-246. 2001.
- Chau, K.T., S.W. Chung, and C.C. Chan. Neuro-fuzzy speed tracking control of traveling-wave ultrasonic motor drives using direct pulsewidth modulation, *IEEE Trans. Ind. Appl.* 39(4): p. 1061-1069. 2003.
- Chen, J.S. and I.D. Lin. Toward the implementation of an ultrasonic motor servo drive using FPGA, *Mechatronics.* 12(4): p. 511-524. 2002.
- Chen, W.Q. Coupled free vibrations of spherically isotropic hollow spheres. Ph.D Thesis. 1996.
- Chu, X. C., R. B. Yan, L. Yan and L. T. Li. A quantitative circuit model of the stator of piezoelectric ultrasonic motor. pp.135-138, Zurich-Uetikon: TRANS TECH PUBLICATIONS LTD. 2002.
- Conway, H.D., E.C.H. Becker, and J.F. Dubil. Vibration frequencies of tapered bars and circular plates, *J. Appl. Mech.-Trans. ASME.* 31329-331. 1964.
- Cote, F., P. Masson, N. Mrad and V. Cotoni. Dynamic and static modelling of piezoelectric composite structures using a thermal analogy with MSC/NASTRAN, *Compos. Struct.* 65(3-4): p. 471-484. 2004.
- Ding, H.J., Chenbuo, and Liangjian. General solutions for coupled equations for piezoelectric media, *Int. J. Solids Struct.* 33(16): p. 2283-2298. 1996.
- Dong, S. X., S. Cagatay, K. Uchino and D. Viehland. A 'center-wobbling' ultrasonic rotary motor using a metal tube-piezoelectric plate composite stator, *J. Intell. Mater. Syst. Struct.* 13(11): p. 749-755. 2002.
- Dong, S. X., S. P. Lim, K. H. Lee, J. D. Zhang, L. C. Lim and K. Uchino. Piezoelectric ultrasonic micromotor with 1.5 mm diameter, *IEEE Trans. Ultrason. Ferroelectr. Freq. Control.* 50(4): p. 361-367. 2003.
- Dong, S. X., S. X. Wang, W. J. Shen and L. T. Li. A miniature piezoelectric ultrasonic motor based on circular bending vibration mode, *IEEE-ASME Trans. Mechatron.* 5(4): p. 325-330. 2000.
- Dong, S. X., J. D. Zhang, H. W. Kim, M. T. Strauss, K. Uchino and D. Viehland. Flexural traveling wave excitation based on shear-shear mode, *IEEE Trans. Ultrason. Ferroelectr. Freq. Control.* 51(10): p. 1240-1246. 2004.
- Dubois, M.A. and P. Muralt. PZT thin film actuated elastic fin micromotor, *IEEE Trans. Ultrason. Ferroelectr. Freq. Control.* 45(5): p. 1169-1177. 1998.
- Eterovic, A.L. and K.J. Bathe. On the Treatment of Inequality Constraints Arising from Contact Conditions in Finite-Element Analysis, *Comput. Struct.* 40(2): p. 203-209. 1991.

- Evans, K.E. and K.L. Alderson. The Static and Dynamic Moduli of Auxetic Microporous Polyethylene, *J. Mater. Sci. Lett.* 11(24): p. 1721-1724. 1992.
- Ewins, D.J. *Modal testing : theory, practice, and application.* pp.xiii, 562 p., Baldock, Hertfordshire, England ; Philadelphia, PA: Research Studies Press. 2000.
- Ferreira, A. and P. Minotti. High-performance load-adaptive speed control for ultrasonic motors, *Control Eng. Practice.* 6(1): p. 1-13. 1998.
- Fleischer, M., D. Stein, and H. Meixner. New type of piezoelectric ultrasonic motor, *IEEE Trans. Ultrason. Ferroelectr. Freq. Control.* 36(6): p. 614-619. 1989.
- Fleischer, M., D. Stein, and H. Meixner. Novel ultrasonic motors with monomodal and bimodal drives, *Sens. Actuator A-Phys.* 21(1-3): p. 357-361. 1990.
- Flynn, A.M. Piezoelectric ultrasonic micromotors. Thesis Ph. D. –Massachusetts Institute of Technology Dept. of Electrical Engineering and Computer Science 1995. 1995.
- Flynn, A. M., L. S. Tavrow, S. F. Bart, R. A. Brooks, D. J. Ehrlich, K. R. Udayakumar and L. E. Cross. Piezoelectric micromotors for microrobots, *J. Microelectromech. Syst.* 1(1): p. 44-51. 1992.
- Friend, J., K. Nakamura, and S. Ueha. A piezoelectric micromotor using in-plane shearing of PZT elements, *IEEE-ASME Trans. Mechatron.* 9(3): p. 467-473. 2004.
- Friend, J.R. and D.S. Stutts. The dynamics of an annular piezoelectric motor stator, *J. Sound Vibr.* 204(3): p. 421-437. 1997.
- Gaudenzi, P. and K.J. Bathe. An Iterative Finite-Element Procedure for the Analysis of Piezoelectric Continua, *J. Intell. Mater. Syst. Struct.* 6(2): p. 266-273. 1995.
- Giraud, F., B. Semail, and J.T. Audren. Analysis and phase control of a piezoelectric traveling-wave ultrasonic motor for haptic stick application, *IEEE Trans. Ind. Appl.* 40(6): p. 1541-1549. 2004.
- Glenn, T.S. Mixed-domain performance model of the piezoelectric traveling-wave motor and the development of a two-sided device. Thesis Ph. D. –Massachusetts Institute of Technology Dept. of Aeronautics and Astronautics. 2002.
- Hagedorn, P. and J. Wallaschek. Traveling-Wave Ultrasonic Motors, .1. Working Principle and Mathematical-Modeling of the Stator, *J. Sound Vibr.* 155(1): p. 31-46. 1992.
- Hagedorn, P., J. Wallaschek, and W. Konrad. Traveling-Wave Ultrasonic Motors, .2. A Numerical-Method for the Flexural Vibrations of the Stator, *J. Sound Vibr.* 168(1): p. 115-122. 1993.
- Hagood, N.W. and A.J. McFarland. Modeling of a Piezoelectric Rotary Ultrasonic Motor, *IEEE Trans. Ultrason. Ferroelectr. Freq. Control.* 42(2): p. 210-224. 1995.
- Han, J.H. and I. Lee. Analysis of composite plates with piezoelectric actuators for vibration control using layerwise displacement theory, *Compos. Pt. B-Eng.* 29(5): p. 621-632. 1998.
- Hanagud, S., M.W. Obal, and A.J. Calise. Optimal Vibration Control by the Use of Piezoceramic Sensors and Actuators, *J. Guid. Control Dyn.* 15(5): p. 1199-1206. 1992.

- He, J. and Z.-F. Fu. Modal analysis. pp.xiii, 291 p., Oxford ; Boston: Butterworth-Heinemann. 2001.
- Hirata, H. and S. Ueha. Characteristics Estimation of a Traveling-Wave Type Ultrasonic Motor, *IEEE Trans. Ultrason. Ferroelectr. Freq. Control.* 40(4): p. 402-406. 1993.
- Hirata, H. and S. Ueha. Design of a Traveling-Wave Type Ultrasonic Motor, *IEEE Trans. Ultrason. Ferroelectr. Freq. Control.* 42(2): p. 225-231. 1995.
- Hosoe, K. An Ultrasonic Motor Used in Autofocus Lens Assemblies, *Techno.* 36-41 (in Japanese). 1989.
- Hughes, T. J. R., R. L. Taylor, J. L. Sackman, A. Curnier and W. Kanoknukulchai. A finite element method for a class of contact-impact problems, *Comput. Meth. Appl. Mech. Eng.* 8(3): p. 249-276. 1976.
- Iijima, T., Y. Nakagawa, and H. Ito. Ultrasonic flat motor using coupling of longitudinal and flexural vibration modes, *Jpn. J. Appl. Phys. Part 1 - Regul. Pap. Short Notes Rev. Pap.* 31(8): p. 2598-2605. 1992.
- Iijima, T., K. Sano, Y. Nakagawa and H. Ito. Rotary ultrasonic motor using symmetrical contour vibration of rectangular plate, *Jpn. J. Appl. Phys. Part 1 - Regul. Pap. Short Notes Rev. Pap.* 32(5B): p. 2402-2404. 1993.
- Ikeda, T.D. Fundamentals of piezoelectricity. pp.xi, 263 p., Oxford ; New York: Oxford University Press. 1990.
- Inman, D.J. Engineering vibration. pp.xv, 560 p., Englewood Cliffs, N.J.: Prentice Hall. 1994.
- Izuno, Y., T. Izumi, H. Yasutsune, E. Hiraki and M. Nakaoka. Speed tracking servo control system incorporating traveling-wave-type ultrasonic motor and feasible evaluations, *IEEE Trans. Ind. Appl.* 34(1): p. 126-132. 1998.
- Izuno, Y., R. Takeda, and M. Nakaoka. New Fuzzy Reasoning-Based High-Performance Speed Position Servo Control Schemes Incorporating Ultrasonic Motor, *IEEE Trans. Ind. Appl.* 28(3): p. 613-618. 1992.
- Juang, P.A. and H.J. Hardtke. A new disc-type ultrasonic motor, *Sens. Actuator A-Phys.* 94(1-2): p. 102-111. 2001.
- Kagawa, Y., T. Tsuchiya, T. Kataoka, T. Yamabuchi and T. Furukawa. Finite element simulation of dynamic responses of piezoelectric actuators, *J. Sound Vibr.* 191(4): p. 519-538. 1996.
- Kawai, Y., K. Asai, S. Naito, T. Fukui, Y. Adachi, N. Handa, K. Ikeda and K. Tsuda. High-power traveling-wave type ultrasonic motor, *Jpn. J. Appl. Phys. Part 1 - Regul. Pap. Short Notes Rev. Pap.* 34(5B): p. 2711-2714. 1995.
- Kim, J., V.V. Varadan, and V.K. Varadan. Finite element modelling of structures including piezoelectric active devices, *Int. J. Numer. Methods Eng.* 40(5): p. 817-832. 1997.
- Koc, B., P. Bouchilloux, and K. Uchino. Piezoelectric micromotor using a metal-ceramic composite structure, *IEEE Trans. Ultrason. Ferroelectr. Freq. Control.* 47(4): p. 836-843. 2000.

- Koc, B., S. Cagatay, and K. Uchino. A piezoelectric motor using two orthogonal bending modes of a hollow cylinder, *IEEE Trans. Ultrason. Ferroelectr. Freq. Control.* 49(4): p. 495-500. 2002.
- Koc, B., A. Dogan, Y. Xu, R. E. Newnham and K. Uchino. An ultrasonic motor using a metal-ceramic composite actuator generating torsional displacement, *Jpn. J. Appl. Phys. Part 1 - Regul. Pap. Short Notes Rev. Pap.* 37(10): p. 5659-5662. 1998.
- Kumada, A. A piezoelectric ultrasonic motor, *Jpn. J. Appl. Phys. Supplement.* 24(24-2): p. 739-741. 1985.
- Kurosawa, M., H. Inagaki, and T. Higuchi. Investigation of stator transducer for a column-shaped ultrasonic motor, *Ultrasonics.* 34(2-5): p. 271-274. 1996.
- Kurosawa, M., K. Nakamura, T. Okamoto and S. Ueha. An ultrasonic motor using bending vibrations of a short cylinder, *IEEE Trans. Ultrason. Ferroelectr. Freq. Control.* 36(5): p. 517-521. 1989.
- Kurosawa, M. and S. Ueha. Hybrid transducer type ultrasonic motor, *IEEE Trans. Ultrason. Ferroelectr. Freq. Control.* 38(2): p. 89-92. 1991.
- Lamberti, N., A. Iula, and M. Pappalardo. A piezoelectric motor using flexural vibration of a thin piezoelectric membrane, *IEEE Trans. Ultrason. Ferroelectr. Freq. Control.* 45(1): p. 23-29. 1998.
- Landis, C.M. A new finite-element formulation for electromechanical boundary value problems, *Int. J. Numer. Methods Eng.* 55(5): p. 613-628. 2002.
- Le Moal, P. and P. Cusin. Optimization of travelling wave ultrasonic motors using a three-dimensional analysis of the contact mechanism at the stator-rotor interface, *Eur. J. Mech. A-Solids.* 18(6): p. 1061-1084. 1999.
- Lebrun, L., P. Gonnard, and M. Guinet. A low-cost piezoelectric motor using a (1,1) non-axisymmetric mode, *Smart Mater. Struct.* 8(4): p. 469-475. 1999.
- Lebrun, L., L. Petit, and P. Gonnard. Piezoelectric motor using a (1,1) non-axisymmetric mode, *Ultrasonics.* 34(2-5): p. 251-255. 1996.
- Lee, C.K., S.H. Chang, and P.Z. Chang. Miniature piezoelectric actuators: design concept, fabrication and performance evaluation, *Smart Mater. Struct.* 7(3): p. 312-326. 1998.
- Lee, C.K. and F.C. Moon. Modal Sensors Actuators, *J. Appl. Mech.-Trans. ASME.* 57(2): p. 434-441. 1990.
- Leinvuo, J.T., S.A. Wilson, and R.W. Whatmore. Flexensional ultrasonic motor using the contour mode of a square piezoelectric plate, *IEEE Trans. Ultrason. Ferroelectr. Freq. Control.* 51(8): p. 929-936. 2004.
- Leissa, A.W. *Vibration of plates.* pp.vii, 353 p., Washington: Scientific and Technical Information Division, National Aeronautics and Space Administration. 1969.
- Leissa, A.W. Recent research in plate vibrations: classical theory, *Shock and Vibration Digest.* 9(10): p. 13-24. 1977.

- Leissa, A.W. Recent research in plate vibrations. 1973-1976: complicating effects, *Shock and Vibration Digest*. 10(12): p. 21-35. 1978.
- Leissa, A.W. Plate vibrations research, 1976-80: classical theory, *Shock and Vibration Digest*. 13(9): p. 11-22. 1981.
- Leissa, A.W. Plate vibrations research, 1976-80: complicating effects, *Shock and Vibration Digest*. 13(10): p. 19-36. 1981.
- Leissa, A.W. Recent research in plate vibrations: 1981-85. PART I. classical theory, *Shock and Vibration Digest*. 19(2): p. 11-18. 1987.
- Leissa, A.W. Recent research in plate vibrations: 1981-85. PART II. COMPLICATING EFFECTS, *Shock and Vibration Digest*. 19(3): p. 10-24. 1987.
- Lenox, T.A. and H.D. Conway. An exact, closed form, solution for the flexural vibration of a thin annular plate having a parabolic thickness variation, *J. Sound Vibr.* 68(2): p. 231-239. 1980.
- Lerch, R. Simulation of Piezoelectric Devices by 2-Dimensional and 3-Dimensional Finite-Elements, *IEEE Trans. Ultrason. Ferroelectr. Freq. Control*. 37(3): p. 233-247. 1990.
- Lin, F.J., R.J. Wai, and R.Y. Duan. Fuzzy neural networks for identification and control of ultrasonic motor drive with LLC resonant technique, *IEEE Trans. Ind. Electron.* 46(5): p. 999-1011. 1999.
- Lin, F.J., R.J. Wai, and C.M. Hong. Recurrent neural network control for LCC-resonant ultrasonic motor drive, *IEEE Trans. Ultrason. Ferroelectr. Freq. Control*. 47(3): p. 737-749. 2000.
- Lin, F.J., R.J. Wai, and C.M. Hong. Identification and control of rotary traveling-wave type ultrasonic motor using neural networks, *IEEE Trans. Control Syst. Technol.* 9(4): p. 672-680. 2001.
- Liu, X., Q. Wang, and S.T. Quek. Analytical solution for free vibration of piezoelectric coupled moderately thick circular plates, *Int. J. Solids Struct.* 39(8): p. 2129-2151. 2002.
- Lu, F., H.P. Lee, and S.P. Lim. Contact modeling of viscoelastic friction layer of traveling wave ultrasonic motors, *Smart Mater. Struct.* 10(2): p. 314-320. 2001.
- Lu, F., H.P. Lee, and S.P. Lim. Modeling of contact with projections on rotor surfaces for ultrasonic traveling wave motors, *Smart Mater. Struct.* 10(5): p. 860-866. 2001.
- Macrobert, T.M. Evaluation of an E-Function when three of its upper parameters differ by integral values, *Pac. J. Math.* 12999-1002. 1962.
- Maeno, T., T. Tsukimoto, and A. Miyake. Finite-Element Analysis of the Rotor Stator Contact in a Ring-Type Ultrasonic Motor, *IEEE Trans. Ultrason. Ferroelectr. Freq. Control*. 39(6): p. 668-674. 1992.
- Maia, N.M.M. and J.M. Montalvão e Silva. Theoretical and experimental modal analysis. pp.xvii, 468 p., Taunton, Somerset, England, New York: Research Studies Press ;Wiley. 1997.

- Manceau, J.F. and F. Bastien. Production of a Quasi-Traveling Wave in a Silicon Rectangular Plate Using Single-Phase Drive, *IEEE Trans. Ultrason. Ferroelectr. Freq. Control.* 42(1): p. 59-65. 1995.
- Manceau, J.F., S. Biwersi, and F. Bastien. On the generation and identification of traveling waves in non-circular structures - application to innovative piezoelectric motors, *Smart Mater. Struct.* 7(3): p. 337-344. 1998.
- Mason, W.P. *Electromechanical transducers and wave filters.* pp.xii, 333 p., New York,: D. Van Nostrand company, inc. 1942.
- Mason, W.P. *Physical acoustics and the properties of solids.* pp.402 p., Princeton, N.J.,: Van Nostrand. 1958.
- Matthies, H. and G. Strang. The solution of nonlinear finite element equations, *Int. J. Numer. Methods Eng.* 141613-1626. 1979.
- Maxim Integrated Products, Inc., MAX038 datasheet. <http://www.maxim-ic.com>
- Mindlin, R.D. Influence of rotary inertia and shear on flexural motions of isotropic, elastic plates, *J. Appl. Mech.-Trans. ASME.* 1831-38. 1951.
- Mindlin, R.D. and H.D. Medick. Extensional vibrations of elastic plates, *J. Appl. Mech.-Trans. ASME.* 26561-569. 1959.
- Ming, Y. and P.W. Que. Performances estimation of a rotary traveling wave ultrasonic motor based on two-dimension analytical model, *Ultrasonics.* 39(2): p. 115-120. 2001.
- Morita, T. Miniature piezoelectric motors, *Sens. Actuator A-Phys.* 103(3): p. 291-300. 2003.
- Morita, T., M. Kurosawa, and T. Higuchi. An ultrasonic micromotor using a bending cylindrical transducer based on pzt thin film, *Sens. Actuator A-Phys.* 50(1-2): p. 75-80. 1995.
- Morita, T., M. Kurosawa, and T. Higuchi. Design of a cylindrical ultrasonic micromotor to obtain mechanical output, *Jpn. J. Appl. Phys. Part 1 - Regul. Pap. Short Notes Rev. Pap.* 35(5B): p. 3251-3254. 1996.
- Morita, T., M.K. Kurosawa, and T. Higuchi. A cylindrical micro ultrasonic motor using PZT thin film deposited by single process hydrothermal method (ϕ 2.4 mm, L = 10 mm stator transducer), *IEEE Trans. Ultrason. Ferroelectr. Freq. Control.* 45(5): p. 1178-1187. 1998.
- Morita, T., M.K. Kurosawa, and T. Higuchi. Cylindrical micro ultrasonic motor utilizing bulk lead zirconate titanate (PZT), *Jpn. J. Appl. Phys. Part 1 - Regul. Pap. Short Notes Rev. Pap.* 38(5B): p. 3347-3350. 1999.
- Morita, T., M.K. Kurosawa, and T. Higuchi. A cylindrical shaped micro ultrasonic motor utilizing PZT thin film (1.4 mm in diameter and 5.0 mm long stator transducer), *Sens. Actuator A-Phys.* 83(1-3): p. 225-230. 2000.
- Muralt, P. Ultrasonic micromotors based on PZT thin films, *J. Electroceram.* 3(2): p. 143-150. 1999.

- Muralt, P., M. Kohli, T. Maeder, A. Kholkin, K. Brooks, N. Setter and R. Luthier. Fabrication and characterization of pzt thin-film vibrators for micromotors, *Sens. Actuator A-Phys.* 48(2): p. 157-165. 1995.
- Na, S. and L. Librescu. Oscillation control of cantilevers via smart materials technology and optimal feedback control: actuator location and power consumption issues, *Smart Mater. Struct.* 7(6): p. 833-842. 1998.
- Ohnishi, O., O. Myohga, T. Uchikawa, M. Tamegai, T. Inoue and S. Takahashi. Piezoelectric ultrasonic motor using longitudinal torsional composite resonance vibration, *IEEE Trans. Ultrason. Ferroelectr. Freq. Control.* 40(6): p. 687-693. 1993.
- Petit, L., R. Briot, L. Lebrun and P. Gonnard. A piezomotor using longitudinal actuators, *IEEE Trans. Ultrason. Ferroelectr. Freq. Control.* 45(2): p. 277-284. 1998.
- Pochhammer, L. Ueber die Differentialgleichung der allgemeineren hypergeometrischen Reihe mit zwei endlichen singularen Punkten, *J. Reine Angew. Math.* 10276-159. 1888.
- Pons, J. L., H. Rodriguez, R. Ceres and L. Calderon. Novel modeling technique for the stator of traveling wave ultrasonic motors, *IEEE Trans. Ultrason. Ferroelectr. Freq. Control.* 50(11): p. 1429-1435. 2003.
- Pons, J. L., H. Rodriguez, E. Rocon, J. F. Fernandez and M. Villegas. Practical consideration of shear strain correction factor and Rayleigh damping in models of piezoelectric transducers, *Sens. Actuator A-Phys.* 115(2-3): p. 202-208. 2004.
- Pons, J. L., H. Rodriguez, F. Seco, R. Ceres and L. Calderon. Modelling of piezoelectric transducers applied to piezoelectric motors: a comparative study and new perspective, *Sens. Actuator A-Phys.* 110(1-3): p. 336-343. 2004.
- Racine, G.A., P. Muralt, and M.A. Dubois. Flexural-standing-wave elastic force motor using ZnO and PZT thin film on micromachined silicon membranes for wristwatch applications, *Smart Mater. Struct.* 7(3): p. 404-416. 1998.
- Rainville, E.D. *Special functions*. New York: The Macmillan Company pp 73. 1960.
- Rayleigh, J.W.S. and R.B. Lindsay. *The theory of sound*. pp.2 v. in 1., New York,: Dover Publications. 1945.
- Rayner, P.J. and R.W. Whatmore. Travelling wave ultrasonic motor using the B-08 flexural mode of a circular membrane, *IEEE Trans. Ultrason. Ferroelectr. Freq. Control.* 48(3): p. 683-690. 2001.
- Romanelli, E. and P.A.A. Laura. An approximate method for analyzing transverse vibrations of circular, annular plates of non-uniform thickness and a free inner boundary, *Comput. Struct.* 62(4): p. 795-797. 1997.
- Saigoh, H., M. Kawasaki, N. Maruko and K. Kanayama. Multilayer piezoelectric motor using the first longitudinal and the 2nd bending vibrations, *Jpn. J. Appl. Phys. Part 1 - Regul. Pap. Short Notes Rev. Pap.* 34(5B): p. 2760-2764. 1995.
- Sashida, T. *Japanese Patent Disclosure*. 58 148682. 1983.
- Sashida, T. and T. Kenjo. *An introduction to ultrasonic motors*. pp.xi, 242 p., Oxford ; New York: Clarendon Press. 1993.

- Sato, K., M. Aoyagi, T. Ogasawara and Y. Tomikawa. Ultrasonic motor using a large-diameter torsional vibrator with slant slits, *Jpn. J. Appl. Phys. Part 1 - Regul. Pap. Short Notes Rev. Pap.* 34(5B): p. 2707-2710. 1995.
- Satonobu, J., M. Fukami, and N. Nakagawa. Traveling wave ultrasonic motor using a flexural composite transducer, *Jpn. J. Appl. Phys. Part 1 - Regul. Pap. Short Notes Rev. Pap.* 42(5B): p. 3007-3011. 2003.
- Satonobu, J., D. Lee, K. Nakamura and S. Ueha. Improvement of the longitudinal vibration system for the hybrid transducer ultrasonic motor, *IEEE Trans. Ultrason. Ferroelectr. Freq. Control.* 47(1): p. 216-221. 2000.
- Satonobu, J., N. Torii, K. Nakamura and S. Ueha. Construction of megatorque hybrid transducer type ultrasonic motor, *Jpn. J. Appl. Phys. Part 1 - Regul. Pap. Short Notes Rev. Pap.* 35(9B): p. 5038-5041. 1996.
- Scarpa, F. and G. Tomlinson. Theoretical characteristics of the vibration of sandwich plates with in-plane negative Poisson's ratio values, *J. Sound Vibr.* 230(1): p. 45-67. 2000.
- Senjyu, T., T. Kashiwagi, and K. Uezato. Position control of ultrasonic motors using MRAC with dead-zone compensation, *IEEE Trans. Ind. Electron.* 48(6): p. 1278-1285. 2001.
- Senjyu, T., T. Kashiwagi, and K. Uezato. Position control of ultrasonic motors using MRAC and dead-zone compensation with fuzzy inference, *IEEE Trans. Power Electron.* 17(2): p. 265-272. 2002.
- Senjyu, T., H. Miyazato, and K. Uezato. Quick and precise position control of an ultrasonic motor with dual mode control, *Int. J. Electron.* 80(2): p. 191-200. 1996.
- Senjyu, T., S. Yokoda, H. Miyazato and K. Uezato. Speed control of ultrasonic motors by adaptive control with a simplified mathematical model, *IEE Proc.-Electr. Power Appl.* 145(3): p. 180-184. 1998.
- Senjyu, T., S. Yokoda, and K. Uezato. Speed control of ultrasonic motors using fuzzy neural network, *J. Intell. Fuzzy Syst.* 8(2): p. 135-146. 2000.
- Sherrit, S., S. P. Leary, B. P. Dolgin and Y. Bar-Cohen. Comparison of the Mason and KLM equivalent circuits for piezoelectric resonators in the thickness mode, *Proceedings of the IEEE Ultrasonics Symposium.* 2921-926. 1999.
- Shi, X. H., Y. C. Liang, H. P. Lee, W. Z. Lin, X. Xu and S. P. Lim. Improved elman networks and applications for controlling ultrasonic motors, *Appl. Artif. Intell.* 18(7): p. 603-629. 2004.
- Shimanuki, M., M. Aoyagi, and Y. Tomikawa. Single-resonance longitudinal and torsional vibrator combination-type motor - improvement of motor characteristics, *Jpn. J. Appl. Phys. Part 1 - Regul. Pap. Short Notes Rev. Pap.* 33(5B): p. 3075-3080. 1994.
- Singh, B. and S. Chakraverty. Transverse Vibration of Circular and Elliptic Plates with Quadratically Varying Thickness, *Appl. Math. Model.* 16(5): p. 269-274. 1992.
- Singh, B. and S.M. Hassan. Transverse vibration of a circular plate with arbitrary thickness variation, *Int. J. Mech. Sci.* 40(11): p. 1089-1104. 1998.

- Singh, B. and V. Saxena. Axisymmetrical Vibration of a Circular Plate with Double Linear Variable Thickness, *J. Sound Vibr.* 179(5): p. 879-897. 1995.
- Smith, F.C. On the logarithmic solutions of the generalized hypergeometric equation when $p = q+1$., *Bull. Amer. Math. Soc.* 45629-636. 1939.
- Storck, H. and J. Wallaschek. The effect of tangential elasticity of the contact layer between stator and rotor in travelling wave ultrasonic motors, *Int. J. Non-Linear Mech.* 38(2): p. 143-159. 2003.
- Suetomo, A. and Y. Tomikawa. Rectangular-plate-type piezoelectric ceramics ultrasonic motor using double 1st resonance modes of longitudinal and width-bending vibrations, *Jpn. J. Appl. Phys. Part 1 - Regul. Pap. Short Notes Rev. Pap.* 43(5B): p. 2871-2872. 2004.
- Sun, C.T. and X.D. Zhang. Use of Thickness-Shear Mode in Adaptive Sandwich Structures, *Smart Mater. Struct.* 4(3): p. 202-206. 1995.
- Sun, D., J.B. Liu, and X. Ai. Modeling and performance evaluation of traveling-wave piezoelectric ultrasonic motors with analytical method, *Sens. Actuator A-Phys.* 100(1): p. 84-93. 2002.
- Sun, D. C., D. J. Wang, Z. L. Xu and H. X. Wu. Distributed piezoelectric element method for vibration control of smart plates, *Aiaa J.* 37(11): p. 1459-1463. 1999.
- Suzuki, A., M. Kihara, Y. Katsumata, N. Kikuchi and J. Tsujino. Configuration of a transverse vibration rod type ultrasonic motor using three longitudinal transducers driven in three different vibration phases, *Jpn. J. Appl. Phys. Part 1 - Regul. Pap. Short Notes Rev. Pap.* 43(5B): p. 2901-2904. 2004.
- Suzuki, Y., K. Tani, and T. Sakuhara. Development of a new type piezoelectric micro-motor, *Sens. Actuator A-Phys.* 83(1-3): p. 244-248. 2000.
- Takano, T., Y. Tomikawa, and C. Kusakabe. Same phase drive-type ultrasonic motors using 2 degenerate bending vibration modes of a disk, *IEEE Trans. Ultrason. Ferroelectr. Freq. Control.* 39(2): p. 180-186. 1992.
- Takano, T., Y. Tomikawa, and C. Kusakabe. Operating characteristics of a same-phase drive-type ultrasonic motor using a flexural disk vibrator, *Jpn. J. Appl. Phys. Part 1 - Regul. Pap. Short Notes Rev. Pap.* 38(5B): p. 3322-3326. 1999.
- Takano, T., Y. Tomikawa, T. Ogasawara, S. Sugawara and M. Konno. Ultrasonic motors using piezoelectric ceramic multimode vibrators, *IEEE Trans. Ultrason. Ferroelectr. Freq. Control.* 37(3): p. 224-229. 1990.
- Thurston, E.G. and Y.T. Tsui. On the lowest flexural resonant frequency of a circular disk of linearly varying thickness driven at its center, *J. Acoust. Soc. Am.* 27926-929. 1955.
- Texas Instruments, LF353 datasheet. <http://www.ti.com/>
- Texas Instruments, OPA27 datasheet. <http://www.ti.com/>
- Texas Instruments, SN74LS74A datasheet. <http://www.ti.com/>

- Texas Instruments, TLC555 datasheet. <http://www.ti.com/>
- Timoshenko, S., D.H. Young, and W. Weaver. *Vibration problems in engineering*. pp.xiii, 521 p., New York,: Wiley. 1974.
- Tomikawa, Y., K. Adachi, M. Aoyagi, T. Sagae and T. Takano. Some constructions and characteristics of rod-type piezoelectric ultrasonic motors using longitudinal and torsional vibrations, *IEEE Trans. Ultrason. Ferroelectr. Freq. Control.* 39(5): p. 600-608. 1992.
- Tong, J. H., T. H. Cui, P. G. Shao and L. D. Wang. Piezoelectric micromotor based on the structure of serial bending arms, *IEEE Trans. Ultrason. Ferroelectr. Freq. Control.* 50(9): p. 1100-1104. 2003.
- Trindade, M.A., A. Benjeddou, and R. Ohayon. Finite element modelling of hybrid active-passive vibration damping of multilayer piezoelectric sandwich beams - part I: Formulation, *Int. J. Numer. Methods Eng.* 51(7): p. 835-854. 2001.
- Trindade, M.A., A. Benjeddou, and R. Ohayon. Finite element modelling of hybrid active-passive vibration damping of multilayer piezoelectric sandwich beams - part II: System analysis, *Int. J. Numer. Methods Eng.* 51(7): p. 855-864. 2001.
- Tsujino, J. Ultrasonic motor using a one-dimensional longitudinal-torsional vibration converter with diagonal slits, *Smart Mater. Struct.* 7(3): p. 345-351. 1998.
- Tzou, H.S. and H.Q. Fu. A Study of Segmentation of Distributed Piezoelectric Sensors and Actuators .1. Theoretical-Analysis, *J. Sound Vibr.* 172(2): p. 247-259. 1994.
- Tzou, H.S. and H.Q. Fu. A Study of Segmentation of Distributed Piezoelectric Sensors and Actuators .2. Parametric Study and Active Vibration Controls, *J. Sound Vibr.* 172(2): p. 261-275. 1994.
- Uchiki, T., T. Nakazawa, K. Nakamura, M. Kurosawa and S. Ueha. Ultrasonic motor utilizing elastic fin rotor, *Jpn. J. Appl. Phys. Part 1 - Regul. Pap. Short Notes Rev. Pap.* 30(9B): p. 2289-2291. 1991.
- Uchino, K. *Piezoelectric actuators and ultrasonic motors*. pp.viii, 349 p., Boston: Kluwer Academic Publishers. 1997.
- Uchino, K. Piezoelectric ultrasonic motors: overview, *Smart Mater. Struct.* 7(3): p. 273-285. 1998.
- Uchino, K., S. Cagatay, B. Koc, S. Dong, P. Bouchilloux and M. Strauss. Micro piezoelectric ultrasonic motors, *J. Electroceram.* 13(1-3): p. 393-401. 2004.
- Ueha, S. and Y. Tomikawa. *Ultrasonic motors : theory and applicationms*. pp.ix, 297 p., Oxford New York: Clarendon Press ;Oxford University Press. 1993.
- Vasques, C.M.A. and J.D. Rodrigues. Coupled three-layered analysis of smart piezoelectric beams with different electric boundary conditions, *Int. J. Numer. Methods Eng.* 62(11): p. 1488-1518. 2005.
- Vyshnevskyy, O., S. Kovalev, and J. Mehner. Coupled tangential-axial resonant modes of piezoelectric hollow cylinders and their application in ultrasonic motors, *IEEE Trans. Ultrason. Ferroelectr. Freq. Control.* 52(1): p. 31-36. 2005.

- Wallaschek, J. Piezoelectric ultrasonic motors, *J. Intell. Mater. Syst. Struct.* 6(1): p. 71-83. 1995.
- Wallaschek, J. Contact mechanics of piezoelectric ultrasonic motors, *Smart Mater. Struct.* 7(3): p. 369-381. 1998.
- Wang, H.-G. Generalized hypergeometric function solutions on the transverse vibration of a class of non-uniform beams, *J. Appl. Mech.-Trans. ASME.* 34(12): p. 702-708. 1967.
- Wang, J. Generalized power series solutions of the vibration of classical circular plates with variable thickness, *J. Sound Vibr.* 202(4): p. 593-599. 1997.
- Wang, Q., S. T. Quek, C. T. Sun and X. Liu. Analysis of piezoelectric coupled circular plate, *Smart Mater. Struct.* 10(2): p. 229-239. 2001.
- Wang, S.Y. A finite element model for the static and dynamic analysis of a piezoelectric bimorph, *Int. J. Solids Struct.* 41(15): p. 4075-4096. 2004.
- Wen, F.L., S.C. Mou, and M. Ouyang. Design and construction of shaft-driving type piezoceramic ultrasonic motor, *Ultrasonics.* 43(1): p. 35-47. 2004.
- Wen, F.L., C.Y. Yen, and M. Ouyang. Thin-disk piezoceramic ultrasonic motor. Part I: design and performance evaluation, *Ultrasonics.* 41(6): p. 437-450. 2003.
- Williams, A.L.W. and W.J. Brown. Piezoelectric motor, US patent 2439499, Piezoelectric motor, US patent 2439499. 1948.
- Wriggers, P. Computational contact mechanics. pp.xxii, 441 p., Hoboken, NJ: J. Wiley & Sons. 2002.
- Wu, T.Y. and G.R. Liu. Free vibration analysis of circular plates with variable thickness by the generalized differential quadrature rule, *Int. J. Solids Struct.* 38(44-45): p. 7967-7980. 2001.
- Xu, X., Y. C. Liang, H. P. Lee, W. Z. Lin, S. P. Lim, K. H. Lee and X. H. Shi. Identification and speed control of ultrasonic motors based on neural networks, *J. Micromech. Microeng.* 13(1): p. 104-114. 2003.
- Yang, J.S. The Vibration of a Circular Plate with Varying Thickness, *J. Sound Vibr.* 165(1): p. 178-184. 1993.
- Yao, K., B. Koc, and K. Uchino. Longitudinal-bending mode micromotor using multilayer piezoelectric actuator, *IEEE Trans. Ultrason. Ferroelectr. Freq. Control.* 48(4): p. 1066-1071. 2001.
- Yen, C.Y., F.L. Wen, and M. Ouyang. Thin-disc piezoceramic ultrasonic motor. Part II: system construction and control, *Ultrasonics.* 41(6): p. 451-463. 2003.
- Yi, S., S. F. Ling, M. Ying, H. H. Hilton and J. R. Vinson. Finite element formulation for anisotropic coupled piezoelectro- hygro- thermo- viscoelasto- dynamic problems, *Int. J. Numer. Methods Eng.* 45(11): p. 1531-1546. 1999.
- Zhang, X.D. and C.T. Sun. Analysis of a sandwich plate containing a piezoelectric core, *Smart Mater. Struct.* 8(1): p. 31-40. 1999.

-
- Zhong, Z.-H. Finite element procedures for contact-impact problems. pp.xi, 371 p., Oxford: Oxford University Press. 1993.
- Zhu, M.L. Contact analysis and mathematical modeling of traveling wave ultrasonic motors, IEEE Trans. Ultrason. Ferroelectr. Freq. Control. 51(6): p. 668-679. 2004.
- Zienkiewicz, O.C. and R.L. Taylor. The finite element method. Oxford ; Boston: Butterworth-Heinemann. 2000.

Appendix A

Description of USM

A.1 Kumada motor

Fig. 1.1 (a) illustrates how the vibrations produce rotor motion. The piezoelectric stack induces a longitudinal mode in the stator which in turn produces a bending mode in the extension/torsion coupler. The torsional coupler looks like an old fashioned TV channel knob, consisting of two legs which transform longitudinal vibration generated by the Langevin vibrator to a bending mode of the knob disk, and a vibratory extruder. Notice that this extruder is aligned with a certain cant angle to the legs, which transforms the bending to a torsion vibration. This transverse moment coupled with the bending up-down motion leads to an elliptical rotation on the tip portion, as illustrated in Fig. 1.1 (b). It is this motion, through contact interaction, that caused the rotor to spin. A motor 30 mm \times 60 mm in size and 20 - 30° cant angle between a leg and a vibratory piece provided torque as high as 1.3 Nm and an efficiency of 80%. However, this type provides only unidirectional rotation.

A.2 Suzuki motor

In 2000 Suzuki *et al.* devised a piezoelectric micromotor that was simply structured and suited for miniaturization. Fig. 1.2 (a) shows the piezoelectric micromotor structure. The stator is made from stainless steel and glued to piezoelectric ceramics. The rotor

is made from nickel by electroforming and gilding. The shaft is made from stainless steel. The flat spring has three beam-shaped suspension parts between the center part and the outer part. The flat spring is made from stainless steel by etching process, and three suspensions and the central part are etched once more, so that the outer part is thicker than the suspensions and the central part. The micromotor is constructed by piling up the shaft, stator, rotor and flat spring in this order. The central part of the flat spring and the top of the shaft are welded with laser when the micromotor is assembled. The function of the flat spring structure is to generate the contact pressure between the stator and the rotor via the suspended bending parts. It is also possible to control contact conditions between the stator and rotor by choice of the shape and material of the flat spring structure. Therefore, the size of the new micromotor is 2 mm in diameter and 0.3 mm in height. The volume is 0.49 mm^3 . Fig. 1.2 (b) shows the operating principle of micromotor. The piezoelectric ceramics are shaped rectangular parallelepipeds, which are polarized in the direction of their thickness. They expand and contract when alternating voltage is applied to them. Since the cantilever oscillators have flexural vibration, the elliptic movements are excited at the free end of the cantilever oscillators. After the rotor and the stator with cantilever oscillators are assembled, the elliptic movements are transmitted to the rotor, and only the horizontal vibration of elliptic movements generates the rotor rotation. The most efficient rotation is achieved when the frequency of the applied voltage equals the resonance frequency of the cantilever oscillator. The piezoelectric micromotor can rotate stably, and the starting torque is measured to be $3.2 \mu\text{Nm}$.

A.3 Ohnishi motor

In 1993, Onishi *et al.* investigated a piezoelectric USM, which used longitudinal and torsional composite vibration in order to obtain high torque characteristics with small diameter. The stator consists of two piezoelectric ceramic blocks, two metal cylinders,

which are head mass and rear mass, two insulating plates and supporting plate as shown in Fig. 1.3 (a). All these are bolted together in to form a Langevin resonator. The lower piezoelectric ceramic block operates the longitudinal vibration mode. It consists of 12 stack piezoelectric ceramic circular plates. Each plate is polarized in the thickness direction. These ceramic plates have outer diameter of 20 mm, inner diameter of 8 mm and thickness of 0.5 mm. The upper piezoelectric ceramic block operates the torsional vibration mode and consists of 8 stack piezoelectric ceramic circular plates, which are made of the same ceramic material as the lower ceramic block and polarized in the circumferential direction. The ceramic plates have outer diameter of 20 mm, inner diameter of 8 mm and thickness of 1 mm. Phosphor bronze electrode plates 0.05 mm are arranged between all the piezoelectric ceramic plates. The piezoelectric ceramic blocks, two insulating plates made of alumina and the supporting plate made of stainless steel, are put between the head mass made of aluminum and the rear mass made of stainless steel, which are bolted together to form a stator. The two insulating plates, 1 mm thick, respectively, were used to enable the driving of the upper ceramic block, operating in the longitudinal mode, and the lower ceramic block, operating in the torsional mode, independently. The stainless steel bolt is 5 mm in diameter. A rotor, guided by the shaft and a bearing, is pressed against the stator surface by Belleville springs, which can change the rotor pressing force by adjusting a nut. A wear-proof sheet (polyester resin) with thickness of 0.2 mm is adhered to the stator surface, in order to convert the ultrasonic elliptical vibration of the stator to rotational motion of the rotor efficiently by frictional force as well as to protect the rotor and the stator surfaces from wear. Overall motor dimensions are 20 mm diameter and 77 mm length.

The operation principle for the USM is shown in Fig. 1.3 (b). Longitudinal vibration displacement is in a direction parallel to the axis of the stator, while torsional vibration displacement is in the circumferential direction. Hence, an elliptical motion can be obtained at the stator surface by simultaneous oscillation for these two vibration modes

by applying AC electric fields to both piezoelectric ceramic blocks. For a half period (1-2-3 in Fig. 1.3 (b)), since the rotor is in contact with the stator, the rotational force is transmitted from the stator to the rotor. For the other part of a period (3-4-1 Fig. 1.3 (b)), the rotor is released from the stator, so that the rotational force is not transmitted. The rotor can thus be rotated in a designated direction by the stator motion. Moreover, it is obvious that the rotor can be rotated reversibly by changing the phase difference by between the longitudinal and torsional vibration modes. Dynamic characteristics for the motor were examined. The motor exhibited 0.4 Nm maximum torque, 450 rpm maximum rotational speed, 40% maximum efficiency, quick responsiveness and reversibility.

A.4 Dong motor

The objective of Dong *et al.*'s research was to develop an improved method to excite a traveling wave in a single piezoelectric ceramic plate (stator) via the shear modes. Specifically, the d_{15} piezoelectric effect, which is much higher than the d_{31} used in common plate types USM, has been used to excite a flexural traveling wave. Fig. 1.4 (a) shows the stator structure which had an outer diameter of 10.5 mm, an inner diameter of 1.8 mm, and a thickness of 0.56 mm. The 18-teeth ring has the same outer diameter as that of piezoelectric ceramic plate with 0.5 mm in width and 1.5 mm in height. Fig. 1.4 (b) shows a piezoelectric ceramic plate with a small center hole polarized in its radial direction. The bottom electrode of the plate is divided into four parts (*a*, *b*, *c*, and *d*), and the top electrode is grounded and covers the entire plate. To excite higher-order modes, the electrode can be divided into eight or more parts. Two pairs of alternative voltages, phase shifted by 90° (sin and cos) were applied to electrodes *a* and *c* and *b* and *d*, respectively. Because the voltages were applied out of phase, the two shear modes will produce a rotation shown in Fig. 1.4 (c); consequently, a shear-shear flexural traveling wave is excited.

At a resonance frequency 38.83 kHz, the motor had a maximum rotational speed of

160 rpm. Under optimum conditions, the maximum speed was slightly increased to 200 rpm. With a suitable polymer/ceramic powder mixture frictional material, the motor's maximum torque was around 1.8 mNm.

A.5 Flynn motor

In 1992, Flynn *et al.* fabricated the world's first ferroelectric thin film motor. The significance of their contribution is that if PZT can be deposited in a thin film form compatible with silicon processing, motors can be manufactured in a batch printing process instead of being individually machined. Additionally, these motors should show significant improvements in performance over bulk PZT motors. This is because the films are very thin that it is possible to apply much higher electric fields than in thicker bulk devices, hence leading to higher energy densities.

Eight electrodes are patterned radially around a center point and driven four-phase over two wavelengths as shown in Fig. 1.6. Eight probes would be needed to drive the motor in this particular example. This stator has an inner-diameter of 1.2mm and an outer diameter of 2 mm placed over a 2.2 mm \times 2.2 mm square membrane. The eight pads are driven in a four phase sequence (sin, cos, -sin and -cos), repeated twice. Note that there are four extra pads to be used as sensors, since the piezoelectric film is reciprocal, where a bending moment can induce a voltage.

A 4V peak to peak drive signal at 90 kHz competently spins a fairly large rotor, a glass lens 1.5 mm in diameter, at 100-300 rpm.

A.6 Cagatay motor

In 2004 Cagatay *et al.* developed a micro USM with low manufacturing cost, simpler driving circuit, and scalability. The stator of the prototype motor consists of a hollow metal tube (brass) with an outer diameter of 1.6 mm, an inner diameter of 0.8 mm,

a length of 4 mm, and two rectangular piezoelectric plates with dimensions, 4 mm in length, 1 mm in width, and 0.3 mm in thickness shown in Fig. 1.7 (a). A rod connects a pair of ferrules which are the rotors, one at each end of the cylinder as shown in Fig. 1.7 (b).

The principle is briefly introduced. In general, a square beam has two orthogonal bending modes whose resonance frequencies are equal to each other. The first bending mode frequencies in any direction for circular cylinders are also equal to each other. The stator of the motor presented in the study combines the circular and square cross sections. Two surfaces of the hollow metal cylinder were polished at an angle of 90° with respect to each other and two uniformly rectangular piezoelectric plates were bonded onto the flat orthogonal surfaces of the cylinder. This causes the stator to have two degenerated orthogonal bending modes, whose resonance frequencies are close to each other. The split of the bending mode frequencies is due to the partially square/partially circular external surface of the hollow cylinder. Because the piezoelectric plates are oriented by 45° to the direction of minimum and maximum bending moment of inertia (x' and y' axis), driving one piezoelectric plate (while short circuiting the other to ground) at a frequency between the two orthogonal bending mode frequencies excites both modes, thus, causing the cylinder to wobble. When the other piezoelectric plate is driven at the same frequency, the direction of wobble motion is reversed.

The working frequency under zero load was approximately 227-233 kHz. Although the size is small, relatively high power was obtained under an optimized load condition: torque of 0.06 mNm, maximum power of 3.2 mW with a speed of 1127 rpm, and maximum efficiency of 11% under 48 V_{rms} at 221 kHz.

Appendix B

Logarithmic Solutions of Generalized Hypergeometric Equation

In Eq. (2.5), the generalized hypergeometric equation with $p = 0$ and $q = 3$, is an ordinary differential equation with a regular singular point at the origin, and assume to have a solution of the form

$$z(x) = \sum_{k=0}^{\infty} c_k x^{\rho+k} \quad c_0 \neq 0 \quad (\text{B.1})$$

Substituting Eq. (B.1) into Eq. (2.5) yields

$$\begin{aligned} & \sum_{k=0}^{\infty} c_k [x^{\rho+k} - \prod_{i=1}^4 (\rho + k + \gamma_i - 1) x^{\rho+k-1}] \\ &= \sum_{k=1}^{\infty} [c_{k-1} - c_k \prod_{i=1}^4 (\rho + k + \gamma_i - 1)] x^{\rho+k-1} - c_0 \prod_{i=1}^4 (\rho + \gamma_i - 1) x^{\rho-1} \end{aligned} \quad (\text{B.2})$$

Then, the indicial equation (or characteristic equation) is

$$c_0 \prod_{i=1}^4 (\rho - 1 + \gamma_i) = 0 \quad (\text{B.3})$$

$c_0 \neq 0$, Eq. (B.3) yields four values of ρ , namely,

$$\rho_i = 1 - \gamma_i, i = 1 \dots 4 \quad (\text{B.4})$$

The coefficients c_k satisfy the recurrence formula

$$c_k = \frac{c_{k-1}}{\prod_{i=1}^4 (\rho + k - 1 + \gamma_i)} \quad (\text{B.5})$$

which leads to

$$c_k = c_0 \prod_{i=1}^4 \frac{\Gamma(\rho - 1 + \gamma_i)}{\Gamma(\rho - 1 + \gamma_i + k)} \quad (\text{B.6})$$

Let $c_0 = 1$ and substitute Eq. (B.6) into Eq. (B.1) gives

$$z(x) = \sum_{k=0}^{\infty} x^{\rho+k} \prod_{i=1}^4 \frac{\Gamma(\rho + \gamma_i)}{\Gamma(\rho + \gamma_i + k)} \quad (\text{B.7})$$

If no two values of γ_i are equal or differ by an integer, from Eq. (B.7), the various solutions may be obtained by setting ρ equal to the roots of Eq. (B.4). This leads to Eq. (2.7).

If only λ numbers ($\lambda = 2, 3$ or 4 in the case plate vibration) of γ_i are equal or differ by an integer (as discussed in section 3), Eq. (2.5) has $\lambda - 1$ logarithmic solutions. For the vibration of plates, the largest value of λ is 4 . When λ is 2 , the logarithmic solutions have been given by Smith (1939), MacRobert (1962) and Wang (1967). The logarithmic solutions are derived here for λ equal to 3 or 4 . For completeness, the solutions for $\lambda = 2$ are also presented. Thus, $z_2(x)$, $z_3(x)$, and $z_4(x)$ can be written according to the theory of Frobenius (Smith, 1939) as

$$z_2(x) = v'(\rho)_{\rho=1-\gamma_2} = \sum_{k=0}^{\infty} f_k(\Gamma) x^{\rho+k} (c_0 \ln x + g_k^1) \quad (\text{B.8})$$

$$z_3(x) = v''(\rho)_{\rho=1-\gamma_3} = \sum_{k=0}^{\infty} f_k(\Gamma) x^{\rho+k} (c_0 \ln^2 x + 2g_k^1 \ln x + g_k^2) \quad (\text{B.9})$$

$$z_4(x) = v'''(\rho)_{\rho=1-\gamma_4} = \sum_{k=0}^{\infty} f_k(\Gamma) x^{\rho+k} (c_0 \ln^3 x + 3g_k^1 \ln^2 x + 3g_k^2 \ln x + g_k^3) \quad (\text{B.10})$$

Where

$$\begin{aligned} v(\rho) &= c_0(\rho) \sum_{k=0}^{\infty} f_k(\Gamma) x^{\rho+k} \\ c_0(\rho) &= c_0'(\rho + \gamma_r - 1)^{\lambda-1} \\ f_k(\Gamma) &= \prod_{i=1}^4 \frac{\Gamma(\rho + \gamma_i)}{\Gamma(\rho + \gamma_i + k)} \\ g_k^1 &= \frac{\partial c_0}{\partial \rho} + \Phi_{0k}^{ij} c_0 \\ g_k^2 &= \frac{\partial^2 c_0}{\partial^2 \rho} + 2\Phi_{0k}^{ij} \frac{\partial c_0}{\partial \rho} + [(\Phi_{0k}^{ij})^2 + \Phi_{0k}^{ij}] c_0 \\ g_k^3 &= \frac{\partial^3 c_0}{\partial^3 \rho} + 3\Phi_{0k}^{ij} \frac{\partial^2 c_0}{\partial^2 \rho} + 3[(\Phi_{0k}^{ij})^2 + \Phi_{1k}^{ij}] \frac{\partial c_0}{\partial \rho} + [(\Phi_{0k}^{ij})^3 + 3\Phi_{0k}^{ij} \Phi_{1k}^{ij} + \Phi_{2k}^{ij}] c_0 \end{aligned}$$

and

$$\begin{aligned}
 \Phi_{nk}^{ij} &= \Psi_{nk}^{ij} + \sum_{t=1}^j \pi \frac{\partial^n}{\partial^n \rho} \cot \pi(\rho + \gamma_t + k) - \sum_{t=1}^i \pi \frac{\partial^n}{\partial^n \rho} \cot \pi(\rho + \gamma_t) \\
 \Psi_{nk}^{ij} &= \sum_{t=1+i}^4 \varphi_n(\rho + \gamma_t) + \sum_{t=1}^i (-1)^n \varphi_n(1 - \rho - \gamma_t) \\
 &\quad - \sum_{t=1+j}^4 \varphi_n(\rho + \gamma_t + k) - \sum_{t=1}^j (-1)^n \varphi_n(1 - \rho - \gamma_t - k) \\
 &\quad n = 0, 1, 2; i, j = 0, 1, 2, 3
 \end{aligned} \tag{B.11}$$

$\varphi_n(z)$ is a polygamma function. In the above development, the following formula has been used:

$$\varphi_n(1 - z) + (-1)^{n+1} \varphi_n(z) = (-1)^n \pi \frac{d^n}{dz^n} \cot \pi z, n = 0, 1, 2 \dots \tag{B.12}$$

The logarithmic solutions of Eqs. (B.8)-(B.10) are in a general form which cannot be used directly. The specific forms are be derived in the following.

B.1 $z_2(x)$

Under this case, $c_0 = c'_0(\rho + \gamma_2 - 1)$, where c'_0 is an arbitrary constant independent of ρ , and $z_2(x)$ consists of two parts depending on the range of k . When $k \geq \gamma_2 - \gamma_1$, using the relation

$$\Gamma(z)\Gamma(1 - z) = \frac{\pi}{\sin \pi z} \tag{B.13}$$

where z is an arbitrary complex number, gives

$$\begin{aligned}
 f_k(\Gamma)_{\rho=1-\gamma_2} &= \frac{\prod_{i=2}^4 \Gamma(\rho + \gamma_i)}{\prod_{i=1}^4 \Gamma(\rho + \gamma_i + k)} \frac{1}{\rho + \gamma_2 - 1} \lim_{\rho \rightarrow 1-\gamma_2} \Gamma(\rho + \gamma_1)(\rho + \gamma_2 - 1) \\
 &= \frac{\prod_{i=2}^4 \Gamma(1 - \gamma_2 + \gamma_i)}{\prod_{i=1}^4 \Gamma(1 - \gamma_2 + \gamma_i + k)} \frac{(-1)^{1-\gamma_2+\gamma_1}}{\Gamma(\gamma_2 - \gamma_1)} \frac{1}{\rho + \gamma_2 - 1}
 \end{aligned} \tag{B.14}$$

$$\left(\frac{1}{\rho + \gamma_2 - 1} c_0 \right)_{\rho=1-\gamma_2} = c'_0 \tag{B.15}$$

The coefficient of $\ln x$ in Eq. (B.8) can be calculated as follows:

$$\left(\sum_{k=\gamma_2-\gamma_1}^{\infty} f_k(\Gamma)x^{\rho+k}c_0 \right)_{\rho=1-\gamma_2} = c'_0 \frac{(-1)^{1-\gamma_2+\gamma_1} \prod_{i=2}^4 \Gamma(1-\gamma_2+\gamma_i)}{\Gamma(\gamma_2-\gamma_1) \prod_{i=1}^4 \Gamma(1-\gamma_1+\gamma_i)} z_1(x) \quad (\text{B.16})$$

c'_0 is chosen to make the coefficient of $z_1(x)$ equal to 1. That is,

$$c'_0 = \frac{\Gamma(\gamma_2-\gamma_1) \prod_{i=1}^4 \Gamma(1-\gamma_1+\gamma_i)}{(-1)^{1-\gamma_2+\gamma_1} \prod_{i=2}^4 \Gamma(1-\gamma_2+\gamma_i)} \quad (\text{B.17})$$

Since

$$\begin{aligned} \left(\frac{1}{\rho+\gamma_2-1} g_k^1 \right)_{\rho=1-\gamma_2} &= \frac{c'_0}{\rho+\gamma_2-1} + c'_0 \Phi_{0k}^{10} \\ &= \frac{c'_0}{\rho+\gamma_2-1} + c'_0 (\Psi_{0k}^{10} - \pi \cot \pi(\rho+1)) \\ &= c'_0 \Psi_{0k}^{10} \end{aligned} \quad (\text{B.18})$$

the non-logarithmic terms in Eq. (B.8) can be obtained:

$$\begin{aligned} \left(\sum_{k=\gamma_2-\gamma_1}^{\infty} f_k(\Gamma)x^{\rho+k}g_k^1 \right)_{\rho=1-\gamma_2} &= \sum_{s=0}^{\infty} f_s(\Gamma)x^{\rho+\gamma_2-\gamma_1+s} c'_0 \Psi_{0s}^{10} \\ &= x^{1-\gamma_1} \sum_{s=0}^{\infty} \Psi_{0s}^{10} x^s \prod_{i=1}^4 \frac{\Gamma(1-\gamma_1+\gamma_i)}{\Gamma(1-\gamma_1+\gamma_i+s)} \end{aligned} \quad (\text{B.19})$$

When $0 \leq k \leq \gamma_2 - \gamma_1 - 1$,

$$\begin{aligned} f_k(\Gamma)_{\rho=1-\gamma_2} &= \prod_{i=2}^4 \frac{\Gamma(\rho+\gamma_i)}{\Gamma(\rho+\gamma_i+k)} \lim_{\rho \rightarrow 1-\gamma_2} \frac{\Gamma(\rho+\gamma_1)}{\Gamma(\rho+\gamma_1+k)} \\ &= (-1)^k \prod_{i=2}^4 \frac{\Gamma(1-\gamma_2+\gamma_i)}{\Gamma(1-\gamma_2+\gamma_i+k)} \frac{\Gamma(\gamma_2-\gamma_1-k)}{\Gamma(\gamma_2-\gamma_1)} \end{aligned} \quad (\text{B.20})$$

$$\begin{aligned} (g_k^1)_{\rho=1-\gamma_2} &= c'_0 + c'_0(\rho+\gamma_2-1)\Phi_{0k}^{11} \\ &= c'_0 + c'_0(\rho+\gamma_2-1)(\Psi_{0k}^{11} + \lim_{\rho \rightarrow 1-\gamma_2} (\pi \cot \pi(\rho+1+k) - \pi \cot \pi(\rho+1))) \\ &= c'_0 + c'_0(\rho+\gamma_2-1)\Psi_{0k}^{11} \\ &= c'_0 \end{aligned} \quad (\text{B.21})$$

then

$$\begin{aligned} \sum_{k=0}^{\gamma_2-\gamma_1-1} f_k(\Gamma)x^{\rho+k}g_k^1 &= \sum_{s=1}^{\gamma_2-\gamma_1} f_s(\Gamma)x^{\rho+\gamma_2-\gamma_1-s}g_s^1 \\ &= \prod_{i=2}^4 (\gamma_i - \gamma_1) \frac{1}{x^{\gamma_1}} {}_5F_0([1, 1, 1 + \gamma_1 - \gamma_2, 1 + \gamma_1 - \gamma_3, 1 + \gamma_1 - \gamma_4], [], \frac{1}{x}) \end{aligned} \quad (\text{B.22})$$

$$(c_0)_{\rho=1-\gamma_2} = c'_0(\rho + \gamma_2 - 1) = 0 \quad (\text{B.23})$$

Hence

$$\begin{aligned} z_2(x) &= z_1(x) \ln x + x^{1-\gamma_1} \sum_{s=0}^{\infty} \Psi_{0s}^{10} x^s \prod_{i=1}^4 \frac{\Gamma(1 - \gamma_1 + \gamma_i)}{\Gamma(1 - \gamma_1 + \gamma_i + s)} \\ &+ \prod_{i=2}^4 (\gamma_i - \gamma_1) \frac{1}{x^{\gamma_1}} {}_5F_0([1, 1, 1 + \gamma_1 - \gamma_2, 1 + \gamma_1 - \gamma_3, 1 + \gamma_1 - \gamma_4], [], \frac{1}{x}) \end{aligned} \quad (\text{B.24})$$

B.2 $z_3(x)$

Under this case $c_0 = c'_0(\rho + \gamma_3 - 1)^2$. For $k \geq \gamma_3 - \gamma_1$, the coefficient of $\ln^2 x$ in Eq. (B.9) can be calculated using

$$\begin{aligned} \left(\sum_{k=\gamma_3-\gamma_1}^{\infty} f_k(\Gamma) x^{\rho+k} c_0 \right)_{\rho=1-\gamma_3} &= \left(\sum_{s=0}^{\infty} f_s(\Gamma) x^{\rho+\gamma_3-\gamma_1+s} c_0 \right)_{\rho=1-\gamma_3} \\ &= \frac{c'_0 (-1)^{\gamma_2+\gamma_1} \Gamma(1 - \gamma_3 + \gamma_4)}{\prod_{i=1}^4 \Gamma(1 - \gamma_1 + \gamma_i) \prod_{i=1}^2 \Gamma(\gamma_3 - \gamma_i)} z_1(x) \end{aligned} \quad (\text{B.25})$$

c'_0 is chosen by making the coefficient of $z_1(x)$ equal to 1:

$$c'_0 = \frac{\prod_{i=1}^4 \Gamma(1 - \gamma_1 + \gamma_i) \prod_{i=1}^2 \Gamma(\gamma_3 - \gamma_i)}{(-1)^{\gamma_2+\gamma_1} \Gamma(1 - \gamma_3 + \gamma_4)} \quad (\text{B.26})$$

then

$$\begin{aligned} \left(\sum_{k=\gamma_3-\gamma_1}^{\infty} f_k(\Gamma) x^{\rho+k} g_k^1 \right)_{\rho=1-\gamma_3} &= \left(\sum_{s=0}^{\infty} f_s(\Gamma) x^{\rho+\gamma_3-\gamma_1+s} g_s^1 \right)_{\rho=1-\gamma_3} \\ &= x^{1-\gamma_1} \sum_{s=0}^{\infty} \Psi_{0s}^{20} x^s \frac{\prod_{i=1}^4 \Gamma(1 - \gamma_1 + \gamma_i)}{\prod_{i=1}^4 \Gamma(1 - \gamma_1 + \gamma_i + s)} \end{aligned} \quad (\text{B.27})$$

$$\begin{aligned} \left(\sum_{k=\gamma_3-\gamma_1}^{\infty} f_k(\Gamma) x^{\rho+k} g_k^2 \right)_{\rho=1-\gamma_3} &= \left(\sum_{s=0}^{\infty} f_s(\Gamma) x^{\rho+\gamma_3-\gamma_1+s} g_s^2 \right)_{\rho=1-\gamma_3} \\ &= x^{1-\gamma_1} \sum_{s=0}^{\infty} [(\Psi_{0s}^{20})^2 + \Psi_{1s}^{20} + 2\pi^2] x^s \frac{\prod_{i=1}^4 \Gamma(1 - \gamma_1 + \gamma_i)}{\prod_{i=1}^4 \Gamma(1 - \gamma_1 + \gamma_i + s)} \end{aligned} \quad (\text{B.28})$$

When $\gamma_3 - \gamma_2 \leq k \leq \gamma_3 - \gamma_1 - 1$,

$$\begin{aligned} & \left(\sum_{k=\gamma_3-\gamma_2}^{\gamma_3-\gamma_1-1} f_k(\Gamma) x^{\rho+k} g_k^1 \right)_{\rho=1-\gamma_3} = \left(\sum_{s=1}^{\gamma_2-\gamma_1} f_s(\Gamma) x^{\rho+\gamma_3-\gamma_1-s} g_s^1 \right)_{\rho=1-\gamma_3} \\ & = \prod_{i=2}^4 (\gamma_i - \gamma_1) \frac{1}{x^{\gamma_1}} {}_5F_0([1, 1, 1 + \gamma_1 - \gamma_2, 1 + \gamma_1 - \gamma_3, 1 + \gamma_1 - \gamma_4], [], \frac{1}{x}) \end{aligned} \quad (\text{B.29})$$

$$\begin{aligned} & \left(\sum_{k=\gamma_3-\gamma_2}^{\gamma_3-\gamma_1-1} f_k(\Gamma) x^{\rho+k} g_k^2 \right)_{\rho=1-\gamma_3} = \left(\sum_{s=1}^{\gamma_2-\gamma_1} f_s(\Gamma) x^{\rho+\gamma_3-\gamma_1-s} g_s^2 \right)_{\rho=1-\gamma_3} \\ & = 2x^{1-\gamma_2} \sum_{s=1}^{\gamma_2-\gamma_1} \Psi_{0s}^{21} x^{-s} \frac{(-1)^{1-s} \Gamma(s) \prod_{i=2}^4 \Gamma(1 - \gamma_1 + \gamma_i)}{\prod_{i=2}^4 \Gamma(1 - \gamma_1 + \gamma_i - s)} \end{aligned} \quad (\text{B.30})$$

When $0 \leq k \leq \gamma_3 - \gamma_2 - 1$

$$\begin{aligned} & \left(\sum_{k=0}^{\gamma_3-\gamma_2-1} f_k(\Gamma) x^{\rho+k} g_k^2 \right)_{\rho=1-\gamma_3} = \left(\sum_{s=1}^{\gamma_3-\gamma_2} f_s(\Gamma) x^{\rho+\gamma_3-\gamma_2-s} g_s^2 \right)_{\rho=1-\gamma_3} \\ & = 2(-1)^{\gamma_1+\gamma_2} \Gamma(1 - \gamma_1 + \gamma_2) \frac{\prod_{i=2}^4 \Gamma(1 - \gamma_1 + \gamma_i)}{\prod_{i=3}^4 \Gamma(\gamma_i - \gamma_2)} \\ & \cdot \frac{1}{x^{\gamma_2}} {}_5F_0([1, 1, 1 + \gamma_2 - \gamma_1, 1 + \gamma_2 - \gamma_3, 1 + \gamma_2 - \gamma_4], [], \frac{1}{x}) \end{aligned} \quad (\text{B.31})$$

Then $z_3(x)$ can be expressed as

$$\begin{aligned} z_3(x) &= \sum_{k=0}^{\infty} f_k(\Gamma) x^{\rho_3+k} (c_0 \ln^2 x + 2g_k^1 \ln x + g_k^2) \\ &= 2z_2(x)_{\Psi_{**}^{1*} \rightarrow \Psi_{**}^{2*}} \ln x - z_1(x) \ln^2 x \\ &+ x^{1-\gamma_1} \sum_{s=0}^{\infty} [(\Psi_{0s}^{20})^2 + \Psi_{1s}^{20} + 2\pi^2] x^s \frac{\prod_{i=1}^4 \Gamma(1 - \gamma_1 + \gamma_i)}{\prod_{i=1}^4 \Gamma(1 - \gamma_1 + \gamma_i + s)} \\ &+ 2x^{1-\gamma_2} \sum_{s=1}^{\gamma_2-\gamma_1} (-1)^{1-s} \Gamma(s) x^{-s} \Psi_{0s}^{21} \prod_{i=2}^4 \frac{\Gamma(1 - \gamma_1 + \gamma_i)}{\Gamma(1 - \gamma_1 + \gamma_i - s)} \\ &+ 2(-1)^{\gamma_1+\gamma_2} \Gamma(1 - \gamma_1 + \gamma_2) \frac{\prod_{i=2}^4 \Gamma(1 - \gamma_1 + \gamma_i)}{\prod_{i=3}^4 \Gamma(\gamma_i - \gamma_2)} \\ &\cdot \frac{1}{x^{\gamma_2}} {}_5F_0([1, 1, 1 + \gamma_2 - \gamma_1, 1 + \gamma_2 - \gamma_3, 1 + \gamma_2 - \gamma_4], [], \frac{1}{x}) \end{aligned} \quad (\text{B.32})$$

where $\bar{z}_2(x)$ can be obtained by substituting Ψ_{**}^{2*} for Ψ_{**}^{1*} in $z_2(x)$ given by Eq. (B.24).

B.3 $z_4(x)$

Under this case $c_0 = c'_0(\rho + \gamma_3 - 1)^3$. For $k \geq \gamma_4 - \gamma_1$, the coefficient of $\ln^3 x$ of Eq. (B.10) are calculated as

$$\left(\sum_{k=\gamma_4-1}^{\infty} f_k(\Gamma)x^{\rho+k}c_0 \right)_{\rho=1-\gamma_4} = \frac{c'_0(-1)^{1+\gamma_1+\gamma_2+\gamma_3-\gamma_4}}{\prod_{i=1}^3 \Gamma(\gamma_4 - \gamma_i) \prod_{i=2}^4 \Gamma(1 - \gamma_1 + \gamma_i)} z_1(x) \quad (\text{B.33})$$

c'_0 is chosen to make the coefficient of $z_1(x)$ equal to 1:

$$c'_0 = (-1)^{1+\gamma_1+\gamma_2+\gamma_3-\gamma_4} \prod_{i=1}^3 \Gamma(\gamma_4 - \gamma_i) \prod_{i=2}^4 \Gamma(1 - \gamma_1 + \gamma_i) \quad (\text{B.34})$$

then

$$\begin{aligned} \left(\sum_{k=\gamma_4-\gamma_1}^{\infty} f_k(\Gamma)x^{\rho+k}g_k^3 \right)_{\rho=1-\gamma_4} &= \left(\sum_{s=0}^{\infty} f_s(\Gamma)x^{\rho+\gamma_4-\gamma_1+s}g_s^3 \right)_{\rho=1-\gamma_4} \\ &= x^{1-\gamma_1} \sum_{s=0}^{\infty} [(\Psi_{0s}^{30})^3 + \Psi_{2s}^{30} + 3\Psi_{0s}^{30}(\Psi_{1s}^{30} + 3\pi^2)] x^s \prod_{i=1}^4 \frac{\Gamma(1 - \gamma_1 + \gamma_i)}{\Gamma(1 - \gamma_1 + \gamma_i + s)} \end{aligned} \quad (\text{B.35})$$

$$\begin{aligned} \left(\sum_{k=\gamma_4-\gamma_1}^{\infty} f_k(\Gamma)x^{\rho+k}g_k^2 \right)_{\rho=1-\gamma_4} &= \left(\sum_{s=0}^{\infty} f_s(\Gamma)x^{\rho+\gamma_4-\gamma_1+s}g_s^2 \right)_{\rho=1-\gamma_4} \\ &= x^{1-\gamma_1} \sum_{s=0}^{\infty} [(\Psi_{0s}^{30})^2 + \Psi_{1s}^{30} + 3\pi^2] x^s \prod_{i=1}^4 \frac{\Gamma(1 - \gamma_1 + \gamma_i)}{\Gamma(1 - \gamma_1 + \gamma_i + s)} \end{aligned} \quad (\text{B.36})$$

$$\begin{aligned} \left(\sum_{k=\gamma_4-\gamma_1}^{\infty} f_k(\Gamma)x^{\rho+k}g_k^1 \right)_{\rho=1-\gamma_4} &= \left(\sum_{s=0}^{\infty} f_s(\Gamma)x^{\rho+\gamma_4-\gamma_1+s}g_s^1 \right)_{\rho=1-\gamma_4} \\ &= x^{1-\gamma_1} \sum_{s=0}^{\infty} \Psi_{0s}^{30} x^s \prod_{i=1}^4 \frac{\Gamma(1 - \gamma_1 + \gamma_i)}{\Gamma(1 - \gamma_1 + \gamma_i + s)} \end{aligned} \quad (\text{B.37})$$

When $\gamma_4 - \gamma_2 \leq k \leq \gamma_4 - \gamma_1 - 1$

$$\begin{aligned} \left(\sum_{k=\gamma_4-\gamma_2}^{\gamma_4-\gamma_1-1} f_k(\Gamma)x^{\rho+k}g_k^1 \right)_{\rho=1-\gamma_4} &= \left(\sum_{s=1}^{\gamma_2-\gamma_1} f_s(\Gamma)x^{\rho+\gamma_4-\gamma_1-s}g_s^1 \right)_{\rho=1-\gamma_4} \\ &= \prod_{i=2}^4 (\gamma_i - \gamma_1) \frac{1}{x^{\gamma_1}} {}_5F_0([1, 1, 1 + \gamma_1 - \gamma_2, 1 + \gamma_1 - \gamma_3, 1 + \gamma_1 - \gamma_4], [], \frac{1}{x}) \end{aligned} \quad (\text{B.38})$$

$$\begin{aligned} \left(\sum_{k=\gamma_4-\gamma_2}^{\gamma_4-\gamma_1-1} f_k(\Gamma)x^{\rho+k}g_k^2 \right)_{\rho=1-\gamma_4} &= \left(\sum_{s=1}^{\gamma_2-\gamma_1} f_s(\Gamma)x^{\rho+\gamma_4-\gamma_1-s}g_s^2 \right)_{\rho=1-\gamma_4} \\ &= 2x^{1-\gamma_1} \sum_{s=1}^{\gamma_2-\gamma_1} \Gamma(s)(-1)^{1-s} x^{-s} \Psi_{0s}^{31} \prod_{i=2}^4 \frac{\Gamma(1 - \gamma_1 + \gamma_i)}{\Gamma(1 - \gamma_1 + \gamma_i - s)} \end{aligned} \quad (\text{B.39})$$

$$\begin{aligned}
 & \left(\sum_{k=\gamma_4-\gamma_2}^{\gamma_4-\gamma_1-1} f_k(\Gamma)x^{\rho+k}g_k^3 \right)_{\rho=1-\gamma_4} = \left(\sum_{s=1}^{\gamma_2-\gamma_1} f_s(\Gamma)x^{\rho+\gamma_4-\gamma_1-s}g_s^3 \right)_{\rho=1-\gamma_4} \\
 & = 3x^{1-\gamma_1} \sum_{s=1}^{\gamma_2-\gamma_1} \Gamma(s)(-1)^{1-s}x^{-s}[(\Psi_{0s}^{31})^2 + \Psi_{1s}^{31} + 2\pi^2] \prod_{i=2}^4 \frac{\Gamma(1-\gamma_1+\gamma_i)}{\Gamma(1-\gamma_1+\gamma_i-s)}
 \end{aligned} \tag{B.40}$$

When $\gamma_4 - \gamma_3 \leq k \leq \gamma_4 - \gamma_2 - 1$

$$\begin{aligned}
 & \left(\sum_{k=\gamma_4-\gamma_3}^{\gamma_4-\gamma_2-1} f_k(\Gamma)x^{\rho+k}g_k^2 \right)_{\rho=1-\gamma_4} = \left(\sum_{s=1}^{\gamma_3-\gamma_2} f_s(\Gamma)x^{\rho+\gamma_4-\gamma_2-s}g_s^2 \right)_{\rho=1-\gamma_4} \\
 & = 2(-1)^{\gamma_1+\gamma_2}\Gamma(1-\gamma_1+\gamma_2) \frac{\prod_{i=2}^4 \Gamma(1-\gamma_1+\gamma_i)}{\prod_{i=3}^4 \Gamma(\gamma_i-\gamma_2)} \\
 & \quad \cdot \frac{1}{x^{\gamma_2}} {}_5F_0\left([1, 1, 1+\gamma_2-\gamma_1, 1+\gamma_2-\gamma_3, 1+\gamma_2-\gamma_4], [], \frac{1}{x}\right)
 \end{aligned} \tag{B.41}$$

$$\begin{aligned}
 & \left(\sum_{k=\gamma_4-\gamma_3}^{\gamma_4-\gamma_2-1} f_k(\Gamma)x^{\rho+k}g_k^3 \right)_{\rho=1-\gamma_4} = \left(\sum_{s=1}^{\gamma_3-\gamma_2} f_s(\Gamma)x^{\rho+\gamma_4-\gamma_2-s}g_s^3 \right)_{\rho=1-\gamma_4} \\
 & = 6(-1)^{\gamma_1+\gamma_2}x^{1-\gamma_2} \prod_{i=2}^4 \Gamma(1-\gamma_1+\gamma_i) \sum_{s=1}^{\gamma_3-\gamma_2} \frac{\Gamma(\gamma_2-\gamma_1+s)\Gamma(s)x^{-s}\Psi_{0s}^{32}}{\prod_{i=3}^4 \Gamma(1+\gamma_i-\gamma_2-s)}
 \end{aligned} \tag{B.42}$$

When $0 \leq k \leq \gamma_4 - \gamma_3 - 1$

$$\begin{aligned}
 & \left(\sum_{k=0}^{\gamma_4-\gamma_3-1} f_k(\Gamma)x^{\rho+k}g_k^3 \right)_{\rho=1-\gamma_4} = \left(\sum_{s=1}^{\gamma_4-\gamma_3} f_s(\Gamma)x^{\rho+\gamma_4-\gamma_3-s}g_s^3 \right)_{\rho=1-\gamma_4} \\
 & = 6(-1)^{\gamma_1+\gamma_2} \frac{\prod_{i=2}^4 \Gamma(1-\gamma_1+\gamma_i) \prod_{i=1}^2 \Gamma(1-\gamma_i+\gamma_3)}{\Gamma(\gamma_4-\gamma_3)} \\
 & \quad \cdot \frac{1}{x^{\gamma_3}} {}_5F_0\left([1, 1, 1+\gamma_3-\gamma_1, 1+\gamma_3-\gamma_2, 1+\gamma_3-\gamma_4], [], \frac{1}{x}\right)
 \end{aligned} \tag{B.43}$$

then

$$\begin{aligned}
z_4(x) &= \sum_{k=0}^{\infty} f_k(\Gamma) x^{\rho_4+k} (c_0 \ln^3 x + 3g_k^1 \ln^2 x + 3g_k^2 \ln x + g_k^3) \\
&= z_1(x) \ln^3 x - 3z_2(x)_{\Psi_{**}^1 \rightarrow \Psi_{**}^3} \ln^2 x + 3z_3(x)_{\Psi_{**}^2 \rightarrow \Psi_{**}^3, 2\pi^2 \rightarrow 3\pi^2} \ln x \\
&\quad + 6(-1)^{\gamma_1+\gamma_2} \frac{\prod_{i=2}^4 \Gamma(1-\gamma_1+\gamma_i) \prod_{i=1}^2 \Gamma(1-\gamma_i+\gamma_3)}{\Gamma(\gamma_4-\gamma_3)} \\
&\quad \cdot \frac{1}{x^{\gamma_3}} {}_5F_0([1, 1, 1 + \gamma_3 - \gamma_1, 1 + \gamma_3 - \gamma_2, 1 + \gamma_3 - \gamma_4], [], \frac{1}{x}) \\
&+ 6(-1)^{\gamma_1+\gamma_2} x^{1-\gamma_2} \prod_{i=2}^4 \Gamma(1-\gamma_1+\gamma_i) \sum_{s=1}^{\gamma_3-\gamma_2} \frac{\Gamma(\gamma_2-\gamma_1+s) \Gamma(s) x^{-s} \Psi_{0s}^{32}}{\prod_{i=3}^4 \Gamma(1+\gamma_i-\gamma_2-s)} \\
&+ 3x^{1-\gamma_1} \sum_{s=1}^{\gamma_2-\gamma_1} \Gamma(s) (-1)^{1-s} x^{-s} [(\Psi_{0s}^{31})^2 + \Psi_{1s}^{31} + 2\pi^2] \prod_{i=2}^4 \frac{\Gamma(1-\gamma_1+\gamma_i)}{\Gamma(1-\gamma_1+\gamma_i-s)} \\
&+ x^{1-\gamma_1} \sum_{s=0}^{\infty} x^s [(\Psi_{0s}^{30})^3 + \Psi_{2s}^{30} + 3\Psi_{0s}^{30}(\Psi_{1s}^{30} + 3\pi^2)] \prod_{i=1}^4 \frac{\Gamma(1-\gamma_1+\gamma_i)}{\Gamma(1-\gamma_1+\gamma_i+s)}
\end{aligned} \tag{B.44}$$

where $\bar{z}_2(x)$ can be obtained by substituting Ψ_{**}^{3*} for Ψ_{**}^{1*} in $z_2(x)$ given by Eq. (B.24) and $\bar{z}_3(x)$ can be obtained by substituting Ψ_{**}^{3*} and $3\pi^2$ for Ψ_{**}^{2*} and $2\pi^2$ respectively in $z_3(x)$ given by Eq. (B.32)..

B.4 Convergence conditions

For checking the convergence condition of logarithmic solutions $z_2(x)$, $z_3(x)$ and $z_4(x)$ given by Eqs. (B.24), (B.32) and (B.44) respectively, the infinite series included in $z_2(x)$, $z_3(x)$ and $z_4(x)$ expressed by Eqs. (B.18), (B.27), (B.28), (B.35), (B.36) and (B.37) will be checked. These infinite series can be expressed in the general form:

$$x^{1-\gamma_1} \sum_{s=0}^{\infty} x^s [\sum \Psi_{**s}^{**}] \prod_{i=1}^4 \frac{\Gamma(1-\gamma_1+\gamma_i)}{\Gamma(1-\gamma_1+\gamma_i+s)} \tag{B.45}$$

where $\sum \Psi_{**s}^{**}$ is the summation of polygamma functions. Let u_s denotes the s term in Eq. (B.45) and define

$$d = \lim_{s \rightarrow \infty} \frac{u_{s+1}}{u_s} = \lim_{s \rightarrow \infty} \frac{\sum \Psi_{**s+1}^{**}}{\sum \Psi_{**s}^{**}} \frac{x}{\prod_{i=1}^4 (1-\gamma_1+\gamma_i+s)} \tag{B.46}$$

Since $\lim_{s \rightarrow \infty} \frac{\sum \Psi_{*s+1}^{**}}{\sum \Psi_{*s}^{**}} = 1$, hence if x is finite, $d < 1$. Then the infinite series in Eq. (B.45) converge for all finite x (i.e. all cases except for $m \neq 2$).

To illustrate, Ψ_{0s}^{10} in relation to $\sum \Psi_{*s}^{**}$ in Eq. (B.27) will be used as an example to prove that $\lim_{s \rightarrow \infty} \sum \Psi_{*s+1}^{**} / \sum \Psi_{*s}^{**} = 1$. The proofs for other $\sum \Psi_{*s}^{**}$ terms appearing in Eqs. (B.27), (B.28), (B.35), (B.36) and (B.37) follow the same procedure. Ψ_{0s}^{10} can be expressed according to Eq. (B.11) as

$$\Psi_{0s}^{10} = \sum_{t=2}^4 \varphi_0(1 - \gamma_2 + \gamma_t) + \varphi_0(\gamma_2 - \gamma_1) - \sum_{t=1}^4 \varphi_0(1 - \gamma_1 + \gamma_t + s) \quad (\text{B.47})$$

Since

$$\varphi_n(z) = (-1)^{n+1} n! \sum_{k=0}^{\infty} \frac{1}{(z+k)^{n+1}} \quad (\text{B.48})$$

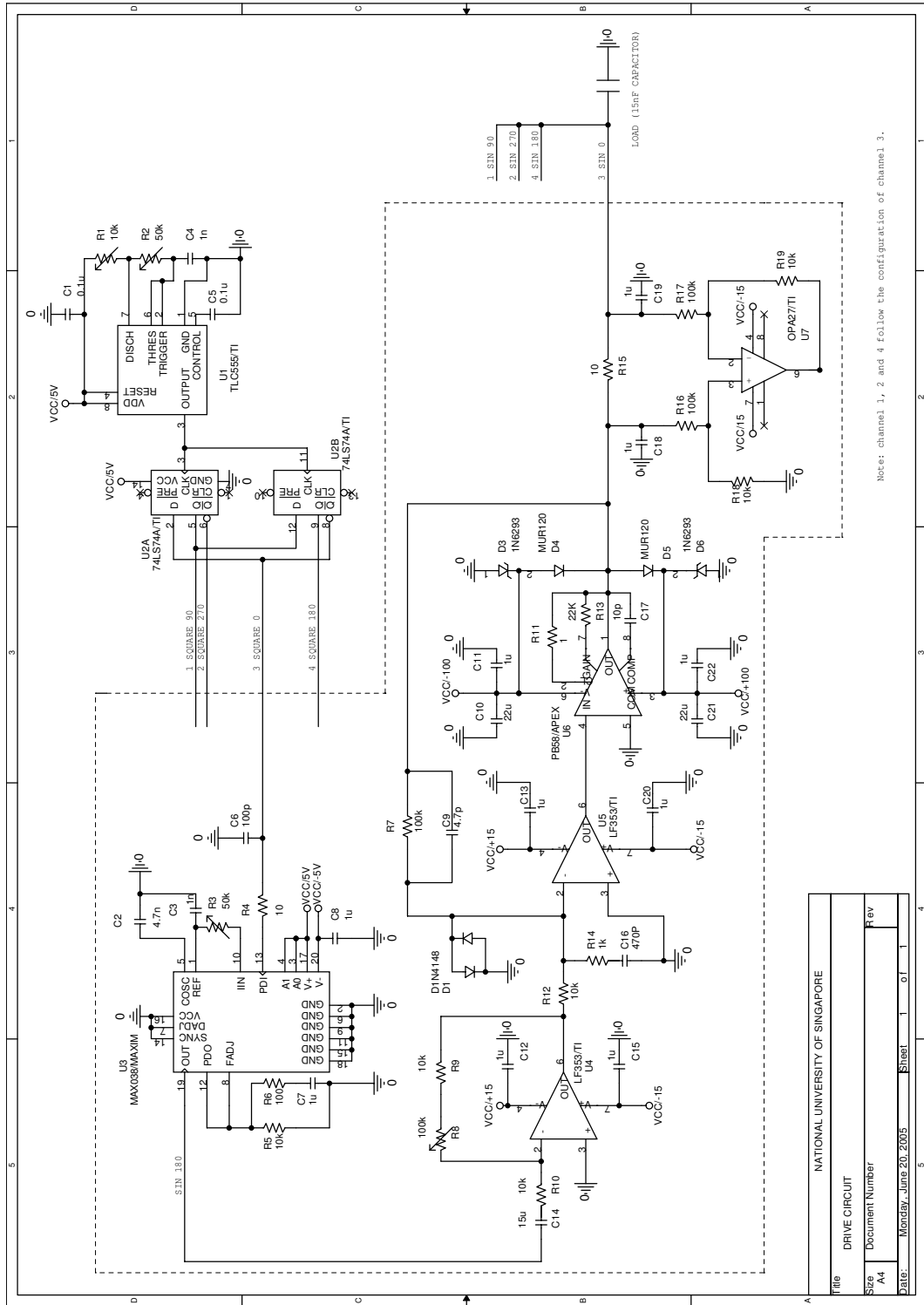
$$\Psi_{0s}^{10} = \sum_{k=0}^{\infty} \left[\sum_{t=1}^4 \frac{1}{1 - \gamma_1 + \gamma_t + s + k} - \sum_{t=2}^4 \frac{1}{1 - \gamma_2 + \gamma_t + k} - \frac{1}{\gamma_2 - \gamma_1 + k} \right] \quad (\text{B.49})$$

then

$$\lim_{s \rightarrow \infty} \frac{\Psi_{0s+1}^{10}}{\Psi_{0s}^{10}} = 1 \quad (\text{B.50})$$

Appendix C

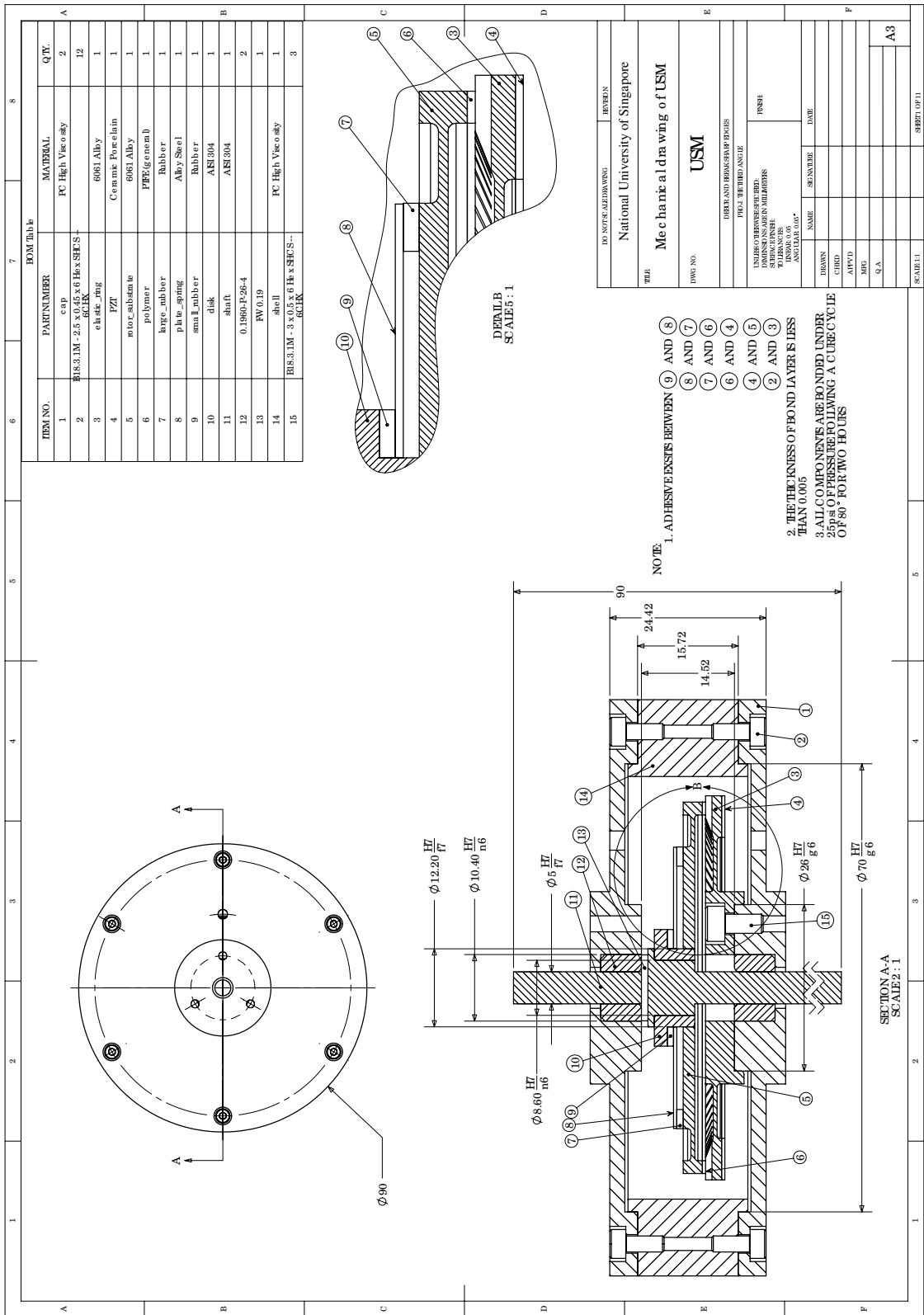
Electrical Drawing

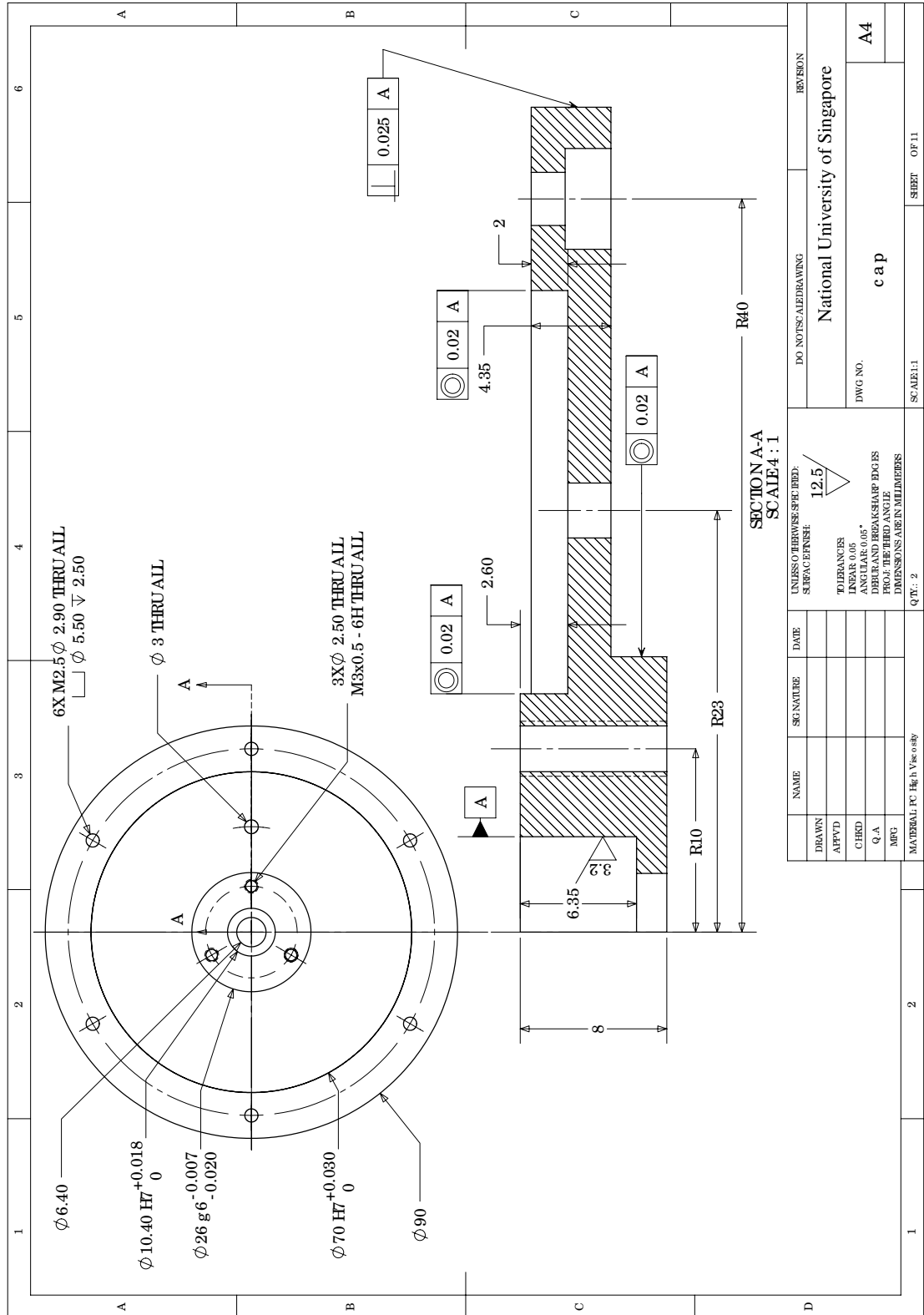


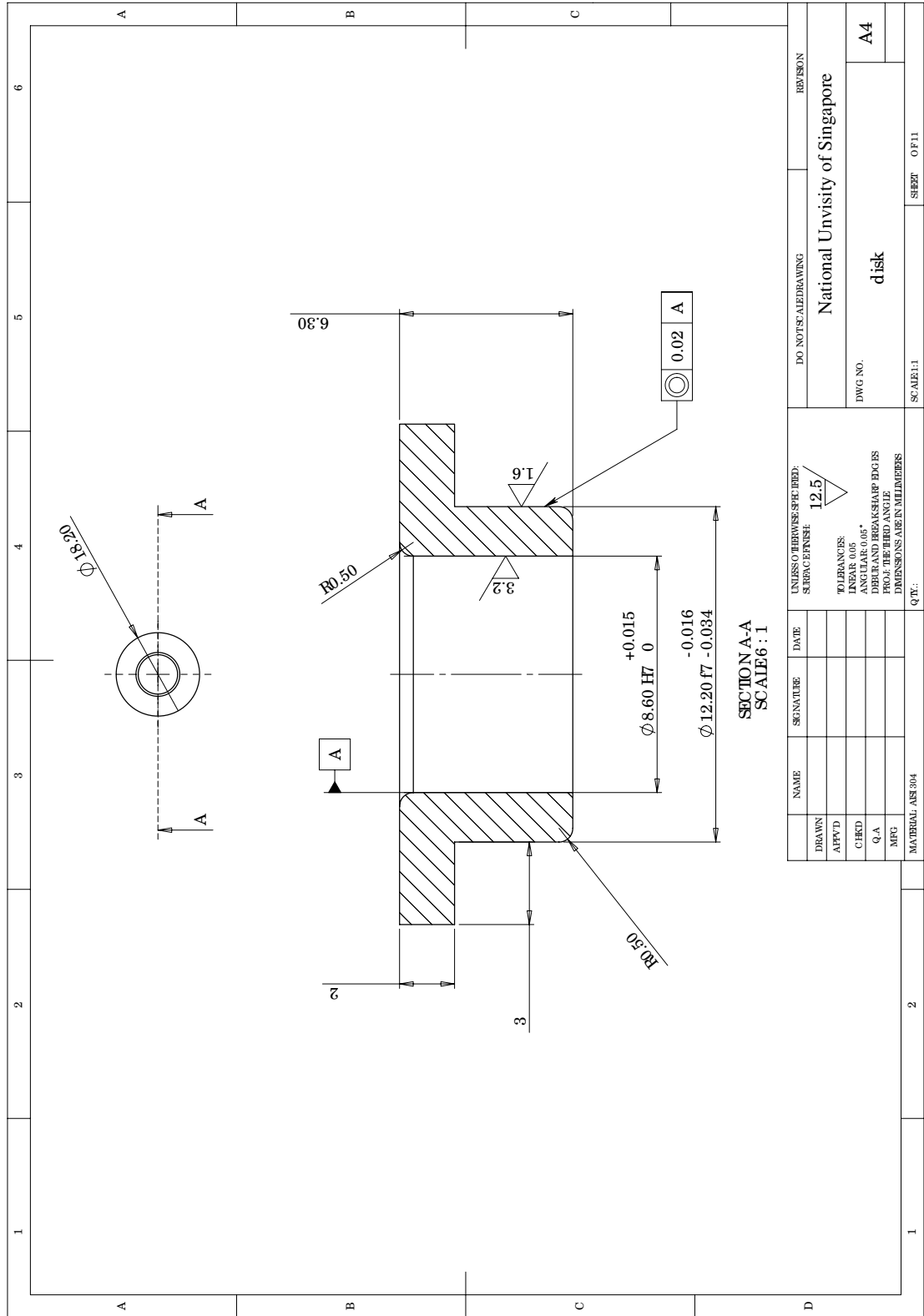
NATIONAL UNIVERSITY OF SINGAPORE	
Title	DRIVE CIRCUIT
Size	Document Number
A4	Rev
Date:	Monday, June 20, 2005 Sheet 1 of 1

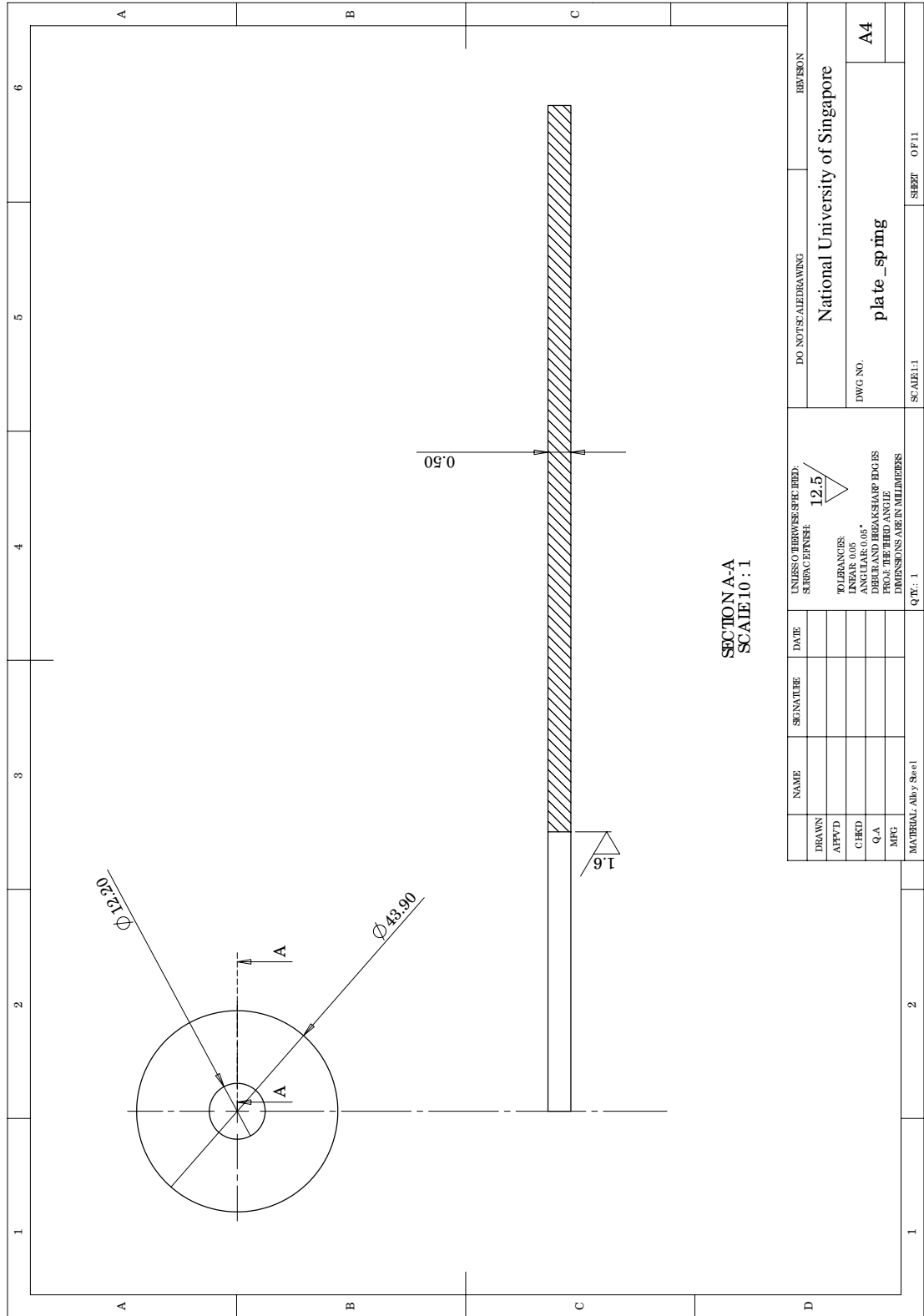
Appendix D

Mechanical Drawing

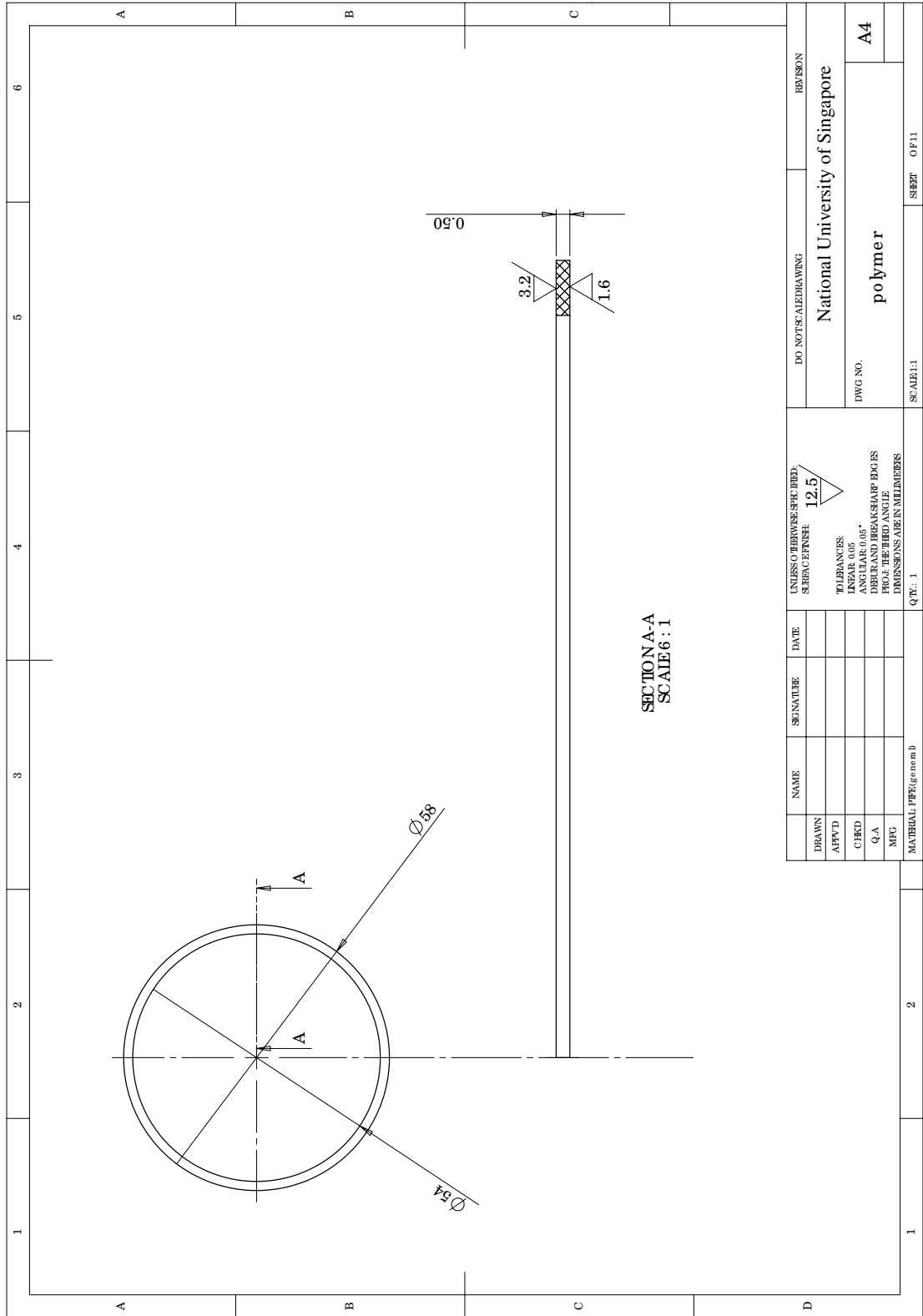


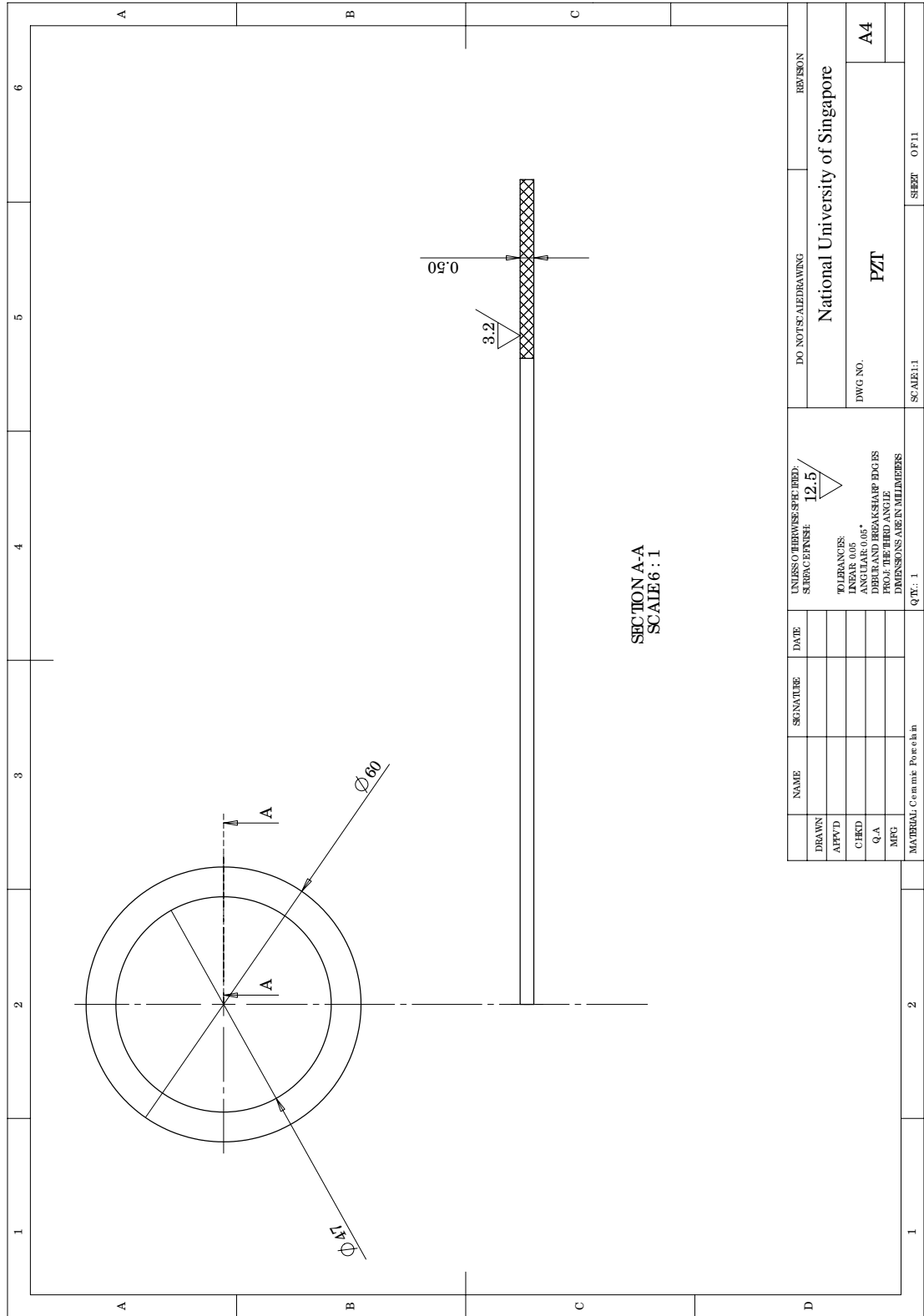




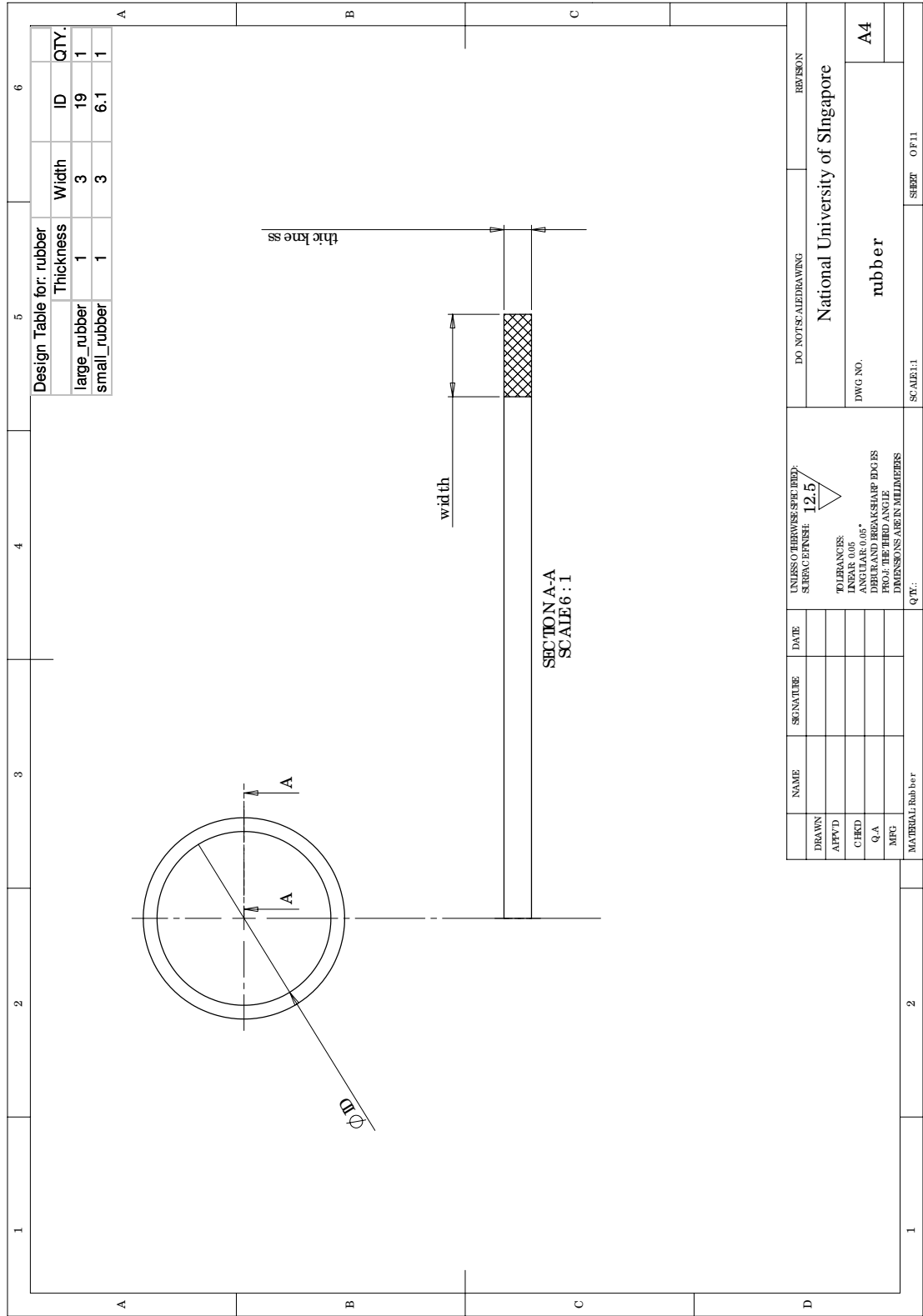


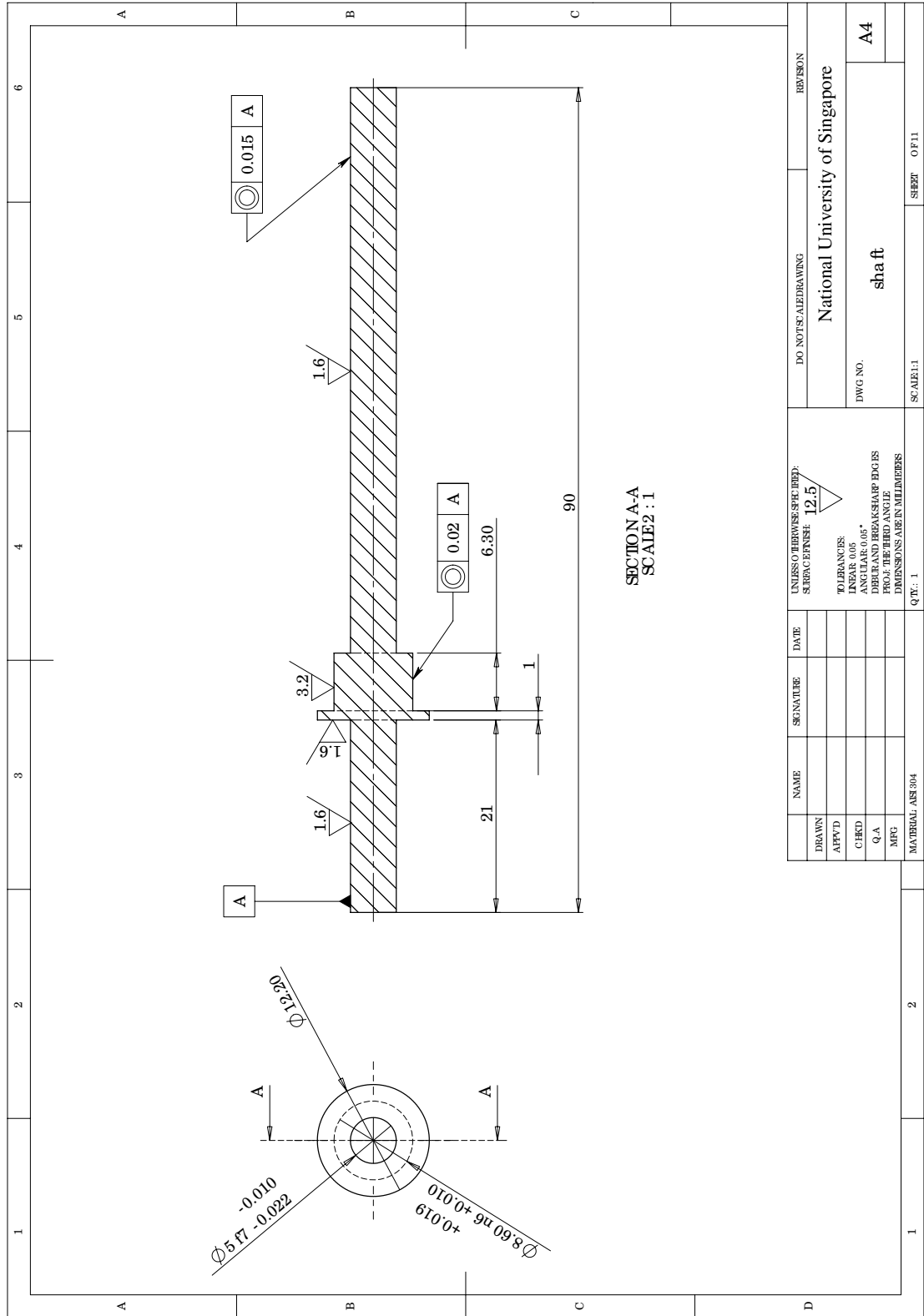
NAME	SIGNATURE	DATE	UNLESS OTHERWISE SPECIFIED, SURFACE FINISH: 12.5	DO NOT SCALE DRAWING	REVISION
DRAWN			TOLERANCES: UNLESS OTHERWISE SPECIFIED: ANGLES TO 0.01° DEBUR AND BREAK SHARP EDGES PROF. THE THIRD ANGLE DIMENSIONS ARE IN MILLIMETERS	National University of Singapore plate_spring	A4
APPROV'D					
CHKD					
Q.A					
MFG					
MATERIAL: Alloy Steel			SCALE: 1:1	SHEET: 0 F 11	

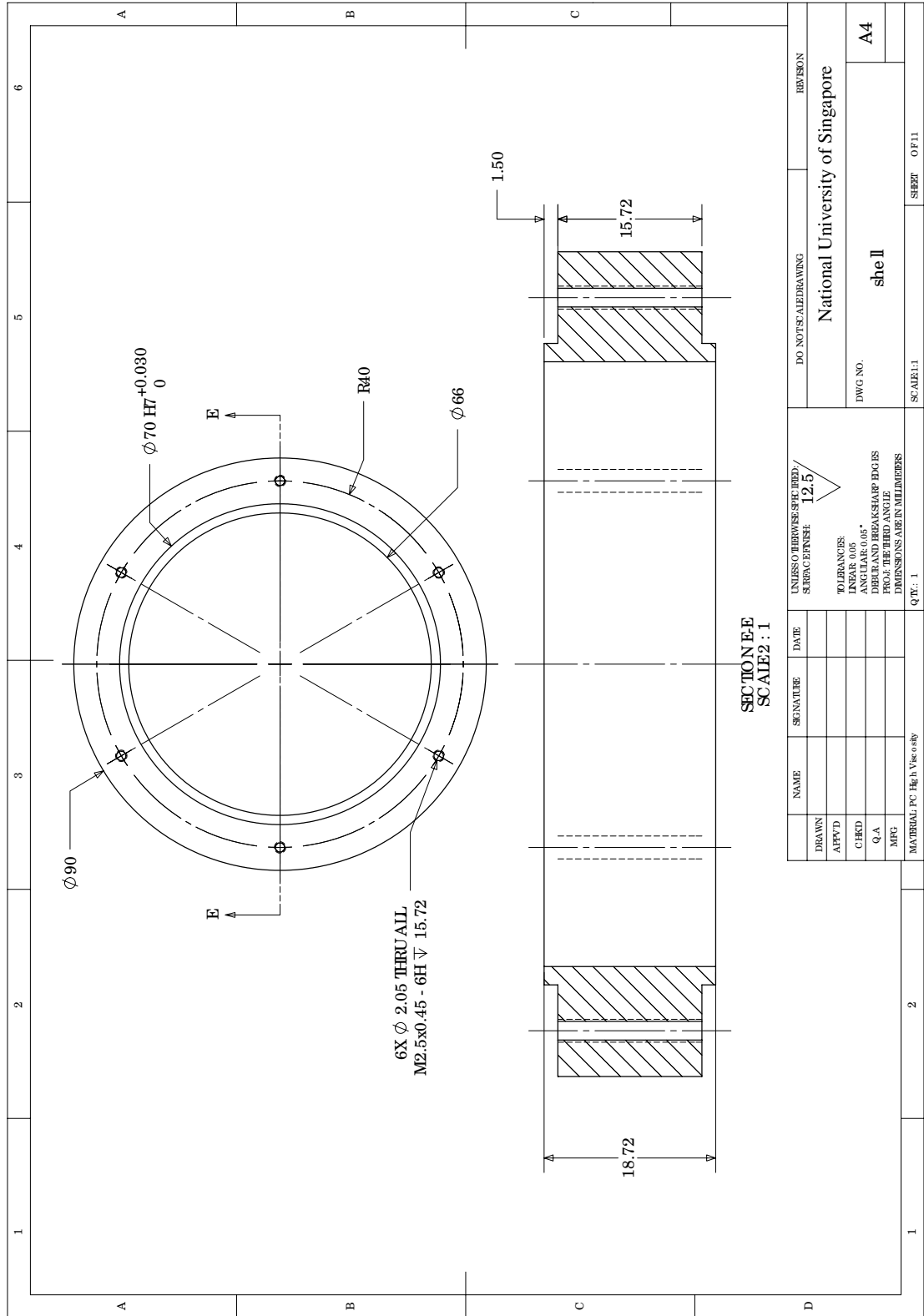




NAME		SENATE	DATE	UNLESS OTHERWISE SPECIFIED, TOLERANCES ARE:	DO NOT SCALE DRAWING	REVISION		
DRAWN				12.5	National University of Singapore			
APP'D				ANGLES TO 0.05°		DWG. NO.	A4	
CHECK				DEBUR AND BREAK SHARP EDGES		PZT		
Q.A				PROF. THE THIRD ANGLE				
MFG				DIMENSIONS ARE IN MILLIMETERS				
MATERIAL: Cement Potchahn				QTY: 1	SCALE: 1:1	SHEET: 0 F11		







Appendix E

Vita

Name: Duan WenHui
Place of Birth: Inner Mongolia, China
Date of Birth: November 10th, 1973

Education

TianJin University, China	1993-1997	B. Eng. (Engineering Mechanics)
TianJin University, China	1999-2002	M. Eng. (General Mechanics)
National University of Singapore, Singapore	2002-2006	Ph.D. (Smart Materials and Structures)

Honours and Awards

Research Scholarship (2002-2006) National University of Singapore

Publications

Wang, Q., **W.H. Duan**, and S.T. Quek
Repair of notched beam under dynamic load using piezoelectric patch
International Journal of Mechanical Sciences, 2004. 46(10): p. 1517-1533.

Duan, W.H., S.T. Quek, and Q. Wang
Free vibration analysis of piezoelectric coupled thin and thick annular plate
Journal of Sound and Vibration, 2005. 281(1-2): p. 119-139.

ScienceDirect TOP25 Hottest Articles within Journal of Sound and Vibration:
Ranking 3.

Duan, W.H., S.T. Quek, and Q. Wang
Generalized hypergeometric function solutions for transverse vibration of a class of
non-uniform annular plates
Journal of Sound and Vibration, 2005. 287(4-5): p. 785-807.

To be continued on the next page

Duan, W. H., S.T. Quek and S. P. Lim

Finite element solution for intermittent-contact problem with piezoelectric actuation in ring type ultrasonic motor (under review)

Duan, W. H., S.T. Quek and S. P. Lim

Design, fabrication and characterization of a ring type ultrasonic motor with multiple wave numbers (under review)

P. S. Tua, S.T. Quek and **W. H. Duan**

Finite Element Analysis on Repair of Cracked Beam with Piezoelectric Patch
The Seventeenth KKCNN Symposium on Civil Engineering, December 13-15, 2004, Thailand pp 211-216

W. H. Duan, S.T. Quek and S. P. Lim

Finite Element Analysis of a Ring-Type Ultrasonic Motor
The SPIE conference on Modeling, Signal Processing, and Control, March 07-10, 2005, San Diego, CA USA.

Qiu, Y., **Duan, W. H.**, Zhang D. D., Qiu, J. J.

Multiple resonance excited by electro-magnetic or water current of shaft system in large scale hydroelectric generating set
Journal of vibration engineering, 17, pp.28-30. 2004 17: 28-30.

Qiu Jiajun, **Duan W. H.**

Axial Displacement and Axial Electromagnetic Force of Rotor System in Hydro-Turbine Generator
Journal of Mechanical Strength 2003 3: 285-289

Qiu Jiajun, **Duan W. H.**

Analytical Solution to Oil Film Stiffness and Damping of Thrust Bearing
Large Electric Machine and Hydraulic Turbine 2002 2:5-8

Qiu Jiajun, **Duan W. H.**

Axial Electromagnetic Force and Axial Vibration of Hydroturbine
Conference of National Rotor Dynamics Institute,91-95, 2001, Yanji. China